DESY-THESIS-1998-036
December 1998

Diffractive Dissociation in ep Deep Inelastic Scattering

by

G. M. Briskin

ISSN 1435-8085

To be sure that your reports and preprints are promptly included in the HEP literature database
send them to (if possible by air mail):

DESY Zentralbibliothek Notkestraße 85 22607 Hamburg Germany	DESY Bibliothek Platanenallee 6 15738 Zeuthen Germany

TEL AVIV UNIVERSITY
RAYMOND AND BEVERLY SACKLER
FACULTY OF EXACT SCIENCES

Diffractive Dissociation in *ep* Deep Inelastic Scattering

Thesis submitted towards a Ph.D. Degree
at Tel Aviv University
School of Physics and Astronomy, Tel Aviv University
by
Gennady M. Briskin.

The research work for this thesis was carried out in the Experimental
High Energy Physics Group of Tel Aviv University
under the supervision of
Prof. Halina Abramowicz
and
Prof. Aharon Levy.

June 1998

Abstract

The deep inelastic diffractive cross section, $d\sigma^D_{\gamma^* p \to XN}/dM_X$, has been measured in the mass range $M_X \leq 15$ GeV for $\gamma^* p$ center of mass energies $60 < W < 200$ GeV and photon virtualities $Q^2 = 7$ to 140 GeV^2. For fixed Q^2 and M_X, the diffractive cross section is found to rise rapidly with W. Parameterizing the W dependence by the form $d\sigma^D_{\gamma^* \to XN}/dM_X \propto (W^2)^{(2\overline{\alpha_{\mathbb{P}}}-2)}$ the data yielded for the t-averaged Pomeron trajectory a value of $\overline{\alpha_{\mathbb{P}}} = 1.135 \pm 0.008(stat)^{+0.011}_{-0.030}(syst)$. This value for the Pomeron trajectory is larger than $\overline{\alpha_{\mathbb{P}}}$ extracted from soft interactions. The W dependence of the diffractive cross section measured in this analysis is found to be the same as that of the total cross section for scattering of virtual photons on protons. From the measured diffractive cross section the diffractive structure function of the proton $F_2^{D(3)}(\beta, x_{\mathbb{P}}, Q^2)$ has been determined. We find the data to be consistent with the assumption that the diffractive structure function $F_2^{D(3)}$ factorizes according to $x_{\mathbb{P}} F_2^{D(3)}(x_{\mathbb{P}}, \beta, Q^2) = (x_0/x_{\mathbb{P}})^n F_2^{\mathbb{P}}(\beta, Q^2)$. They are also consistent with QCD based models which incorporate factorization breaking. The rise of $x_{\mathbb{P}} F_2^{D(3)}$ with decreasing $x_{\mathbb{P}}$ and the weak dependence of $F_2^{\mathbb{P}}$ on Q^2 suggest a substantial contribution from partonic interactions.

To my dear friend and wife Lisa

and

my parents and grandparents

Contents

List of Figures

List of Tables

Introduction

Quantum Chromodynamics (QCD) has proven to be a very successful theory in describing the world of strong interactions. QCD explains strong interactions as being due to exchange of gauge bosons (gluons) between gluons and quarks (partons) which are part of the fundamental constituents of matter. The confrontation of QCD with experiment can only be tested in hard particle interactions occurring at short distances for which the coupling constant of strong interactions becomes small. This latter property of QCD, called asymptotic freedom, is the foundation for the Quark Parton Model (QPM) in which partons are believed to act as free point–like particles.

One of the most important aspects of strong forces is confinement of colored partons within hadrons. It is believed to be a property of QCD but has never been proven rigorously, as perturbation theory is not applicable in the region of long range forces responsible for confinement.

In this non–perturbative region some global aspects of soft interactions are successfully described by Regge theory [1]. In Regge approach, interactions between hadrons occur through exchanges of the Regge trajectories which, with one exception, correspond to real observable particles. The Regge trajectory which carries the vacuum quantum numbers is called Pomeron and has no corresponding known particle.

Despite the wealth of data [2], the nature of the Pomeron remains elusive. The concept of the Pomeron has been studied in terms of perturbative QCD by many authors [3]. The ideas about the nature of the Pomeron range from a simple diagram with two gluon exchange [4, 5] to a coherent Pomeron [6] which initiates the hard scattering as if it were a point–like particle, from a soft Pomeron to a Lipatov Pomeron, from a universal structure of the Pomeron to a non–universal one.

The most promising laboratory for investigating the Pomeron is diffractive scattering in particle interactions. The best example of a diffractive reaction is the process of elastic scattering of two particles, $hh' \to hh'$, in which no quantum numbers are exchanged. In addition to the elastic scattering, there are inelastic diffractive processes. These include the single dissociation, $hh' \to hX$, and the double dissociation, $hh' \to YX$, reactions in which the beam and/or the target particles are excited into states with the same internal quantum numbers as those of the incoming particles. Typical of known properties of diffractive processes is a weak dependence of the cross section on energy and factorization properties suggested by a fairly independent ratio of the diffractive to the total cross section [7]. Another characteristic of high energy elastic and diffractive scattering is the exponential suppression of the cross section as a function of the square of the momentum transfer, t, between the two hadrons. As this property is reminiscent of the diffraction of light by a circular aperture, the diffractive scattering in strong interactions derives its name from the optical analogy. In general a process is called diffractive if it proceeds via Pomeron exchange, an exchange which carries the quantum numbers of vacuum.

It has been suggested that the Pomeron structure could be probed with a virtual photon at HERA [8, 9, 10]. By requiring the scale governing the interaction to be large, through the large photon virtuality, the dynamics of diffraction can be investigated and compared to perturbative calculations. The experimental signature of a Pomeron exchange would consist of a large rapidity gap in the hadronic final state, located between the photon and the proton fragmentation regions. This is in contrast to the dominant mechanism of Deep Inelastic Scattering (DIS) in which the color transfer between the struck quark and the proton remnant is responsible for populating the rapidity interval between them with hadrons.

The observation of events with a large rapidity gap in the final state produced in deep inelastic electron proton interactions reported by the ZEUS Collaboration [11] and H1 Collaboration [12] has thus opened a whole new area of studies in QCD. Large rapidity gap events have been also observed at HERA in the region where the photon emitted from the electron is almost real and known to behave like a hadron [13, 14].

The discovery of large rapidity gap events at HERA has steered much interest among theoreticians and renewed their activity in the field. Since then many workshops were organized with the aim to discuss the basic theoretical ideas and predictions for diffractive phenomena within the QCD framework and to improve the understanding of HERA data.

Diffraction was extensively studied in hadron-hadron interactions approximately thirty years ago. Many properties of the diffractive scattering and in particular the observed factorization properties find a natural explanation if it is assumed that diffractive processes are indeed mediated by an exchange of the universal Pomeron trajectory. The universality of the exchanged trajectory has been proposed originally by Gribov and Pomeranchuk [15] and is usually referred to as Regge factorization.

The experimental program to study the properties of diffractive processes in the presence of a large scale has only recently started. From the theoretical point of view it becomes essential to analyze various processes in terms of which type of Pomeron could be probed. The QCD picture of the Pomeron points to its non-universal nature. There is general consensus that an understanding of the Pomeron nature can establish the missing link between the short-range and long range strong interactions.

Both HERA collider experiments, ZEUS and H1 have studied photon diffractive dissociation in the photoproduction regime [16, 17], in which the electron is scattered under a small angle and the interaction can be thought of as proceeding through a beam of quasi-real photons scattering on a proton target. The energy range covered by the HERA experiments is an order of magnitude larger than for the fixed target experiments. From these measurements it was concluded that photon diffractive dissociation in photoproduction follows a similar pattern as single diffractive dissociation in hadron-hadron interactions.

The measurements of diffractive properties in deep inelastic scattering have also been performed by ZEUS [18, 19] and H1 [20, 21]. These early results were compatible with the Regge factorization, however the values of the Pomeron intercept determined from the energy dependence of the diffractive structure function were inconclusive as to the nature of the Pomeron probed in deep inelastic scattering. This was one of the many open questions at the start of the analysis presented here. The main issue was whether the Pomeron probed in DIS is "soft", by which it is generally meant that the intercept is the same as measured in hadron-hadron or photon-hadron interactions, or whether it is "hard", which corresponds to expectations of perturbative QCD models.

Two major difficulties arise when studying diffractive scattering at HERA. The first difficulty is encountered in the selection of the diffractive sample. At HERA, the highly sophisticated detectors cover predominantly the photon fragmentation region, leaving out for precise measurements most of the proton fragmentation region. The second difficulty arises because not all events which have topological properties typical for diffractive dissociation are due to Pomeron exchange. This thesis reports on the continuing efforts to understand, control and improve reconstruction and selection of diffractive events in inclusive *ep* deep inelastic scattering collisions at HERA with the ZEUS detector.

This thesis presents details and improvements of the analysis for the measurement of the diffractive cross section in deep inelastic neutral current scattering. The extraction of the diffractive contribution $\gamma^* p \to XN$ is performed with the 1994 data using the method developed in [19]. A factor of about five increase in luminosity combined with improved detector performance, off-line reconstruction procedure and better Monte Carlo event generators permits to extend the Q^2 region from previous 10 - 56 GeV^2 to 7 - 140 GeV^2 and to reduce statistical and systematical errors.

In the first chapter a brief overview of deep inelastic scattering is presented, followed by a review of those aspects of diffractive scattering addressed with the data discussed here. The second chapter gives a description of the HERA collider and the ZEUS detector with emphasis on those components which are relevant for this analysis. A description of the Monte Carlo generators used to simulate deep inelastic and diffractive processes, as well as, the ZEUS software chain is presented in the third chapter. Chapter four describes the preselection of the data sample using the ZEUS three-level trigger system. The event reconstruction which is the main new feature of the analysis is described in chapter five. Particular emphasis is put on a new reconstruction algorithm for the hadronic final state, identification of the scattered electron, and energy corrections which improve the quality of the data. Chapter six gives details about selection cuts applied in order to obtain the final neutral current deep inelastic event sample. The extraction of the diffractive sample is described in chapter seven. The measurement of the diffractive cross section and the corresponding structure function F_2^D are presented in chapter eight together with a detailed discussion of systematic uncertainties. A discussion of the results and comparison with representative theoretical approaches then follows.

Chapter 1

Theoretical Review

In this chapter we will first describe the kinematics of Deep Inelastic (DIS) and Diffractive Scattering. The theoretical framework of DIS will be presented, followed by a discussion of the physics at small x. The overview of models proposed to describe diffractive scattering will be presented next. In the end the methods used at HERA for kinematic variable reconstruction are reviewed.

1.1 Kinematic Variables

The basic quantities used for the description of inclusive deep inelastic scattering in the process

$$e(k) + P(p) \to e'(k') + anything$$

are,

$$\begin{aligned} Q^2 &= -q^2 = -(k-k')^2 \quad , \\ x &= \frac{Q^2}{2p\cdot q} \quad , \\ y &= \frac{p\cdot q}{p\cdot k} \quad , \\ W^2 &= \frac{Q^2(1-x)}{x} + m_p^2 \approx \frac{Q^2}{x} \text{ for } x \ll 1 \quad , \end{aligned} \tag{1.1}$$

where k and k' are the four-momenta of the initial and final state leptons, p is the initial state proton four-momentum and m_p is the proton mass. The four-momentum transfer squared Q^2 gives the transverse resolving power of the probe with wavelength $\lambda = 1/Q$ (we set $\hbar = c = 1$). x is the Bjorken scaling variable. In the parton model x can be interpreted as the proton momentum fraction carried by the struck quark. The variable y is the fractional energy transferred from the lepton to the proton in the proton rest frame. W is the $\gamma^* p$ center of mass (c.m.) energy. For the range of Q^2 and W considered here, $W^2 \approx y \cdot s$, where $s = 4E_e E_p$ stands for the square of the *ep* c.m. energy, $\sqrt{s} = 300$ GeV.

The large c.m. energy gives access to the kinematic regions both at very small x and at large Q^2. The Q^2 range at HERA varies from about zero up to 10^5 GeV^2. The very low Q^2 region corresponds to interactions with an almost real photon, while the large Q^2 region allows to probe the proton down to distances of 10^{-16} cm.

For the description of the diffractive interactions

$$e(k) + P(p) \rightarrow e'(k') + X + P'(p'),$$

we use X to denote the final state corresponding to the photon dissociation and by P' the final state proton. If the proton dissociates we denote its state by N to indicate that it is still separated from the state X.

To describe the diffractive final states new variables are introduced. We define the square of the momentum transfer at the proton vertex,

$$t = (p - p')^2 \, ,$$

where p' is the 4-momentum of the outgoing proton. In the case of proton dissociation p' should be replaced the 4-momentum of the outgoing system N.

The fraction of the proton momentum carried by the Pomeron is defined as

$$x_{I\!P} = \frac{(p - p') \cdot q}{p \cdot q} = \frac{M_X^2 + Q^2 - t}{W^2 + Q^2 - m_p^2} \, ,$$

where M_X is the invariant mass of the hadronic system produced as the outcome of photon dissociation. For large Q^2 and W^2 the influence of t and m_p on $x_{I\!P}$ is negligible. It should be noted that the subscript IP may not always be adequate, although it still make sense to talk about the fraction of proton momentum vested in the interaction. This is particularly true for models in which large rapidity gap formation does not involve the notion of the Pomeron.

In analogy to x we define β as the Bjorken variable related to the Pomeron,

$$\beta = \frac{Q^2}{2(p - p') \cdot q} = \frac{x}{x_{I\!P}} = \frac{Q^2}{Q^2 + M_X^2 - t} \, .$$

Here again t is only included for completeness. Note that $x = \beta \cdot x_{I\!P}$.

At HERA the kinematic variables can be determined either from the electron alone, or from the measured hadronic system alone, or from a combination of both. The hadronic measurement relies mostly upon the calorimeter. At medium to large y the precision of the hadronic method can be improved by momentum measurements in the trackers.

The Electron Method

The kinematic variables are calculated from the energy E'_e and the angle θ_e of the scattered electron (measured with respect to the proton direction) as follows:

$$y_{el} = 1 - \frac{E'_e}{2E_e}(1 - \cos\theta'_e) \tag{1.2}$$

$$Q^2_{el} = 2E_e E'_e(1 + \cos\theta'_e) \tag{1.3}$$

$$x_{el} = \frac{E_e}{E_p} \frac{E'_e(1 + \cos\theta'_e)}{2E_e - E'_e(1 - \cos\theta'_e)}, \tag{1.4}$$

where E_e and E_p are the electron and proton beam energies, respectively. Although the simplest method, requiring only a single particle measurement, the electron method has intrinsic difficulties. A small deviation in the measured electron energy, at low y, result in large uncertainties in the determination of x.

The Hadron Method

The method proposed by Jacquet and Blondel [72] permits evaluation of the kinematic variables entirely with the hadronic system. The Jacquet-Blondel (JB) equations are:

$$y_{jb} = \frac{E_h - p_{zh}}{2E_e} \tag{1.5}$$

$$Q^2_{jb} = \frac{p^2_{xh} + p^2_{yh}}{1 - y_{jb}} \tag{1.6}$$

$$x_{jb} = \frac{Q^2_{jb}}{s y_{jb}}. \tag{1.7}$$

Here E_h, p_{xh}, p_{yh} and p_{zh} denote the 4-vector components of the hadronic system, which are calculated as the 4-momentum sum over all final state hadrons h. The sums run over all final state hadrons. Jacquet and Blondel have shown that the contribution from hadrons lost in the beam pipe is insignificant.

The Double Angle Method

In the Double Angle (DA) method [73], the event variables x, y and Q^2 are reconstructed from the angle of the final state electron, θ'_e, and the angle, γ_h, that characterizes the final state hadronic system. The angle γ_h is determined from the hadronic energy flow measured in the detector using the equation

$$cos\gamma_h = \frac{p^2_{xh} + p^2_{yh} - (E_h - p_{zh})^2}{p^2_{xh} + p^2_{yh} + (E_h - p_{zh})^2}. \tag{1.8}$$

In the naïve quark-parton model γ_h is the scattering angle of the struck quark. The DA kinematic variables can be calculated from γ_h regardless of its interpretation:

$$\begin{aligned} Q^2_{DA} &= 4E_e^2 \cdot \frac{\sin\gamma_h(1 + \cos\theta'_e)}{\sin\theta'_e + \sin\gamma_h - \sin(\theta'_e + \gamma_h)} \\ x_{DA} &= \frac{E_e}{E_p} \cdot \frac{\sin\theta'_e + \sin\gamma_h + \sin(\theta'_e + \gamma_h)}{\sin\theta'_e + \sin\gamma_h - \sin(\theta'_e + \gamma_h)} \\ y_{DA} &= \frac{\sin\theta'_e(1 - \cos\gamma_h)}{\sin\theta'_e + \sin\gamma_h - \sin(\theta'_e + \gamma_h)}. \end{aligned} \tag{1.9}$$

We study in this thesis events of the type

$$ep \rightarrow e' + X + rest,$$

where X denotes the hadronic system observed in the detector and *rest* the particle system escaping detection through the beam holes. The mass M_X of the system X is determined from the energy flow objects according to:

$$(M_X^{meas})^2 = (\sum_j E)^2 - (\sum_j p_x)^2 - (\sum_j p_y)^2 - (\sum_j p_z)^2 \, . \tag{1.10}$$

1.2 Deep Inelastic Scattering

The differential cross section $ep \to e'X$ can be expressed in terms of two[1] independent structure functions F_1 and F_2, which describe the coupling of the virtual photon to the proton and are functions of two variables, x and Q^2,

$$\begin{aligned}\frac{d^2\sigma}{dxdQ^2} &= \frac{4\pi\alpha_{em}^2}{xQ^4}\left[(1-y)F_2 + y^2 x F_1\right] \\ &= \frac{4\pi\alpha_{em}^2}{xQ^4}\left[1-y+\frac{y^2}{2}\frac{1}{1+R}\right]\cdot F_2 \\ &= \frac{4\pi\alpha_{em}^2}{xQ^4}\left[(1-y+\frac{y^2}{2})\cdot F_2 - \frac{y^2}{2}\cdot F_L\right], \end{aligned} \tag{1.11}$$

where α_{em} is the electromagnetic coupling constant. Here we have expressed the cross section also in terms of the longitudinal structure function F_L and the ratio R, defined as

$$F_L \equiv F_2 - 2xF_1 \qquad R \equiv \frac{F_L}{F_2 - F_L} = \frac{\sigma_L}{\sigma_T}. \tag{1.12}$$

R can be interpreted as the ratio of the cross sections σ_L and σ_T for the absorption of longitudinally and transversely polarized virtual photons on protons, with $\sigma_{tot}^{\gamma^* p} = \sigma_L + \sigma_T$. The relation between the structure functions and the virtual photon, γ^*, cross sections can be expressed[2] as,

$$\begin{aligned} F_2(x,Q^2) &= \frac{Q^2(1-x)}{4\pi^2\alpha_{em}}\frac{Q^2}{Q^2+4m_p^2x^2}\cdot\sigma_{tot}^{\gamma^* p} \approx \frac{Q^2}{4\pi^2\alpha_{em}}(\sigma_L(x,Q^2)+\sigma_T(x,Q^2)) \\ F_L(x,Q^2) &= \frac{Q^2(1-x)}{4\pi^2\alpha_{em}}\cdot\sigma_L(x,Q^2) \approx \frac{Q^2}{4\pi^2\alpha_{em}}\cdot\sigma_L(x,Q^2), \end{aligned} \tag{1.13}$$

where in the approximate expressions small x was assumed.

The experimental program is to measure the structure functions and to understand them in terms of a more microscopic picture of the proton. This is first addressed by reviewing briefly the quark-parton model, and then turning to our current theory describing the strong interactions, Quantum Chromodynamics (QCD).

1.3 The Quark Parton Model

According to Feynman's parton model [23], the proton is assumed to be composed of free point-like constituents, called partons. In this model the deep-inelastic ep cross section can be viewed as the incoherent sum of a two body elastic electron parton scattering cross sections weighted by the parton distribution functions $f_i(x)$.

A consequence of the assumption that the proton consists of point-like constituents and that electron-parton scattering is point-like, is that these parton density functions should only depend on x, that is, be independent of Q^2, or "scale invariant", as x contains no scale of mass or length. This is the Bjorken scaling hypothesis [24].

[1] In this thesis we only consider small to moderate Q^2, so that the exchange of the Z boson has been neglected (a 1% correction for $Q^2 \approx 1000$ GeV^2), and the structure function F_3 thus been omitted.

[2] We use the Hand convention[22] for the definition of the virtual photon flux.

By writing the cross section for electron-proton scattering in terms of parton density functions, a relation between these functions and the structure functions F_1 and F_2 may be identified,

$$F_2(x) = x\sum_i e_i^2 f_i(x), \tag{1.14}$$

$$\text{and} \quad F_1(x) = \frac{1}{2x}F_2(x), \tag{1.15}$$

where e_i is the charge of the parton and $f_i(x)\mathrm{d}x$ is the probability to find a parton i in the momentum interval between x and $x+\mathrm{d}x$. Equation 1.15, known as the Callan-Gross relationship [25], is a direct consequence of the spin-$\frac{1}{2}$ nature of partons; for spin zero partons the ratio $\frac{2xF_1}{F_2}$ would be zero.

Scaling was indeed observed at the Stanford Linear Accelerator in 1969 [26], and measurement of the ratio $\frac{2xF_1}{F_2}$ at the same experiment confirmed the spin-$\frac{1}{2}$ nature of the point like partons. Since the SLAC results confirmed the Callan-Gross relation Feynman's partons were identified with Gell-Mann's quarks and the model was called the Quark-Parton Model (QPM). The fractional charge of the partons was later confirmed using neutrino-nucleon scattering and the postulated number of 3 valence quarks (uud/ddu) in the proton/neutron was experimentally confirmed using the Gross-Llewellyn-Smith sum rule [27].

If the proton consisted only of charged quarks, their momentum would be expected to add up to the proton momentum,

$$\sum_i \int_0^1 \mathrm{d}x x f_i(x) = 1. \tag{1.16}$$

However, experimentally a value of ~ 0.5 was found [28], implying that about half of the proton's momentum is carried by neutral partons. Direct evidence for the existence of these partons, called gluons, was provided in 1979 at DESY via the observation of three-jet events in e^+e^- annihilation [29]. Furthermore, later experiments demonstrated that scale invariance is approximately true for $x \sim 0.15$, and that the significant variations of the structure function F_2 with Q^2 are observed at higher and lower values of x, see figure 1.1. These deviations from the expectations of the quark parton model are explained by the theory of Quantum Chromodynamics.

1.4 The Quantum Chromodynamics Theory

The Quantum Chromodynamics (QCD) field theory was developed in the 1970's to describe the physics of strong interactions. QCD is a non-abelian gauge theory based on the SU(3) color symmetry group. In QCD, the quarks are not free, but interact through the gauge bosons called gluons. As a consequence of the non-abelian structure of QCD the gluons also carry color charge themselves and therefore couple to each other. This self coupling of the gauge bosons in QCD is the main difference to QED. In QED, the effective charge coupling increases at very small distances, whereas in QCD the color coupling decreases at short distances.

The scale dependence of the strong coupling constant α_S in leading order perturbation theory is given by

$$\alpha_S(Q^2) = \frac{12\pi}{(33-2n_f)\ln(\frac{Q^2}{\Lambda^2})} \tag{1.17}$$

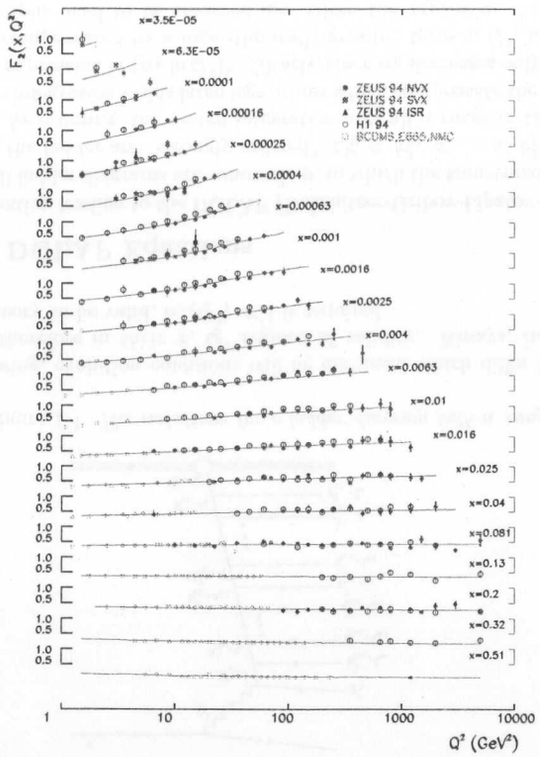

Figure 1.1: *The structure function $F_2(x, Q^2)$ as a function of Q^2, for fixed x values.*

where n_f is the number of quark flavors. The QCD scale parameter Λ represents the energy scale at which the strong coupling constant becomes large and perturbation theory breaks down. At a large energy scale α_S vanishes logarithmically. This behavior of α_S is known as *asymptotic freedom*. Within the framework of QCD the quark parton model appears only in the asymptotic limit as $Q^2 \to \infty$.

QCD, as discussed so far, modifies the conclusions drawn from the QPM. The modifications to the QPM result from dynamics among the partons via the gluon as the mediating gauge boson and permit a simple interpretation of the violation of the scaling hypothesis. In QCD the quarks may radiate (and absorb) gluons, which in turn may split into quark-antiquark pairs or gluon pairs. More and more of these fluctuations can be resolved with shorter wavelength of the photonic probe, $\lambda = 1/Q$. With Q^2 increasing we have a depletion of quarks at large x and corresponding accumulation at lower x. This means that at high values of x, $F_2(x, Q^2)$ should decrease with increasing Q^2, whilst at low value of x it should increase. In fact, at small x it is the gluon content with distribution function $g(x, Q^2)$ that governs the proton and gives rise to the DIS cross section via the creation of $q\bar{q}$ pairs.

In the QCD improved parton model the main result obtained is that the parton densities, and thus the F_2 structure function acquire a Q^2 dependence. The mechanism of these scaling violations is formalized in the evolution equations, and is described in more details in the next section.

1.5 Factorization Theorem of QCD

Due to the presence of non-perturbative effects the calculation of the inclusive cross section σ_{ep} from first principles in QCD is not possible. However, the QCD factorization theorem [30] addresses this situation and allows to write the cross section for ep scattering symbolically as

$$\sigma_{ep} = \sum_i \left[f_{i/p}(\mu_F^2) \otimes \sigma_{ei}(\mu_F^2) \right], \tag{1.18}$$

see figure 1.2a. The σ_{ei} cross section denotes the short distance interaction. It is independent of long distance effects and is computable in perturbative QCD (pQCD). The parton distribution functions $f_{i/p}$ are not calculable in pQCD. They have to be determined experimentally. They depend on the type of hadron, but not on the particular scattering process considered. Thus they are a universal description of the partons and their soft, long range interactions.

The separation of the scattering process into short-distance dependences calculable in pQCD and into long-distance dependences which need to be taken from outside the theory is called *factorization*. The separation is set by a factorization scale μ_F. The cross section σ_{ep} is a measurable quantity and therefore cannot dependent on the choice of the factorization scale. Often one chooses $\mu_F^2 = Q^2$, because then σ_{ei} reduces to the Born graph (here $ei \to ei$ by γ exchange, figure 1.2b). In the parton picture $f_{i/p}(Q^2)$ is then interpreted as the parton density in the proton as seen by a photon with virtuality (resolving power) Q^2.

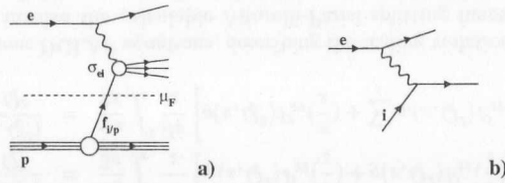

Figure 1.2: *a) Deep Inelastic Scattering. The ep cross section is factorized into electron-parton cross section σ_{ei} and parton density $f_{i/p}$ with the factorization scale μ_F. b) The lowest order diagram contribution to σ_{ei} in a).*

1.6 Evolution Equations

Since $\sigma_{ei}(\mu_F^2)$ can be calculated perturbatively for any scale, one can also calculate the change of the parton distribution functions with a change of scale. These are the *evolution equations*. For the derivation of the evolution equations, one has to perform the perturbative calculation of σ_{ei}, taking into account all contributing graphs, see figure 1.3. In order to carry out the calculation in practice certain approximations need to be applied. Such

approximations are then valid in regions of x and Q^2 where the selected contributions are dominant.

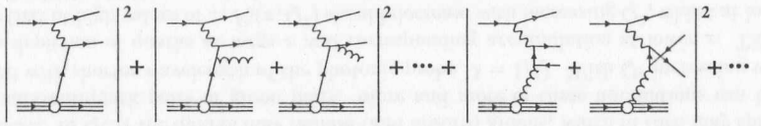

Figure 1.3: *Diagrams contributing to the DIS cross section* σ_{ep}.

In a "physical" gauge, in which only the physical transverse gluon polarization states need to be taken into account, the individual contributions of the perturbation series can be represented by so-called ladder diagrams, see figure 1.4. In the figure the transverse momenta of the emitted quanta are denoted with p_{Ti}. Similarly, the transverse momenta carried by the quanta that constitute the side rails of the ladder are k_{Ti}. The longitudinal components are given in fractions of the proton energy E_i/E_p and are labeled with ξ_i for the emitted quanta and with x_i for the internal quanta. Energy-momentum conservation requires $x_i = x_{i+1} + \xi_i$, and therefore $x_i > x_{i+1}$.

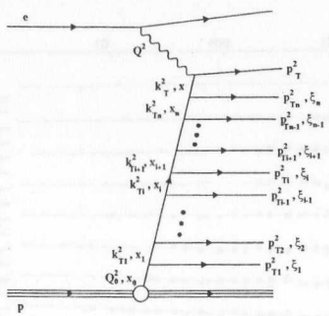

Figure 1.4: *The notations for a ladder diagram with n rungs.*

In the following, evolution equations will be discussed which differ in their approximations, and therefore in their x, Q^2 regions of validity. Always, in order to allow perturbation theory to be valid, $\alpha_S(Q^2) \ll 1$ is required.

1.6.1 The DGLAP Equations

In the approximation leading to the DGLAP (Dokshitzer-Gribov-Lipatov-Altarelli-Parisi) equations [31] all ladder diagrams are summed up, in which the transverse momenta along the side rails of the ladder are "strongly ordered", $Q_0^2 \ll k_{T1}^2 \ll \ldots \ll k_{Tn}^2 \ll Q^2$.

With strong k_T ordering, the nested integration over all n rungs in the ladder can be carried out. The integration yields large logarithms which compensate the smallness of α_S. The result is an expression $\propto (\alpha_S \ln Q^2)^n$. Clearly, since α_S decreases only logarithmically with Q^2 and is compensated by a logarithmically growing term in Q^2, in a perturbative expansion all graphs need to be summed up. Often the expression "re-summation" is used, because the perturbation series is re-arranged such that the largest terms come

first. This is called a leading log approximation (here in $\ln Q^2$), since each power n in α_S is accompanied by the same power of $\ln Q^2$.

This approximation is valid when Q^2 is large, but x is not too small in order not to produce also large logarithms,

$$\alpha_S(Q^2) \ln \frac{1}{x} \ll \alpha_S(Q^2) \ln Q^2 \lesssim 1. \tag{1.19}$$

In this approximation, the evolution equations for the quark density q_i for flavor i and gluon density g are

$$\begin{aligned} \frac{dq_i(x,Q^2)}{d\ln Q^2} &= \frac{\alpha_S}{2\pi} \int_x^1 \frac{dz}{z} \left[q_i(z,Q^2) P_{qq}(\frac{x}{z}) + g(z,Q^2) P_{qg}(\frac{x}{z}) \right] \\ \frac{dg(x,Q^2)}{d\ln Q^2} &= \frac{\alpha_S}{2\pi} \int_x^1 \frac{dz}{z} \left[g(z,Q^2) P_{gg}(\frac{x}{z}) + \sum_i q_i(z,Q^2) P_{gq}(\frac{x}{z}) \right]. \end{aligned} \tag{1.20}$$

These are the famous DGLAP equations, describing the scaling violations of the structure functions. They involve the calculable Altarelli-Parisi splitting functions $P_{ij}(\zeta)$. The splitting functions $P_{ij}(\zeta)$ represent the probability per unit of $\ln Q^2$ for parton branching $q \to qg$, $g \to gg$ and $g \to q\bar{q}$, where the daughter parton i carries a fraction $1-\zeta$ of the mother's j momentum.

The solutions of the DGLAP equations give the parton distributions for any value of Q^2 and $x > x_0$, once they are known at a particular value Q_0^2 for $x > x_0$. The latter at present cannot be calculated but have to be determined experimentally.

A special case for which the DGLAP equations can also be solved analytically [32] occurs when in addition to the above conditions also strong ordering in x is required, $x_0 \gg x_1 \gg \ldots \gg x_n \gg x$. The large logarithmic terms arising from the integration are then of the form $\propto (\alpha_S(Q^2) \ln Q^2 \ln \frac{1}{x})^n$, which need to be resummed. This is the double leading log approximation (DLL). It is expected to hold when the DLL terms dominate over the others,

$$\left.\begin{array}{l} \alpha_S(Q^2) \ln Q^2 \\ \alpha_S(Q^2) \ln \frac{1}{x} \end{array}\right\} \ll \alpha_S(Q^2) \ln Q^2 \ln \frac{1}{x} \lesssim 1 \tag{1.21}$$

This is the case for large Q^2 and small x. At small x the parton content of the proton is expected to be dominated by gluons, because $P_{ij}(\zeta)$ is largest when gluons are being produced. When quarks are neglected, and $P_{gg} = \frac{6}{\zeta}$ is approximated, the DGLAP equations can be solved to yield the DLL solution for the gluon density [33]

$$xg(x,Q^2) \approx xg(x,Q_0^2) \exp \sqrt{\frac{144}{25} \ln \left[\frac{\ln(Q^2/\Lambda^2)}{\ln(Q_0^2/\Lambda^2)} \right] \ln \frac{1}{x}}, \tag{1.22}$$

provided the starting gluon density is not too singular at small x. At small x a fast rise of the gluon density with decreasing x is thus predicted. That is, xg increases faster than $(\ln \frac{1}{x})^\lambda$, but slower than $(\frac{1}{x})^{\lambda'}$ for any powers $\lambda, \lambda' > 0$. Apart from these shape restrictions the actual rate of the growth is not predicted, it depends on the "evolution length" from Q_0^2 to Q^2. Numerically this expression yields at Q^2 of about 20 GeV^2 and low x, $x \sim 10^{-4} - 10^{-3}$, power law behavior in x, $xg(x,Q^2) \sim x^{-\lambda}$, with a value of $\lambda \sim 0.35$.

1.6.2 The BFKL Equation

When x is small, but Q^2 not large enough to reach the DLL regime, the DGLAP approximations cease to be valid. For the limit $1/x$ large and Q^2 finite and fixed the BFKL (Balitsky-Fadin-Kuraev-Lipatov) [34] equation has been derived. It takes into account diagrams in which the x_i are strongly ordered, $x_0 \gg x_1 \gg \ldots \gg x_n \gg x$. No ordering on k_{Ti} is imposed. Large logarithms $\propto (\alpha_S \ln \frac{1}{x})^n$ are thus generated that need to be resummed, leading to the leading log approximation in $\ln \frac{1}{x}$. The region of validity is

$$\alpha_S(Q^2) \ln Q^2 \ll \alpha_S(Q^2) \ln \frac{1}{x} \lesssim 1. \tag{1.23}$$

The BFKL equation is expressed in terms of the "unintegrated" gluon density $f(x, k_T^2)$, which is related to the usual gluon density by

$$xg(x, Q^2) = \int_0^{Q^2} \frac{dk_T^2}{k_T^2} f(x, k_T^2). \tag{1.24}$$

The BFKL equation is an evolution equation in x. It does not discuss the Q^2 evolution. It is formulated only for gluon distribution which dominates at small x

$$\frac{\partial f(x, k_T^2)}{\partial \ln(1/x)} = \int dk_T'^2 \, K(k_T^2, k_T'^2) \cdot f(x, k_T^2), \tag{1.25}$$

where K is the BFKL kernel. $f(x, k_T^2)$ can be calculated for any (small) x, once it is known at some x_0 for all k_T^2.

Characteristic of the BFKL equation is "k_T diffusion", in contrast to k_T ordering for DGLAP. k_T diffusion poses a difficulty for the application of the BFKL equation, because k_T may diffuse into the infrared region ($k_T < Q_0^2$) where perturbation theory cannot be applied. Therefore, a lower cut-off for the k_T integration is usually introduced and the dependence of the result on that cut-off is studied.

In the large k_T regime and for a fixed α_S the equation can be solved analytically. The result is

$$xg(x, Q^2) \propto f(Q^2) \cdot x^{-\lambda} \quad \text{with} \quad \lambda = \frac{12\alpha_S}{\pi} \ln 2 \sim 0.5.$$

However, the running of α_S and higher order corrections decrease the value of λ [35].

The BFKL power law behavior leads to a violation of unitarity in the limit $x \to 0$. The rise of the gluon density at small values of x and therefore in $\sigma_{tot}^{\gamma^* p}$ is limited by the Froissart bound [36]:

$$\sigma_{tot}^{\gamma^* p} \leq \frac{\pi}{m_\pi^2} (\ln \frac{s}{s_0})^2 \tag{1.26}$$

where m_π is the mass of the pion and s_0 is an unknown scale factor. It is therefore expected that the rise of $\sigma_{tot}^{\gamma^* p}$ with decreasing x must be dampened by some mechanism.

At small values of x, the density of gluons becomes very large and gluons may annihilate, or recombine to gluons. The recombination of gluons at high densities will eventually limit their increase. In order to take the recombination of gluons $gg \to g$ into account Gribov, Levin and Ryskin added a quadratic correction to the evolution of the gluon distribution, yielding the so-called GLR equation [37]:

$$\frac{d^2 xg(x, Q^2)}{d \ln Q^2 d \ln \frac{1}{x}} = \frac{3\alpha_S}{\pi} xg(x, Q^2) - \frac{81\alpha_S^2(Q^2)}{16 R^2 Q^2} [xg(x, Q^2)]^2. \tag{1.27}$$

Recombination effects become important at $xg(x, Q^2) \simeq 6Q^2$ GeV^2 which is well outside the scope of HERA and could be only reached at much smaller values of x [38].

1.6.3 The CCFM Equation

The CCFM (Catani-Ciafaloni-Fiorani-Marchesini) equation [39] developed in recent years unifies the BFKL and DGLAP approaches and takes into account coherence effects by angular ordering. It gives the BFKL solution at low x and the DGLAP solution at high x. The CCFM approach, for the BFKL case, leads to a reduction of the exponent λ and the reduction of the k_T diffusion [40].

1.6.4 The Domain of Evolution Equations

In figure 1.5 the regions of validity of the different evolution equations are sketched. They are not predicted precisely by the theory, but have to be explored experimentally.

With DGLAP evolution a parton density $f(x, Q_0^2)$ known for $x \in [x_0, 1]$ can be evolved to any value of Q^2 for $x \in [x_0, 1]$. The behavior for $x < x_0$ cannot be predicted with DGLAP. Similarly, with BFKL evolution a parton density $f(x_0, k_T^2)$ known for $0 < k_T^2 < \infty$ can be evolved to any value of x. The new feature, orthogonal to the DGLAP evolution, is that the low x behavior is predicted by the theory. In principle DGLAP and BFKL evolution together could be used for a Münchhausen trick (bootstrapping), to predict the structure of the proton for all x as long as $Q^2 > Q_0^2$, above the cut-off to avoid the non-perturbative region.

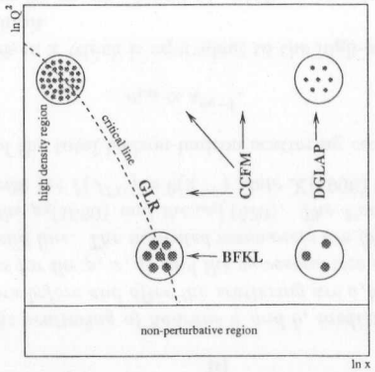

Figure 1.5: *Range of validity for various evolution equations. Increasing Q^2 leads to a better spatial resolution (DGLAP). Smaller values in x yield an increase in the parton density (BFKL). The region of high parton density is the region where saturation effects are expected to diminish the rise of F_2 with decreasing x.*

1.7 The Interest in Small x

The previous section have detailed some successes and shortcomings of QCD. The shortcomings – inability to make predictions involving non-perturbative effects – has led to a revival of Regge theory. The foundation of the Regge theory rests on general properties

of the S-matrix, unitarity and analyticity. The domain of Regge theory includes predictions for the energy dependence of hadron-hadron scattering cross sections and predictions about leading particles in the hadron-hadron collisions.

The interest in the region of large values in W (equivalent to the small x region) accessible at HERA is connected with the cross section for hadron-hadron scattering in the high energy limit within the Regge approach. This motivates why Regge theory is still of significant interest in particular for the transition region.

Before we can make the point, we need to make an excursion to Regge theory. For introduction into this field, see for example [41] as a review related to HERA physics.

Regge theory

In order to understand how Regge theory is applied, consider the elastic scattering of hadrons a and b, $ab \to ab$, as depicted in figure 1.6a. Their 4-momenta are denoted with a, b for the initial and a', b' for the final state. The cross section can be expressed as a function of the Mandelstam variables $s = (a+b)^2$ and $t = (b-b')^2$. It is the squared sum over the scattering amplitudes due to the quanta X (conventionally mesons) that can be exchanged,

$$\frac{\mathrm{d}\sigma^{\mathrm{el.}}}{\mathrm{d}t} = \frac{1}{16\pi s^2}\left|\sum_X \mathcal{M}_X^{\mathrm{el.}}(s,t)\right|^2. \tag{1.28}$$

In Regge theory, where the mesons are connected via a so-called Regge trajectory (explained below), the sum yields

$$\sum_X \mathcal{M}_X^{\mathrm{el.}}(s,t) = \mathcal{M}_{I\!R}(s,t) \propto \beta(t)\xi(\alpha(t))s^{\alpha(t)}. \tag{1.29}$$

$\beta(t)$ is the residue function which parameterizes the couplings at the hadron vertices and $\xi(\alpha(t))$ is the complex phase factor. The Regge trajectory $\alpha(t)$ gives the relationship between the mass m and the spin J of the exchanged mesons, $J = \alpha(m^2)$, see figure 1.6b.

Empirically, Regge trajectories can be parameterized as straight lines with

$$\alpha(t) = \alpha_0 + \alpha' t. \tag{1.30}$$

α_0 is called the intercept and α' the slope of the trajectory. As an example, a Regge trajectory for mesons is shown in figure 1.6b. Due to the confinement problem, meson trajectories (hadron masses) cannot yet be calculated from first principles in QCD.

The total cross section

Starting from the elastic cross section (in principle one has to sum over all Regge trajectories whose resonances can be exchanged in the reaction)

$$\frac{\mathrm{d}\sigma^{\mathrm{el.}}}{\mathrm{d}t} \propto (\beta(t))^2 \cdot s^{2\alpha(t)-2}, \tag{1.31}$$

we can use the optical theorem, relating the total cross section to the forward scattering amplitude

$$\sigma_{\mathrm{tot}} = \frac{1}{s}\mathrm{Im}\mathcal{M}_{\mathrm{el}}(s, t=0), \tag{1.32}$$

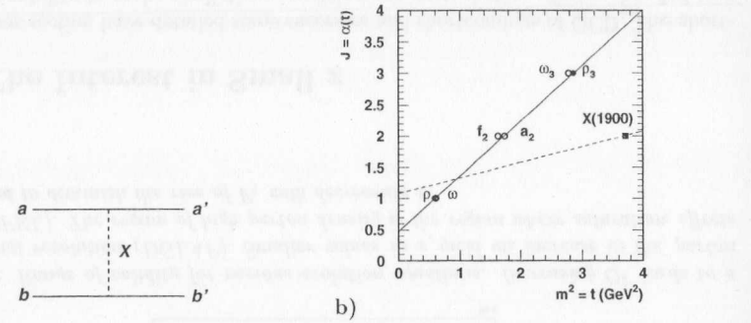

Figure 1.6: *a) The elastic scattering of hadrons a and b, mediated by the exchange of a quantum X. The 4-vectors before and after the scattering are a, b and a', b'. b) Regge trajectories. The trajectories for the ρ, ω, f_2 and the a_2 resonances almost coincide; they are represented here with a solid line. The indicated resonances are the $\rho(770)$, the $\omega(782)$, the $f_2(1270)$, the $a_2(1320)$, the $\rho_3(1690)$ and the $\omega_3(1670)$. The Pomeron trajectory (dashed line) is shown together with the $I(J^{PC}) = 0(2^{++})$ state $X(1900)$ observed by WA91 [42].*

to predict the behavior of the total hadron-hadron scattering cross section

$$\sigma_{\mathrm{tot}} \propto s^{\alpha_0 - 1}. \tag{1.33}$$

The region of small values in x which is equivalent to the high-energy limit ($s \gg Q^2$), is defined to be the Regge limit.

The total cross sections for pp, $p\bar{p}$, γp and $\gamma\gamma$ reactions are plotted as a function of the c.m. energy $\sqrt{s}$ in figure 1.7. Their behavior is surprisingly similar (and also for other hadron-hadron scattering cross sections like πp, Kp etc. that are not shown in figure 1.7 [43]). They fall at small c.m. energy $\sqrt{s} \lesssim 10$ GeV, and rise towards large energy. All these cross section can be parameterized with the universal ansatz [44]

$$\sigma_{\mathrm{tot}} = As^{\alpha_{I\!R}(0)-1} + Bs^{\alpha_{I\!P}(0)-1}. \tag{1.34}$$

A and B are process dependent parameters which are a priori unknown and need to be fitted to the data. The value of $\alpha_{I\!R}(0)$ was fixed to the average value of the Reggeon intercept ~ 0.45 and the value of $\alpha_{I\!P}(0) \sim 1.08$ was obtained from a global fit to all existing total hadron–hadron cross section data.

The Pomeron

The fall off at small energies is readily interpreted as due to meson exchange, whose Regge trajectories have an intercept $\alpha_{I\!R}(0) < 1$ (compare figure 1.6b; here only trajectories that dominate high energy scattering are shown; other meson trajectories have smaller intercepts and therefore do not contribute much to high energy scattering). Correspondingly, the rise at high energy is attributed to an exchange described by a Regge trajectory with intercept $\alpha_{I\!P}(0) > 1$. There exists however no established set of particles with such a Regge trajectory. Nevertheless, the Regge ansatz gives a successful parameterization of the scattering process. Therefore a hypothetical object, the Pomeron ($I\!P$) is postulated, which has the quantum numbers of the vacuum (electrically and colour neutral,

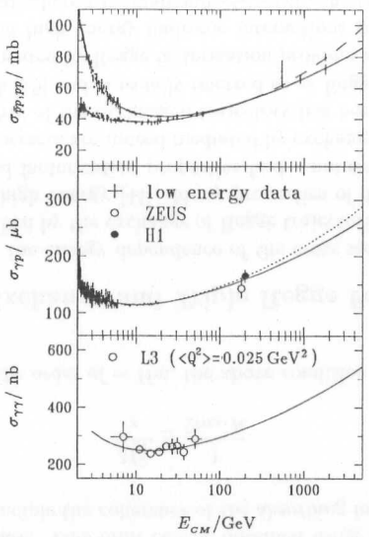

Figure 1.7: *The total cross section for pp (or $p\bar{p}$), γp and $\gamma\gamma$ interactions as a function of the total CM energy $\sqrt{s} = E_{\rm CM}$ [45]. ZEUS and H1 measure $\sigma_{\gamma p}$ in ep scattering with $Q^2 \approx 0$ (photoproduction). The curves represent the DL parameterizations with $\alpha_{I\!P}$ =1.0808 (solid), =1.112 (dashed) and =1.088 (dotted).*

isospin 0 and C parity +1), and whose exchange is described by the Pomeron trajectory $\alpha_{I\!P}(t) \approx 1.08 + 0.25 \cdot t$, see fig 1.6b. The object is suspected to be of gluonic nature, perhaps a glue ball. A possible glue ball candidate with $J^{PC} = 2^{++}$ in fact would fall on the Pomeron trajectory, see figure 1.6b. Because $\alpha_{I\!P}(0) > 1$, physical states with $J = 0, 1$ belonging to the Pomeron trajectory cannot exist.

The small x behavior of $\sigma^{\gamma^* p}$

In the high energy limit $W^2 \to \infty$, Q^2-fixed, and thus $x \to 0$ one is approaching the regime of Regge phenomenology. In this regime, the so-called Regge limit, *all* hadronic total cross sections are expected to be mediated by Pomeron exchange and to exhibit *the same* energy behavior. This expectation is born out from the data.

Scattering of virtual photons and protons at small x corresponds to the Regge limit of this subprocess ($W^2 \gg Q^2$). It is natural to ask if the total cross section behavior $\sigma_{\rm tot} \propto s^{0.08}$ found for hadron-hadron and photon-hadron scattering continues to hold for virtual photon-hadron scattering, i.e. we expect $\sigma^{\gamma^* p}$ to rise as $\sigma^{\gamma^* p} \propto (1/x)^{0.08}$ with decreasing x.

However, as was shown earlier, the pQCD prediction for the $\sigma_{tot}^{\gamma^* p}$ (or F_2) at small x will be determined by the dominant gluon content of the proton, because the quarks to which the photon couples are pair created by the gluons. The BFKL prediction for small x was

$$F_2 \propto xg(x) \propto \left(\frac{1}{x}\right)^{\lambda} \Rightarrow \sigma_{\rm tot}^{\gamma^* p} \propto s^{\lambda}. \qquad (1.35)$$

The (LO) BFKL expectation for the small x behavior of F_2 is $F_2 \propto (1/x)^{0.5}$. This power growth is faster than the growth expected from eq. 1.22, the DLL approximation.

This situation is very interesting. The experience from total cross sections at high energies would suggest that $\sigma_{tot}^{\gamma^* p}$ (or F_2) should rise $\propto (1/x)^{0.08}$ at small x, a behavior long known and parameterized with the Pomeron, but whose origin is not understood from QCD. On the other hand pQCD does make a prediction for small x, which is different from the past experience: F_2 should rise much faster, $\propto (1/x)^{0.5}$, in the BFKL approach. The DLL expectation is in between. The slow rise is often said to be due to the "soft" Pomeron or the "non-perturbative" Pomeron, or the "Donnachie-Landshoff" Pomeron. The fast rise would be attributed to the "hard", or "perturbative", or "Lipatov", or "BFKL" Pomeron, if one still wants to use the Regge language (see figure 1.8).

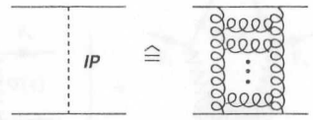

Figure 1.8: *The exchange of a (BFKL) Pomeron in the Regge language is equivalent to a sum over graphs with gluon ladders between the interacting particles in perturbative QCD.*

This is one of the reasons why *ep* scattering at HERA at small x is so interesting, that is as x decreases, for fixed large Q^2 there should be a transition between the hard short distance physics associated with moderate values of x and the physics of the "Pomeron" which is widely believed to dominate at very small x. Under which conditions will we see which behavior? How about the transition region? Do HERA data extend into a kinematic regime where the steep rise predicted by BFKL can be seen? And if a steep rise is to be seen, is it really to be attributed to BFKL dynamics? It is a theoretical and experimental challenge to establish whether events where Pomeron is being exchanged in DIS in the HERA range are governed by hard or soft processes or whether they are actually a mixture of both and to shed light on the long standing problems on the origin of the Pomeron. Some of the answers will be given by the HERA data presented in this thesis.

Ultimately the hope is that the QCD predictions for color coherent phenomena - a result of nontrivial interplay of hard and soft QCD physics specific for high energy processes - will provide an important link between the well understood physics of hard processes and the physics of soft processes which at present is mostly phenomenological.

1.8 Diffraction in Soft Interactions

The notion of diffraction in high energy physics is not easy to define. The dictionary defines it as "a modification which light undergoes in passing by the edges of opaque bodies and in which the rays appear to be deflected and to produce fringes of parallel light and dark bands; also: a similar modification of other waves (as quantum mechanical matter waves)".

We will start with a short overview of what is meant by diffractive scattering in soft hadron-hadron interactions after which we will make the connection to Regge theory and to the Pomeron which is the dominant trajectory exchanged in diffractive process.

This sets up the language which is used in studying diffractive phenomena. At the end properties of diffractive reactions in the photoproduction regime at HERA are reviewed.

1.8.1 Diffractive Scattering and Pomeron

The best example of a diffractive reaction is the process of elastic scattering $hh' \to hh'$ in which no quantum numbers are exchanged. In addition to the elastic scattering, there are inelastic diffractive processes. These include the single dissociation, $hh' \to Xh'$, and the double dissociation, $hh' \to XY$, reactions in which the beam and/or the target particles are excited into states with the same internal quantum numbers as those of the incoming particles. Some examples of inelastic diffractive processes are: $\pi^- p \to \pi^- N^*$ (SD) and $\pi^- p \to a_1^- N^*$ (DD).

Typical of known properties of diffractive processes is a weak dependence of the cross section on energy and factorization properties suggested by fairly independent ratio of the diffractive to the total cross section [7]. Another characteristic of high energy elastic and diffractive scattering is the exponential suppression of the cross section as a function of the square of the momentum transfer, t, between the two hadrons. As this property is reminiscent of the diffraction of light by a circular aperture, the diffractive scattering in strong interactions derives its name from the optical analogy. In general a process is called diffractive if it proceeds via Pomeron exchange, an exchange which carries the quantum numbers of vacuum.

In addition to all the above mentioned characteristic behaviors a single dissociation diffractive reaction of the type $hh' \to Xh'$ has a cross section which falls with the mass of X like, $1/M_X^2$. In such diffractive reactions the 'absorbing' hadron should preserve its identity. This constraint leads to the so called coherence condition and limits the invariant mass of the diffracted state. This limit can be obtained using a geometrical argument. From the uncertainty principle the coherence of the absorbing hadron of radius R will be preserved if

$$\frac{M_X^2}{s} \leq \frac{1}{2m_{h'}R}. \tag{1.36}$$

Since the radius R is of the order of $\sim$ 1fm, the above condition implies that $\frac{M_X^2}{s} \lesssim 0.1$.

1.8.2 Pomeron Exchange and Triple Regge Formalism

As mentioned previously the energy dependence of the cross sections for hadron-hadron interactions is well described by the exchange of Regge trajectories of which the Pomeron trajectory dominates at high energy [44]. Many properties of diffractive scattering and in particular the observed factorization properties find a natural explanation if it is assumed that diffractive processes are indeed mediated by exchange of a universal Pomeron trajectory. The universality of the exchanged trajectory has been proposed originally by Gribov and Pomeranchuk [15] and is usually referred to as Regge factorization.

Regge theory supplemented by Regge factorization provides a framework on the basis of which many features of high energy hadronic interactions can be described. In the Regge limit defined as that where t is small and $\frac{s}{M_X^2} \to \infty$, the total, elastic and inelastic diffraction cross sections formulae for the interaction of hadrons h and h' can be written

in the following form:

$$\sigma_T^{hh'} = \sum_k \beta_{hk}(0)\beta_{h'k}(0)s^{\alpha_k(0)-1} \tag{1.37}$$

$$\frac{d\sigma_{el}^{hh'}}{dt} = \sum_k \frac{\beta_{hk}^2(t)\beta_{h'k}^2(t)}{16\pi} s^{2\alpha_k(t)-2} \tag{1.38}$$

$$\frac{d^2\sigma^{hh'}}{dtdM_X^2} = \sum_{k,l} \frac{\beta_{hk}(0)\beta_{h'l}^2(t)g_{kll}(t)}{16\pi s}\left(\frac{s}{M_X^2}\right)^{2\alpha_l(t)}\left(M_X^2\right)^{\alpha_k(0)} \tag{1.39}$$

where the functions β and g are vertex functions and α is the Regge trajectory. The last formula (1.39) is based on Mueller's generalization of the optical theorem [46], which relates the total cross section of two-body scattering with the imaginary part of the forward elastic amplitude for the three body scattering. The term g_{kll} is called the triple-Regge coupling.

The above expressions can be illustrated with the following diagrams:

$\sigma_T^{hh'} =$ 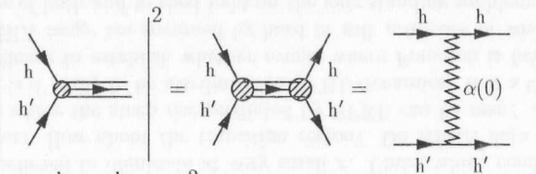 (1.40)

$\frac{d\sigma_{el}^{hh'}}{dt} =$ 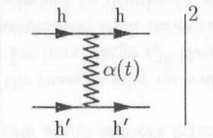 (1.41)

$\frac{d^2\sigma^{hh'}}{dtdM_X^2} =$ 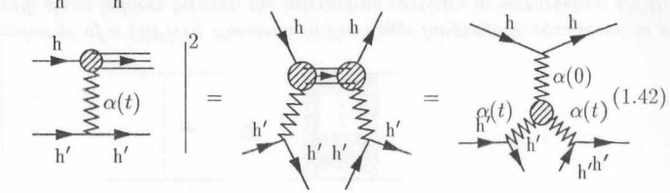 (1.42)

The above formulae have been written in a way that allows for Reggeon contributions other than the Pomeron. In order to describe the properties of diffractive scattering let us assume that at high energy only the Pomeron exchange contributes. The Pomeron trajectory was determined by Donnachie and Landshoff [44] and is given by

$$\alpha_{I\!P}(t) = 1 + \epsilon + \alpha' t\,, \tag{1.43}$$

where $\epsilon = 0.085$ and $\alpha' = 0.25$ GeV^{-2}.

The above formulae can be written in the region of Pomeron dominance as follows:

- The total cross section can be expressed as,

$$\sigma_T^{hh'} = \beta_{hI\!P}(0)\beta_{h'I\!P}(0)s^{\epsilon}. \tag{1.44}$$

- The elastic differential cross section is

$$\frac{d\sigma_{el}^{hh'}}{dt} = \frac{\beta_{h\mathbb{P}}^2(t)\beta_{h'\mathbb{P}}^2(t)}{16\pi} s^{2\epsilon} s^{2\alpha' t}. \tag{1.45}$$

Since the t distribution in the elastic scattering to a good approximation is exponential, let us assume that $\beta_{h\mathbb{P}}(t) = \beta_{h\mathbb{P}}(0)\cdot\exp(b_h t)$ where the effective slope parameter b_h is proportional to the interaction radius square. Thus, for the differential cross section of elastic scattering we get the sharp diffractive peak,

$$\frac{d\sigma_{el}^{hh'}}{dt} \approx \frac{\sigma_T^2}{16\pi} e^{b_{el}t}, \tag{1.46}$$

where the slope of the exponential behavior increases with energy like,

$$b_{el} = 2b_h + 2\alpha' \ln s.$$

We have assumed that the scale in the logarithmic expression is $s_0 = 1\text{GeV}^2$. The phenomena of the increase of the slope with energy is called shrinkage.

- The inelastic single diffraction differential cross section, assuming that at small t we can make the same approximation as in the elastic case, can be written as

$$\frac{d^2\sigma^{hh'}}{dtdM_X^2} = \frac{\beta_{h\mathbb{P}}^2(0)\beta_{h'\mathbb{P}}(0) g_{\mathbb{P}\mathbb{P}\mathbb{P}}(t)}{16\pi} \frac{1}{M_X^2} \left(\frac{s}{M_X^2}\right)^{2\epsilon} \left(M_X^2\right)^{\epsilon} e^{b_{\text{SD}}t}, \tag{1.47}$$

where here too the slope increases with energy like,

$$b_{\text{SD}} = 2b_h + 2\alpha' \ln \frac{s}{M_X^2}. \tag{1.48}$$

It is usually assumed that the t dependence of the triple-Pomeron coupling, $g_{\mathbb{P}\mathbb{P}\mathbb{P}}$, is mild compared to the t dependence of the elastic form-factors of hadrons. If we take $\epsilon = 0$, we recuperate all the properties assigned to diffraction, i.e. an exponential slope in the t distribution, shrinking with s, and $1/M_X^2$ dependence on the dissociated mass. This last behavior can be seen for the differential cross section of the inelastic diffractive reaction $pp \to Xp$ shown in figure 1.9 for different s values. As s increases and we approach the Regge domain a clear $1/M_X^2$ behavior of the cross section can be seen.

The factorization properties allow to rewrite the triple-Regge formula. The diffractive differential cross section can be expressed as a product of two terms, a flux $f_{\mathbb{P}/h'}$ which parameterizes the emission of $\mathbb{P}$ from h' and a total cross section for $h\mathbb{P}$ scattering. Symbolically the cross section can be written as,

$$\frac{d^2\sigma^{hh'}}{dtdM_X^2} = f_{\mathbb{P}/h'}(x_{\mathbb{P}}, t)\cdot\sigma_{h\mathbb{P}}(M_X^2), \tag{1.49}$$

where $x_{\mathbb{P}} = M_X^2/s$. The separation into these terms is arbitrary as far as constant factors are concerned as $\mathbb{P}$ is not a real particle. Various parameterizations for $f_{\mathbb{P}/h'}(x_{\mathbb{P}}, t)$ exist, based upon fits to hadron-hadron data and are described in more detail in chapter 3. The

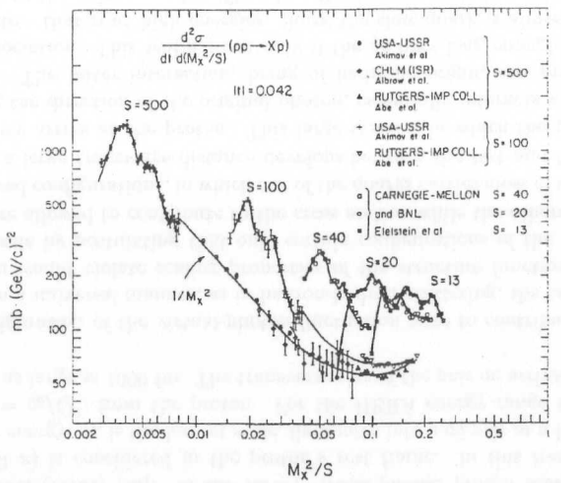

Figure 1.9: *The differential cross section for the inelastic diffractive reaction $pp \to Xp$ as function of the scaled diffractive mass M_X^2/s.*

different parameterizations differ by less than factor 2 in overall normalization, and all resemble the basic behavior $f_{\mathbb{P}/h'}(x_{\mathbb{P}}, t) \propto {x_{\mathbb{P}}}^{1-2\alpha_{\mathbb{P}}(t)}$.

All hadronic reactions show an appreciable contribution of diffractive processes to the total cross section ($\sim$ 25–40%), including double dissociation. The dominant process in diffractive scattering is single dissociation and has at high energies a very characteristic signature. One of the incoming particles emerges from the collision with a very small loss of its initial energy and is well separated in phase space from the other particle which dissociates into a multi–particle state. Diffractive events are thus characterized by a large rapidity [3] gap between the quasi-elastically scattered proton and the rest of the final state, where the rapidity is defined as

$$\eta = -\ln\tan\frac{\theta}{2}, \tag{1.50}$$

where θ is the polar angle relative to the initial direction of the incoming particles.

Large rapidity gap events have been also observed at HERA in the region where the photon emitted from the electron is almost real and known to behave like a hadron [13, 14]. Before embarking on a more detailed discussion of diffractive scattering in DIS at HERA, it is of interest to see whether diffractive dissociation initiated by a real (or quasi-real) photon follows the properties observed in hadron-hadron interactions.

1.8.3 Diffractive Dissociation in Photoproduction

In diffractive photoproduction reactions at HERA the electron is scattered under a small angle and emits a quasi-real photon. The interaction of the photon with the proton is then assumed to proceed in two stages. First, the photon fluctuates into a virtual vector meson, which then interacts with the target proton via Pomeron exchange. With this in

[3] "True" rapidity is not used in this work, and pseudo-rapidity is abbreviated to rapidity.

mind, the following processes contribute to diffractive photoproduction reactions:

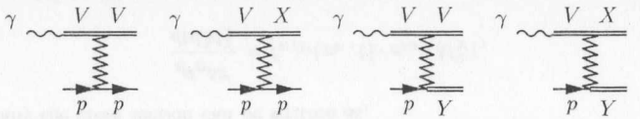

Both HERA collider experiments, ZEUS [16] and H1 [17], have studied photon diffractive dissociation in the photoproduction regime. The measurements were performed at a c.m. energy over an order of magnitude larger than in fixed target experiments [47].

The ZEUS experiments studied the M_X distribution at a fixed value of $W = 200$ GeV and obtained a Pomeron intercept value of

$$\alpha_{I\!P}(0) = 1.12 \pm 0.04(stat) \pm 0.08(syst),$$

in good agreement with the value from hadron-hadron data. The percentage of inelastic photon dissociation above the ϕ mass in the total cross section was found to agree with expectations of Regge factorization. In addition the Leading Proton Spectrometer detector of ZEUS was used to measure the t distribution associated with photon dissociation [48]. The measured t distribution was found to exhibit an exponential behavior. In the energy interval $176 < W < 225$ GeV and for masses $4 < M_X < 32$ GeV, the slope of the exponential t distribution was found to be

$$b = 6.8 \pm 0.9^{+1.2}_{-1.1}\text{GeV}^{-2}.$$

The H1 experiment has performed a measurement of single photon dissociation at two energies, $W = 187$ and 231 GeV. From the study of the energy dependence of the differential cross section which included the results of Chapin et al., [49] and from the M_X dependence they find that the triple-Regge formalism describes the data well. The extracted value of Pomeron intercept

$$\alpha_{I\!P}(0) = 1.068 \pm 0.016(stat) \pm 0.022(syst) \pm 0.041(model)$$

was found to agree with the value obtained from hadron-hadron interactions.

From these measurements it can be concluded that photon diffractive dissociation in photoproduction exhibits a similar pattern of behavior as observed for single diffractive dissociation in hadron-hadron interactions.

1.9 Diffractive Deep Inelastic Scattering

As discussed above many features of high energy hadron-hadron and photon-hadron diffractive interactions are successfully described by the triple-Regge formalism and lend much support to the hypothesis of factorization. However, Regge formalism, which describes global aspects of soft interactions, offers no insight into the microscopic structure or identity of the Pomeron. In the language of QCD we can imagine Pomeron as a color singlet combination of partons such as a pair of gluons, but in order to probe its contents a hard scattering is necessary.

It has been suggested that if the Pomeron has partonic structure, then such structure could be probed in diffractive hard scattering interactions [8, 9, 10]. By hard scattering we mean that there is at least one large scale in the problem that gives the possibility of applying perturbative QCD. In the case of diffractive DIS this is the photon virtuality, Q^2. Requiring the photon virtuality in the interaction to be large the dynamics of diffraction can be investigated and compared to perturbative calculations. The experimental signature of a Pomeron exchange would consist of a large rapidity gap in the hadronic final state, located between the photon fragmentation region and the proton.

The observation of events with a large rapidity gap in the final state produced in deep inelastic ep interactions reported by the ZEUS [11] and H1 [12] Collaborations has thus opened a whole new area of studies in QCD. Since then many workshops were organized with the aim to discuss the basic theoretical ideas and predictions for diffractive phenomena within the QCD framework and to improve the understanding of HERA data.

In the following we will concentrate on discussing single diffractive dissociation phenomena and in particular the dissociation of the virtual photons on a proton target in the presence of at least one large scale. The interpretation of these inclusive reactions as DIS on Pomeron in the language of QPM and QCD are presented and discussed.

1.9.1 Diffraction in the Quark Parton Model

In the QPM there is no mechanism of producing large rapidity gaps, other than by fluctuations in the hadronization process. Therefore, in the QPM diffractive dissociation as such has to be introduced by hand.

I. The Aligned Jet Model

The presence of diffractive dissociation in DIS was predicted by Bjorken based on the aligned-jet model (AJM) [50]. In the AJM, virtual-photon proton scattering at high energies (small x) is considered in the proton's rest frame. In this frame the virtual photon, whose energy, q_0, is the largest scale, fluctuates into a $q\bar{q}$ pair at a large distances, $l_c = 1/2M_p x = q_0/Q^2$, from the proton. For the HERA energy range this 'coherence length' can be as large as 1000 fm. The transverse size of the pair on arrival at the proton is $b_T^2 \approx 1/k_T^2$.

If any configuration of the virtual-photon fluctuation were to contribute to the total cross section in a universal manner, as in hadron-hadron scattering, the cross section for $\gamma^* p$ interaction would violate scaling properties of the structure function F_2. Bjorken solved this puzzle by postulating that only certain configurations of the virtual-photon fluctuation were allowed to contribute to the cross section while the others were not.

In the allowed configurations, in which one of the quarks carries most of the momentum of the photon a large transverse distance develops between the fast and the slow quark by the time they arrive at the proton. This large system, in which the pair is initially 'aligned' along the direction of the original photon, essentially interacts with the proton like a hadron. The latter interaction, being of hadronic origin, can proceed through diffractive dissociation. This will happen only if the $q\bar{q}$ lives long enough to evolve into a hadronic state - that is at high energies. Since the slow quark is almost on shell, the AJM is similar to the parton model. Therefore Bjorken was able to predict that at high energy, even in the QPM picture diffraction will reappear.

In the AJM, diffractive scattering remains a soft phenomenon and thus the Regge phenomenology applies as in the hadron-hadron scattering, corrected for the presence of a virtual photon.

II. Formalism of Diffractive DIS in QPM

In analogy to the DIS cross section, the four-fold differential cross section for ep scattering can be written as

$$\frac{d^4\sigma^D}{dx_{I\!P}\,dtdQ^2dx} = \frac{2\pi\alpha^2}{xQ^4}\left[1+(1-y)^2\right]F_2^{D(4)}(x,Q^2,x_{I\!P},t), \tag{1.51}$$

where for the sake of simplicity we have omitted the contribution from the longitudinal structure function. The superscript D denotes the diffractive process and thus the cross section described is no longer totally inclusive.

Ingleman and Schlien [8] suggested on the basis of expectations from Regge theory that the diffractive structure function could be factorized as follows:

$$F_2^D(x,Q^2,x_{I\!P},t) = f_{I\!P/p}(x_{I\!P},t)\cdot F_2^{I\!P}(\beta,Q^2), \tag{1.52}$$

where $f_{I\!P/p}(x_{I\!P},t)$ is the Pomeron flux factor and parameterizes the emission of $I\!P$ from the proton vertex and the second term $F_2^{I\!P}(\beta,Q^2)$ is called the Pomeron structure function.

In the Ingelman-Schlein approach the deep inelastic ep diffractive scattering proceeds in two steps. First a Pomeron is emitted from the proton and then the virtual photon is absorbed by a constituent of the Pomeron. This is depicted schematically in the following diagram:

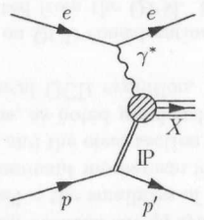

Under the assumption of factorization it is natural to treat the Pomeron as an effective hadron, that is an object containing partons. However, it is unclear whether the partons within the Pomeron should obey the momentum sum rule. The partonic interpretation of a factorizable Pomeron leads to the identification of $F_2^{I\!P}(\beta,Q^2)$ with the parton density functions in the Pomeron, $f_{i/I\!P}(\beta,Q^2)$, such that

$$F_2^{I\!P}(\beta,Q^2) = \sum_i e_i^2\cdot\beta f_{i/I\!P}(\beta,Q^2) \tag{1.53}$$

where the sum is over all the different partons. Because the Pomeron is self-charge-conjugate and an isoscalar the density of any flavor of q is expected to be equal to the density of the corresponding $\bar{q}$, i.e. $f_{i/I\!P} = f_{\bar{i}/I\!P}$.

It would be natural to assume that the strange quark density is the same as that of the u and d quarks. However, the Kp total cross section is smaller than the πp cross section, suggesting a possible suppression of strange quarks. For heavier quarks, it may be

assumed that their density can be dynamically generated by QCD evolution. Obviously the issue of the strange and heavy quark component depends on the real nature of the Pomeron, a subject which is discussed in the next section.

1.9.2 Diffraction in QCD

Some properties of diffractive dissociation make it a very interesting study ground for QCD. Diffractive processes lead to the presence of large rapidity gaps in the final states while in QCD, in which fragmentation is driven by parton radiation, large rapidity gaps are exponentially suppressed, see figure 1.10. To understand diffraction in QCD one has to invoke new coherent phenomena.

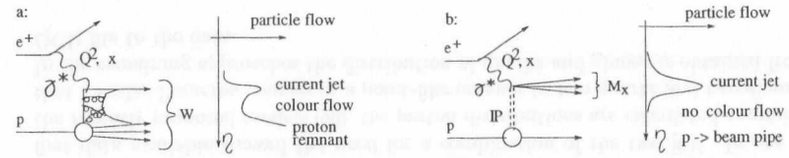

Figure 1.10: *a) Deep inelastic scattering. b) Diffractive deep inelastic scattering.*

In QCD the concept of the Pomeron still remains mysterious. The ideas about the nature of the Pomeron range from a simple diagram with two gluon exchange [4, 5] to a sophisticated gluon exchange whose properties depend on the nature of the interaction. The BKFL Pomeron [34], called sometimes hard or perturbative Pomeron, would consist of a ladder of (reggeized) gluons. From the theoretical point of view it becomes essential to analyze various processes in terms of which type of 'Pomeron' could be probed. The QCD picture of the Pomeron points to its non-universal nature.

There is a consensus that understanding of the nature of the Pomeron will help to establish the missing link between the short-range and long range strong interactions. Diffractive scattering is the obvious laboratory to study the properties of Pomeron exchange.

I. Interplay of soft and hard physics

Together with the high-parton density physics of the low x regime of ep scattering at HERA, came the realization that the hard physics studied till now is the result of an interplay of hard and soft phenomena. In case of deep inelastic scattering the unknown soft physics is hidden in the initial parton distributions which are parameterized at a relatively low scale $Q_0^2 \sim 1\text{GeV}^2$. In particular it is not clear whether the fast rise of F_2 with decreasing x is due to the QCD evolution or to the presence of a large parton density at a low scale.

The ability to separate clearly the regimes dominated by soft or by hard processes is essential for exploring QCD both at a quantitative and qualitative level. A typical example of a process dominated by soft phenomena is the interaction of two large size partonic configurations such as two hadrons. A process which would lend itself to a fully perturbative calculation, and therefore hard, is the scattering of two small size heavy onium-states each consisting of a heavy $q\bar{q}$ pair [51].

In deep inelastic scattering the partonic fluctuations of the virtual photon can lead to configurations of different sizes. The size of the configuration will depend on the relative transverse momentum k_T of the $q\bar{q}$ pair. Small size configurations (large $k_T \sim Q/2$) are favored by phase space considerations. In the QPM, in order to preserve scaling, it was necessary to suppress their presence by making them sterile. In QCD there is a simple explanation for this suppression - the effective color charge of a small size $q\bar{q}$ pair is small due to the screening of one parton by the other and therefore the interaction cross section will be small. This phenomenon is known as color transparency.

The essence of color transparency is expressed in the formula for the interaction cross section of a $q\bar{q}$ with a hadronic target T [52] which follows from the factorization theorem for hard processes in QCD,

$$\sigma(q\bar{q}T) \propto b^2 \, xG_T(x, b^2), \tag{1.54}$$

where b is the transverse separation between the $q\bar{q}$ system and G_T stands for the gluon distribution in the target. At small x the smallness of the cross section is compensated by the large gluon density. The dominant mechanism for diffractive scattering of a small size $q\bar{q}$ pair is two gluon exchange and the cross section can be calculated in perturbative QCD. For large size configurations, as noted previously, one expects the regime of soft interactions, modified by the typical QCD evolution. Here the Ingelman-Schlein type model would be applicable.

This qualitative picture based on QCD considerations leads to a picture of diffraction very different from the one expected from the QPM. The origin of a large rapidity gap may be either of perturbative nature or due to soft processes. The Pomeron exchange is non-universal and exhibits very different energy dependences for different initial photon configurations. Processes dominated by hard scattering are expected to have a faster energy dependence than those dominated by soft processes. The establishment of the validity of this approach has important consequences for the theoretical understanding of QCD.

II. QCD inspired models of LRG production

Since the first results of HERA were presented, the scientific community is burgeoning with ideas about the possible origin of hard diffraction and probable consequences. It is therefore not possible to give a complete and fair review. Instead we will present a broad classification and concentrate on discussing in more details the most popular approaches.

a. Regge factorization and QCD

There is a class of models which follow the original idea of Ingelman and Schlein [8]. The cross section for diffractive scattering is assumed to factorize into a Pomeron flux and the Pomeron is assumed to consist of partons whose densities have to be determined directly from the data.

This approach has led to a plethora of theoretical papers in which the parton content of the Pomeron at some small starting scale, Q_0^2, is treated in various physically motivated ways. The DGLAP [31] equations of pQCD are then used to investigate the evolution with Q^2 of these parton densities.

Originally the use of the DGLAP equations was believed to be inapplicable for the description of diffractive structure function because the presence of the gap makes it impossible to sum over all possible final hadronic states. Their use in this context was

at the level of a plausible assumption. Only recently the QCD factorization theorem was proven to hold for the leading twist diffractive structure function of the proton in DIS [53], giving support to this approach. The Regge factorization of these diffractive parton densities is an additional assumption and leads to their universal description.

A large group of physicists have explored such an approach [9, 54, 55, 56, 57, 58, 59, 60]. They differ in the way one of the three major ingredients are treated: the Pomeron flux, the evolution equation and the initial parton distributions.

- Pomeron flux:
  In most models the Pomeron flux parameterization is assumed to be given by the Regge-inspired fits of pre-HERA data [9]. One notable exception is the approach of Capella at al. [56] which postulates that the bare Pomeron flux has to be determined at large Q^2 when screening corrections are unimportant. Therefore $\alpha_{I\!P}(0)$ is Q^2 dependent and increases from $\alpha_{I\!P}(0) \simeq 1.08$ at $Q^2 = 0\text{GeV}^2$ to $\alpha_{I\!P}(0) \simeq 1.2$ at $Q^2 \sim 10\text{GeV}^2$ as determined from fits to the inclusive F_2 measurements.

- QCD evolution:
  Two groups [59, 57] have explored the possibility that the Pomeron is a photon-like particle and the DGLAP evolution equation acquires an extra term in which the Pomeron couples to quarks with a point-like coupling. The presence of this term leads to an enhancement of large β for the Pomeron structure and its $\log Q^2$ increase at all β values, contrary to the standard DGLAP evolution in which, due to radiation, the large β partons are depleted at the expense of an increase at lower β values.

- Initial parton distributions:
  In the early days the parton distributions were assumed either to have a hard distribution $\beta(1-\beta)$ [9, 8] compatible with a purely quarkonic Pomeron or a very soft one $(1-\beta)^5$ [54, 8] derived from the gluon distribution in the proton. The first data available showed the need for a combination of the two [61]. In one of the recently proposed models [60], the parton distributions are calculated assuming that a scalar Pomeron couples in a point-like manner to two quarks and two gluons. In the remaining approaches the distribution of quarks and gluons is obtained from QCD fits to the data.

b. Color dipole interactions

Since in low x interactions it is rather the $q\bar{q}$ fluctuation of the photon which interacts with the target proton, it is natural to view the interaction as that of a color dipole with the proton. Originally this approach was advocated by Nikolaev and collaborators [62]. For leading twist contributions the concept of color dipole can be extended to more complicated hadronic states [63].

For diffractive scattering the dipole interacts with the proton through two-gluon exchange. The models differ in the way the two-gluon exchange is handled in QCD [64, 63]. Since there is no guarantee that the approach can be fully perturbative, the uncertainties are absorbed into effective parameterizations, whose parameters are derived from the inclusive DIS scattering.

Bialas and Peschansky [65] have extended the dipole approach assuming that the proton also consists of color dipoles. The $\gamma^* p$ interactions are viewed as quasi-onium-

onium scattering. The BFKL dynamics is used to describe the interaction of dipoles, with numerical estimates tuned to describe the F_2 measurements of the proton.

In these models the Pomeron is non-universal and cannot be represented by a single flux. Common to this approach is the prediction of a dominant contribution of the longitudinal photon to the large β spectrum. The low β spectrum is populated by a $q\bar{q}g$ configurations of the photon, while the $q\bar{q}$ configuration of the transversely polarized photon populates the intermediate β region.

c. Perturbative QCD approach

In the perturbative QCD approach diffractive scattering is modeled through the coupling of t-channel gluons in a color singlet state to the photon [66, 67, 68]. For small mass diffraction the final state consist of a $q\bar{q}$ pair, while large mass diffraction includes an additional gluon in the final state, $q\bar{q}g$. The dynamical content of these models differ in the treatment of QCD corrections and in the choice of the gluon density. In many respects the results are similar to the results obtained within the dipole approach.

d. Semi-classical approach and soft color interactions

The physical picture is very similar to Bjorken's aligned-jet model. As in the AJM, the dominant process is the fluctuation of the virtual photon into different kinematical configurations of partons which then interact with the proton target. The basic idea of the semi-classical approach is to treat the proton at small values of x as a classical color field localized within a radius $1/\Lambda_{QCD}$ [69, 70]. The deep inelastic scattering is then viewed as a scattering of the system of fast quarks and gluons off the classical color field. If, after the interaction, the partonic configuration is in a color singlet state, a diffractive final state with a large rapidity gap is produced. Otherwise, an ordinary non-diffractive final state is produced.

The approach has features similar to the more phenomenological model advocated in [71], in which diffractive events are kinematically dominated by single gluon exchange and non-perturbative soft color interactions (SCI) allow the formation of a color singlet final state. The main point is that diffractive and non-diffractive events differ only by SCI.

In the semi-classical approach to diffraction the notion of Pomeron does not really appear. Here, the large rapidity gaps are generated in the final state as a result of color reorientation of different virtual photon fluctuations into the color singlet state in the color field of the proton.

e. Summary

To summarize, a tremendous theoretical progress has been achieved since the first observation of large rapidity gaps in DIS. While the number of models may seem overwhelming, in fact in many respects they follow the same pattern and their validity is limited to specific regions. Their variety reflects the problem of the interplay of soft and hard QCD in diffraction, as well as the interplay of leading and higher twist effects.

Many of the presented models have predictions which can be tested experimentally, such as Regge factorization, the W and Q^2 dependence as well as the t dependence. The characteristics of the final states is another probe for the validity of the presented ideas.

1.10 Summary and Outlook

In deep inelastic electron-proton scattering, $e+p \to e+anything$, a new class of events was observed by ZEUS[16] and H1[17], characterized by the presence in the detector of a large rapidity gap in the fragmentation region of the proton. The properties of these events were found to be consistent with a diffractive production mechanism, which is described by the exchange of a colorless object with the vacuum quantum numbers, generically called the Pomeron (IP).

One of the features of this exchange in hadron-hadron collisions, usually considered as processes with one soft scale ≈ 1 fm, is the Pomeron pole factorization. This means that the high energy dependence of any hadronic cross section should be dominated by a universal Pomeron trajectory. This universal Pomeron trajectory, indeed provides a reasonable phenomenological description of the energy dependence of all total hadronic cross sections with $\alpha_{I\!P}(0) = 1.08$ and $\alpha' = 0.25$ GeV^{-2} as determined by global fits in [44].

In contrast to soft hadronic collisions, diffractive processes in deep inelastic scattering are determined by two different scales. The hard scale is supplied by the virtuality of the photon Q^2 and the soft scale on the proton side is determined by its size ≈ 1 fm. The predicted feature of two scale processes is the violation of the Pomeron pole factorization. Thus, in hard diffractive processes at high energy one may expect different energy dependence for cross sections and that the energy dependence may change as Q^2 increases.

HERA offers a unique opportunity to test these different features of soft and hard QCD diffractive processes, and in particular to measure the value of the Pomeron intercept $\alpha_{I\!P}(0)$.

The results presented in this thesis are based on data collected using the ZEUS detector during 1994 running period. In this period HERA collided 27.5 GeV positrons with 820 GeV protons.

Chapter 2

The ZEUS Detector at HERA

In this chapter we will briefly describe the HERA Collider and the ZEUS detector. In describing the detector we will focus on those components that are of particular relevance for this analysis. A description of the ZEUS trigger architecture is given at the end of the chapter.

2.1 The HERA Accelerator

The Hadron Electron Ring Accelerator, HERA, is the first lepton-proton collider in the world. It is designed to accelerate electrons or positrons and protons in the 6.3 km long ring to 30 GeV and 820 GeV, respectively. The purpose of HERA is to enable the investigation of DIS in a region of phase space not accessible thus far to previous experiments.

HERA is located near the main site of the DESY laboratory in Hamburg, Germany. A view of the HERA layout is depicted in figure 2.1.

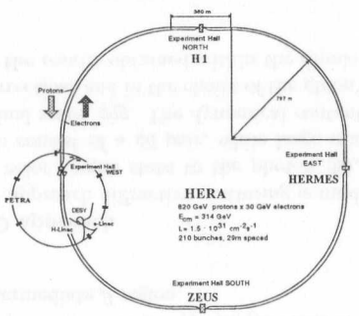

Figure 2.1: *The HERA accelerator complex at DESY, Hamburg.*

In the 1994 data-taking period HERA operated at a proton energy of 820 GeV and an electron energy of 27.52 GeV, resulting in a center of mass energy $\sqrt{s}$ of 300 GeV. To reach an equivalent center of mass energy with a fixed target proton would require an electron beam of 48 TeV.

Parameter	Design Value	Average 1994
Proton energy E_p	820 GeV	820 GeV
lepton energy E_e	30 GeV	27.52 GeV
center-of-mass energy $\sqrt{s}$	314 GeV	300 GeV
$\mathcal{L}_{\text{spec}}$ (cm^{-2}s^{-1}mA^{-2})	$3.2 \cdot 10^{29}$	$5.5 \cdot 10^{29}$
$\int \mathcal{L}$ (pb^{-1})/year	30	6.2
bunches ($ep + e + p$)	210	(153+15+17)
bunch crossing time	96 ns	96ns
p bunch current	0.8 mA	0.22 mA
e bunch current	0.3 mA	0.15 mA
$\#p$/bunch	$11.0 \cdot 10^{10}$	$3.1 \cdot 10^{10}$
$\#e$/bunch	$3.6 \cdot 10^{10}$	$2.6 \cdot 10^{10}$
I^e_{tot}/I^e_{pilot}	–	10.0
I^p_{tot}/I^p_{pilot}	–	10.1

Table 2.1: *A compilation of some of the HERA design parameters and their actual values during the 1994 running period.*

In the second half of the '94 running period it was decided to accelerate positrons instead of electrons in order to achieve longer lepton beam life times. For electrons a life time of only 2–3 hours could be achieved due to interactions with almost stationary positively charged ions, most likely originating from the "ion getter" pumps of the HERA vacuum system, which tend to defocus the electron beam. For a positron beam the pile-up of the ions is avoided due to the repulsive electromagnetic force of the positively charged positrons, thus extending the beam life time to about 8 hours. In the following, electron is used as a generic expression for the colliding lepton.

During this period HERA operated with 153 ep bunches with typical beam currents of 20-33 mA for electrons and 30-55 mA for protons. Besides these colliding bunches there were also unpaired (or *pilot*) 17 proton- and 15 electron-pilot bunches as well as 25 empty bunches. The pilot bunches can be used to estimate beam related background rates, while empty bunches allow the estimation of background rates originating from cosmic rays or to study the noise characteristics of detector components. The design and performance parameters of the HERA machine are summarized in table 2.1.

The integrated luminosity delivered by HERA has continuously increased, from about 30 nb^{-1} in the 1992 data taking period to almost 37 pb^{-1} in 1997, see figure 2.2. In 1994 HERA delivered 6.2 pb^{-1}. For about 2.6 pb^{-1} ZEUS was operational with all main components performing nominally. The present analysis is based on this data set.

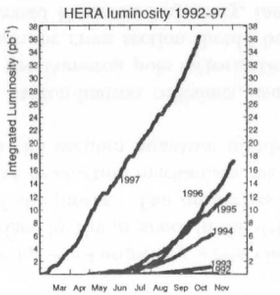

Figure 2.2: *HERA delivered luminosity.*

2.2 The ZEUS Detector

The design, construction and operation of the ZEUS detector owes its successes to the hard work of almost 500 physicists and as many members of technical staff. This multinational collaboration is an assembly of more than 50 institutes coming from 12 different countries. The main detector, weighing 3600 tones and standing 12 meters in height, is located 30m underground in the South Experimental Hall of the main HERA ring.

The coordinate system of ZEUS is defined as a right-handed system with the origin at the nominal interaction point (IP). In this system, the incoming proton direction, referred to as the forward direction, defines the z-axis and the x-axis is defined to point horizontally towards the center of HERA. Thus, the proton beam polar angle is 0°, whereas the electron beam polar angle is 180°. The azimuthal angle ϕ is measured w.r.t the positive x-axis (see figure 2.3).

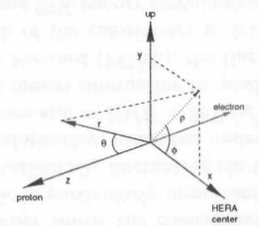

Figure 2.3: *The ZEUS coordinate system.*

ZEUS is a multi-purpose solenoid detector with a solid angle coverage of > 99.6% of 4π srad consisting of inner tracking detectors surrounded by a high resolution Uranium Calorimeter and a muon detection system. A longitudinal cross section through the detector showing the main components is presented in figure 2.4. The asymmetry of the detector on either side of the interaction point reflects the large momentum imbalance between the colliding beams.

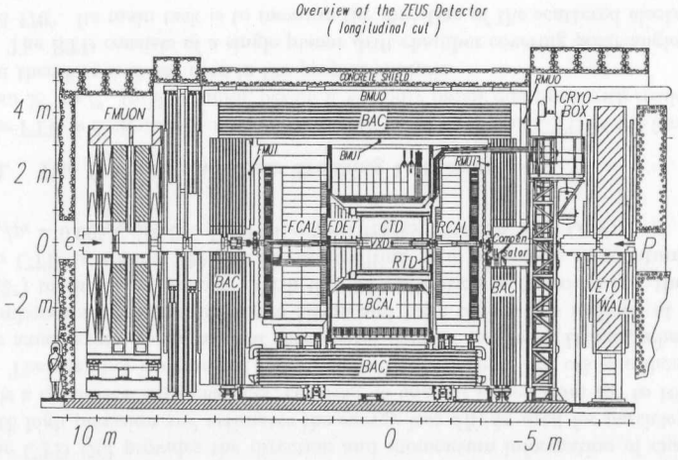

Figure 2.4: *The longitudinal view of the ZEUS detector. The main components are labeled and the directions of the incoming beam electrons and protons are also shown.*

The complete and detailed descriptions of the ZEUS detector may be found in the original technical proposal [74] and subsequent status report [75]. The components of the detector essential for the present analysis are described in more detail in the following sections. A brief description of the ZEUS detector is given below.

Starting radially outward from the interaction point are the tracking detectors; the vertex detector (VXD) and a large drift chamber for charged particle identification and measurement (CTD). The CTD is surrounded by a super-conducting magnet providing a field of 1.43 T. Forward and rear tracking chambers (FTD and RTD) provide extra tracking information in the forward and rear directions. The tracking chambers are surrounded by a high resolution Uranium Calorimeter (UCAL). The UCAL is divided into three main sections; the FCAL in the forward (proton) direction, the BCAL a barrel section surrounding the central region and the RCAL in the rear (electron) direction. The UCAL is enclosed by muon chambers (FMUI, BMUI and RMUI) on the inner side of an iron yoke. The yoke itself serves as an absorber for the backing calorimeter (BAC), which measures the energy of late-showering particles and also provides the return path for the solenoid magnetic field flux. On the outer side of the yoke, the outer muon chambers are installed (FMUO, BMUO and RMUO). Downstream of the main detector in the electron direction at $z = -7.5$ m an iron-scintillator Vetowall is used to reject beam-related backgrounds. The C5 beam monitor, a small lead-scintillator counter, located around the beam pipe at $z = -3.15$ m, is used to determine the nominal interaction point and monitor the proton and electron bunch shapes from timing measurements. Upstream of the interaction point, the proton remnant tagger (PRT), a lead-scintillator counter, located at $z = 5.1$ m around the beam pipe provides information about high energy charged particles which are produced at very small angles and leave the main detector through the beam hole. The leading proton spectrometer (LPS) installed at intervals along the beam line (20-90 m) and forward neutron calorimeter (FNC) located at about 100 m in the forward direction detect protons and neutrons scattered through a very small angles, respectively.

The short time interval of 96 ns between the bunch crossings at HERA results in a nominal rate of 10 MHz. ZEUS employs a three-level triggering system to reduce the rate to a few Hz, a level at which data can be written to tape.

2.2.1 The Tracking Detectors

The inner tracking detectors of ZEUS are positioned inside the superconducting solenoid and are dedicated to charged particle detection and identification. They are comprised of the Vertex Detector (VXD), the Central (CTD), Forward (FTD) and Rear Tracking Detector (RTD).

I. The Vertex Detector

The primary tasks of the VXD are the detection of shorted-lived particles and via additional hit information the improvement of the momentum and angular resolution of charged particles measured with the CTD alone. The VXD is a cylindrical drift chamber, covering an angular region from 8.6° to 165°. The spatial point resolution in the $r\phi$ plane is approximately 50 μm.

II. The Central Tracking Detector

The CTD [76] provides the direction and momentum information of charged particles with high precision and estimates the energy loss dE/dx used for particle identification. It is a cylindrical drift chamber, covering an angular region from 15° to 164°.

The chamber is organized radially into 9 superlayers. The odd-numbered superlayers are axial layers and have their sense wires parallel to the CTD axis, whereas the even-numbered superlayers are stereo layers and have their wires inclined at a small angle (±5°) to the chamber axis. With the '94 calibration of the chamber, the resolution of the CTD is around 230 μm in $r\phi$, resulting in a transverse momentum resolution of $\sigma_{p_t}/p_t = 0.005p_t \oplus 0.016$ for 9 superlayer tracks, where p_t is in GeV.

III. The Forward and Rear Tracking Detectors

The FTD is designed to extend the acceptance of VXD and CTD in the forward direction from 28° to 7°. In '94 running period it was only partly equipped with readout electronics and therefore it is not used in the present analysis.

The RTD consists of a single planar drift chamber covering polar angle between 160° and 170°. Its main task is to measure the direction of the scattered electrons in low Q^2 events.

2.2.2 The Uranium Calorimeter

The Uranium Calorimeter (UCAL) [77] is one of the most essential detector components at ZEUS for the reconstruction of ep-scattering events and plays a crucial role in the present analysis. The UCAL is a sampling calorimeter, consisting of alternating layers of depleted uranium as absorber and scintillator as active material for readout purposes. The thickness of the plates (2.6 mm scintillator and 3.3 mm = 1 X_0 uranium) has been chosen such that the calorimeter response to electrons and hadrons is the same ($e/h = 1 \pm 0.02$) over a wide range of energies, or in other words the calorimeter is said to be compensating. The compensation characteristic is particularly important for energy resolution of hadrons as hadronic showers have a statistically fluctuating electromagnetic component. The energy resolution of the ZEUS calorimeter, measured under test beam conditions, is $\sigma(E)/E = 18\%/\sqrt{E} \oplus 1\%$ for electrons and $\sigma(E)/E = 35\%/\sqrt{E} \oplus 2\%$ for hadrons, where energy is measured in GeV, and $\oplus$ means summation in quadrature.

The calorimeter is divided into three parts, the Forward (FCAL), the Barrel (BCAL) and the Rear (RCAL) (see figure 2.4). The depth of the calorimeter is determined by the maximum jet energy it needs to absorb, requiring 99% energy containment [74]. This energy is a function of polar angle, ranging from about 800 GeV in the forward direction, to about 30 GeV in the rear. The containment of very energetic jets is achieved by surrounding the uranium calorimeter by a much cheaper iron backing calorimeter.

The FCAL, covers polar angles from 2.2° to 36.7°. It is divided into 24 modules numbered with increasing x, each module is further segmented into 20 × 20 cm^2 towers numbered with increasing y. The towers are segmented in depth into an electromagnetic section (EMC) and two hadronic (HAC) sections. Each of the hadronic sections of a tower is identified as a calorimeter cell. The EMC section, however, is divided vertically into four 20 × 5 cm^2 cells. The structure of the RCAL is very similar. However, the EMC section has two 20 × 10 cm^2 cells instead of four and there is only one hadronic section.

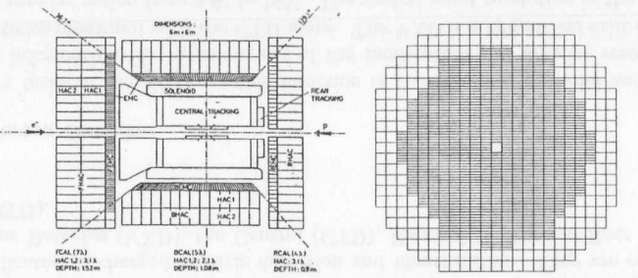

Figure 2.5: *The view of the CAL geometry (left) and FCAL face seen from the IP (right).*

The RCAL covers polar angles between 129.1° to 176.5°. In the outer region of the F- and RCAL are the HAC0 cells. There is no need for a finely segmented EMC sections there, as these regions are shadowed by the BCAL. The view of the UCAL geometry and FCAL face seen from the IP are shown in figure 2.5.

The BCAL covering the angles between the FCAL and the RCAL, consists of 32 wedge-shaped modules and has one EMC and two HAC sections. The modules are tilted 2.5° in ϕ. Each module is divided into 14 towers along the z-axis. The four EMC cells of each tower are projective in θ, where the HAC sections behind them are not projective.

Each calorimeter cell is read out on opposite sides by two photomultiplier tubes (PMTs) coupled to the scintillators via wavelength shifters. Comparison of the two PMT signals allows the determination of the impact point of the particle within a cell.

The calorimeter is calibrated on a channel-by-channel basis using the natural radioactivity of the depleted uranium, which provides stable and time independent reference signal. This calibration procedure is good to 1%. The PMTs can be calibrated via light emission of known intensity from LEDs. The rest of the electronic readout chain is calibrated using test pulses.

The calorimeter also provides accurate timing information with a time resolution better than about 1 ns for energy deposits greater than 4.5 GeV.

2.2.3 The Small Angle Rear Tracking Detector

The SRTD, has been implemented and installed at the beginning of the 1994 with three goals in mind.

- To improve the position measurement for the scattered electron.
- To correct for electron energy loss in an inactive material in front of the RCAL.
- To provide a rejection based on timing at the FLT level.

SRTD is a scintillator strip detector at the face of the RCAL ($z = -148$ cm) and covers an area of 68 × 68 cm^2 around the RCAL beam-pipe hole [78]. In this region inactive material (cables, flanges, *etc...*) causes particles to preshower and lose energy before reaching the calorimeter. The energy deposited in the SRTD can thus be used to correct for energy losses in inactive material, or in other words the SRTD serves as a presampler.

Figure 2.6 shows a schematic diagram of the detector layout. Charged particles are detected by two planes of orthogonally arranged (x, y) strips with a 1 cm pitch which provide position and pulse height information via an optical fiber-photomultiplier readout. Each plane is divided into four quadrants as shown in the figure.

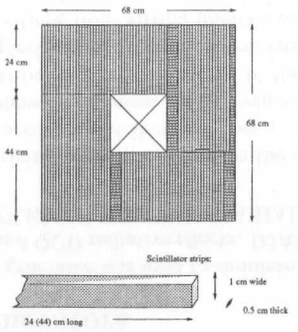

Figure 2.6: *Schematic diagram of the SRTD.*

SRTD hit information is used in conjunction with hits from the CTD for track reconstruction. The SRTD is also used for background rejection by providing a fast timing measurement ($\sigma_t \sim 2$ ns) to the trigger, complementing the rejection provided by the C5 and VETOWALL counters at the FLT level.

2.2.4 The Luminosity Monitor

The precise measurement of the time-integrated luminosity is a crucial aspect of all cross sections. The ep luminosity at HERA is measured by the luminosity monitor using the rate of hard bremsstrahlung photons, $ep \to e'p\gamma$ from the Bethe-Heitler process [79]. The cross section for this process is high and is known from theoretical calculations to an accuracy of 0.5%.

The luminosity monitor [80] consists of two calorimeters, the electron calorimeter (LUMI-e) and the photon calorimeter (LUMI-γ).

The LUMI-e is a lead-scintillator calorimeter. It is located at $z = -34$ m and detects electrons that have lost part of their energy via bremsstrahlung and are deflected from the nominal beam orbit by the magnetic field of HERA. The geometrical acceptance is limited to the detection of electrons with $0.2 \cdot E_{beam} < E'_e < 0.8 \cdot E_{beam}$. The energy resolution is $\sigma(E)/E = 18\%/\sqrt{E}$ with E measured in GeV.

The LUMI-γ is a lead-scintillator calorimeter situated at $z = -104$ m and is protected against synchrotron radiation by a 3.5 X_0 carbon/lead filter. The energy resolution which under test beam conditions is $18\%/\sqrt{E}$, where E is in GeV, is reduced to $25\%/\sqrt{E}$ by the filter.

The measured luminosity uncertainty in '94 data taking period was found to be about 2%, where the dominant sources of errors are due to energy scale uncertainties, cross section calculation, acceptance correction and beam gas background subtraction.

2.3 The ZEUS Trigger and Data Acquisition System

The short bunch crossing time at HERA of 96 ns, equivalent to a rate of approximately 10 MHz, is a technical challenge and puts stringent requirements on the ZEUS trigger and data acquisition system.

ZEUS employs a sophisticated three-level trigger system in order to select ep physics events efficiently while reducing the rate to a few Hz [81, 82]. A schematic diagram of the ZEUS trigger system is shown in figure 2.7.

The First Level Trigger (FLT) is a hardware trigger, designed to reduce the input rate below 1 kHz. Each detector component has its own FLT, which stores the data in a pipeline, and makes a trigger decision within 2 μs after the bunch crossing. The decision from the local FLTs are passed to the Global First Level Trigger (GFLT), which decides whether to accept or reject the event.

If the event is accepted, the data are transferred to the Second Level Trigger (SLT), which is software-based and runs on a network of Transputers. It is designed to reduce the rate below 100 Hz. Each component can also have its own SLT, which passes a trigger decision to the Global Second Level Trigger (GSLT) [83]. The GSLT decides then to accept or reject the event. If GSLT accepts the event then it is passed to an Event Builder.

The Event Builder [84] collects data from all detector components into a single event record and transfers it to the Third Level Trigger (TLT), which makes a decision based on the complete information. The TLT is software-based and includes parts of the offline reconstruction code. It runs on a farm of Silicon Graphics computers and is designed to reduce the rate to a few Hz.

Events accepted by the TLT are written to tape via a fiber-link (FLINK) connection. The size of an event is typically 100 kBytes. From here on events are available for full offline reconstruction and data analysis.

The trigger logic used for the online selection of DIS events, on which the present analysis are based, is described in chapter 4.

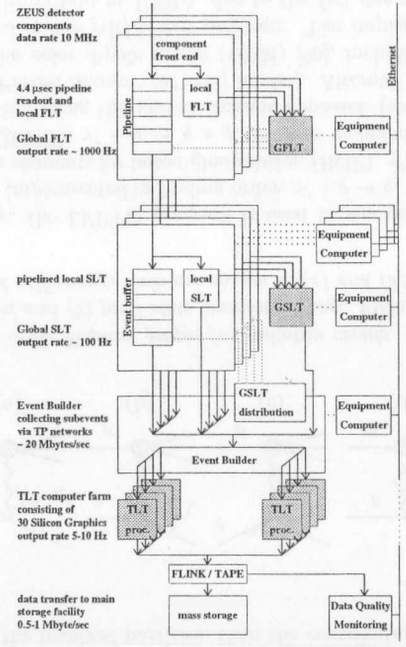

Figure 2.7: *Schematic diagram of the ZEUS trigger and data acquisition system.*

Chapter 3

Monte Carlo Event Simulation

The Monte Carlo (MC) method provides approximate solutions to a variety of mathematical problems by performing statistical sampling experiments on a computer. The method is called after the city in the Monaco principality, because of a roulette, a simple random number generator. The name and the systematic development of Monte Carlo methods dates back to the beginning of this century.

With the advent of high energy colliders and modern, highly complicated detectors the use of Monte Carlo technique for event generation and detector simulation became indispensable. Now-days, Monte Carlo simulations in high energy physics, are seen as an easy and flexible procedure for experimentalists to compare data and theory, in a way that allows arbitrarily complicated cuts to be applied to the data. Furthermore, and most importantly, Monte Carlo detector simulations are the only reliable way to understand detector responses and determine acceptances in todays experiments.

The MC simulation of the physics events in the ZEUS experiment consists of two main parts. In the first part, the *ep*-scattering process is simulated, focusing on the event kinematics and the final state event topology. The second part simulates the detector and trigger response to the constellation of outgoing particles according to the detector geometry and test beam results for different components.

In the following, the main concepts of the different simulation stages and their implementation in software packages are described.

3.1 Deep Inelastic Event Generators

In the present analysis, the DJANGO6 [85] event generator was used to simulate deep inelastic $ep \to eX$ scattering, including both QED and QCD radiative effects. DJANGO6 is an interface of the Monte Carlo programs HERACLES [86], LEPTO [87], ARIADNE [88] and JETSET [89].

In the first stage, HERACLES generates underlying kinematics based on the standard model electroweak cross sections, and takes into account contributions from a whole set of electroweak radiative processes. Figure 3.1 shows the lowest order Feyman graphs for emissions from the electron line. These contributions are the source of the largest corrections. In the diagrams (a) and (b) the simplest graphs for real photon emission at the leptonic vertex and in (c) and (d) the contributions from virtual photons associated with the leptonic vertex are shown. The radiative corrections coming from the hadron line (not shown) are less important, since these corrections are small due to the dependence on

the squared charge of the involved particles, than the contributions of photons radiated off the electron line.

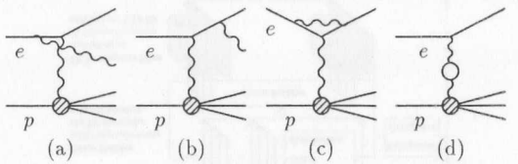

Figure 3.1: *The lowest order Feyman graphs for radiative events. This corrections can be classified into (a) initial and (b) final state bremsstrahlung. Virtual corrections at lepton vertex and the so-called self energy term are shown in (c) and (d).*

In the second stage, the LEPTO program is used to simulate the hard scattering reaction, which is fully implemented in leading order, $\gamma^* + q \to q$. QCD corrections using exact first order matrix elements for boson-gluon fusion (BGF), $\gamma^* + g \to q + \bar{q}$, and QCD Compton scattering (QCDC), $\gamma^* + q \to q + g$, are also included, and higher orders in leading $\log Q^2$ are treated using the parton cascade approach (sometimes referred to as 'Matrix Element plus Parton Shower' (MEPS) model). Alternatively, the QCD cascade can be described by the color dipole model (CDM) [90], including boson-gluon fusion (BGF), as implemented in the ARIADNE program. The implementation of the BGF process is particularly important at HERA, due to the fast rise of the gluon density at low-x.

The CDM differs from the MEPS model in its approach of describing the partonic final state. It correctly treats most QCD coherence effects by describing the gluon bremsstrahlung in terms of radiation from color dipoles between partons, instead of treating partons as independent emitters.

In the last stage, the final QCD cascade partons need to be hadronized. This cannot be described by perturbation theory, since the strong coupling constant α_s becomes large. Thus the hadronization has to be described by a phenomenological procedure. The JETSET program following the LUND [91] string fragmentation model is therefore used to perform the hadronization of cascade partons and obtain colorless hadrons in the final state.

Figure 3.2 illustrates the partonic processes of the event simulation in an inelastic lepton nucleon scattering, leading to the hadronic final state. When a quark is scattered out of the proton, it leaves behind a colored remnant, since the struck parton itself carries color. Thus there are color strings between the partons of the hard interaction and the proton remnant. This picture of deep inelastic lepton nucleon scattering is being referred to here and in literature as *standard deep inelastic scattering* or *non-diffractive DIS*.

In order to estimate the contamination and understand the migration effects of non-diffractive events in the diffractive sample, we have generated non-diffractive DIS events with $Q^2 > 3$ GeV^2. The CDM+BGF model was used to simulate QCD parton cascade. This model at present provides the best description of the hadronic final state, as was observed in [92]. The parton densities of the proton were chosen to be the MRSA [93] set, which adequately represents ZEUS structure function results.

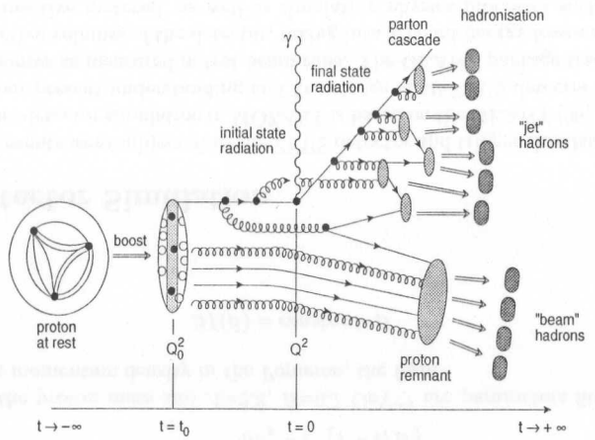

Figure 3.2: *Artistic illustration of the $\gamma^* p$-scattering process, showing different stages in the simulation of the hadronic final state.*

3.2 Diffractive Event Generators

Diffractive processes can be described in terms of the exchange of a Pomeron (IP) with vacuum quantum numbers. These types of processes, as depicted in figure 3.3, are not included in the simulation of the hadronic final state, as implemented in *standard* Monte Carlo models for deep inelastic scattering. In order to model the DIS hadronic final states for diffractive interactions where the proton does not dissociate,

$$e + p \rightarrow e + X + p,$$

the Monte Carlo event generator RAPGAP [94] was used.

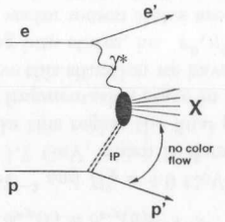

Figure 3.3: *Diagram of a diffractive event.*

The RAPGAP event generator follows the idea of Ingelman and Schlein. The beam proton emits a Pomeron with a probability $f_{\mathbb{P}/p}(x_{\mathbb{P}}, t)$, and is assumed to behave as a (virtual) hadron. The Pomeron, thus, is described by an effective structure function $F_2^{\mathbb{P}}(\beta, Q^2)$, which is independent of the process of emission, and its constituents then take part in a hard scattering process with the virtual photon.

The RAPGAP generator is interfaced with HERACLES for simulation of QED radiative processes. The leading order as well as first order QCD matrix elements for gluon

radiation and boson-gluon fusion are implemented and higher order QCD cascades are treated using leading $\log Q^2$ parton shower or CDM+BGF approach. The hadronization is performed using the Lund string model.

To study the acceptance and smearing effects due to the finite resolution of the measurement, two samples of events with $Q^2 > 3$ GeV^2 and the CDM+BGF model for QCD parton cascades were generated with RAPGAP. The first sample corresponds to the ZEUS parameterization of the Pomeron structure function which was obtained in the previous analysis [95],

$$F_2^{\mathbb{P}}(\beta, Q^2) = \sum_{q_i} e_i^2 \beta f_q(\beta, Q^2) = \beta(1-\beta) + \frac{c}{2}(1-\beta)^2,$$

where c=0.57. This parameterization assumes no Q^2-dependence. Furthermore, we assumed that the Pomeron is made of u, d and s quarks with equal strength, which leads to symmetric parton densities in the Pomeron,

$$\beta f_q(\beta) = \beta f_{\bar{q}}(\beta) = \frac{9}{12} \cdot \{\beta(1-\beta) + \frac{c}{2}(1-\beta)^2\}$$

with $q = u, d$ and s quarks. In deriving the above parton densities we did *not* make an assumption that the partons in the Pomeron should fulfill the momentum sum rule. This parameterization will be referred to as ZPD93.

The second sample of events corresponds to Hannes Jung's (HJP1) parameterization of the Pomeron structure function based on the H1 preliminary measurement of 1994 $F_2^{D(3)}$. The starting parton distributions of the form

$$\beta f_q(\beta) = A \cdot \beta^{\gamma} \cdot (1-\beta)^{\alpha}$$

for the quarks and

$$\beta f_g(\beta) = B \cdot \beta^{\mu} \cdot (1-\beta)^{\delta}$$

for the gluon were assumed at an initial scale of $Q_0^2 = 4$ GeV^2, from which they were evolved to higher Q^2 using the next-to-leading order Altarelli-Parisi equations in perturbative QCD. In the fit, the momentum sum rule was not imposed. Figure 3.4 shows parton densities as obtained from the QCD fit by H. Jung.

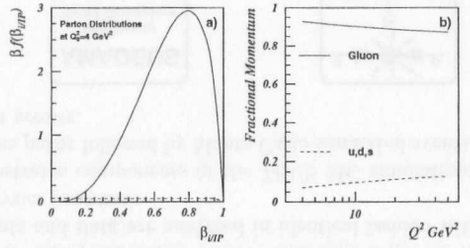

Figure 3.4: *(a) Momentum weighted parton distributions of quarks and gluons in fractional momenta $\beta_{q/\mathbb{P}}$ and $\beta_{g/\mathbb{P}}$ for diffractive exchange, averaged over $x_{\mathbb{P}}$ and t as extracted from the QCD fit at $Q_0^2 = 4$ GeV^2; (b) fraction of the total momentum carried by quarks and gluons as a function of Q^2.*

The Pomeron flux factor of Streng [10] was taken for both MC samples, in the form

$$f^S_{\mathbb{P}/p} = \frac{\delta^2_{\mathbb{P}p}(t)}{16\pi} \cdot x_{\mathbb{P}}^{1-2\alpha_{\mathbb{P}}(t)}$$

where $\alpha_{\mathbb{P}}(t) = \alpha(0) + \alpha'_{\mathbb{P}}\, t$ with $\alpha_{\mathbb{P}}(0) = 1 + \epsilon$ and $\alpha' = 0.25$. The parameter ϵ was taken to be 0.085 for the first sample and 0.139 for the second. For the Pomeron-proton vertex the ansatz

$$\delta_{\mathbb{P}p}(t) = \delta_{\mathbb{P}p}(0) e^{-\frac{1}{2}R_N^2 t}$$

was used with $\delta^2_{\mathbb{P}p}(0) = 58.74$ GeV^{-2} and $R_N^2 = 4.0$ GeV^{-2}.

The low mass region $M_X < 1.7$ GeV, which is dominated by vector mesons is *not* modeled correctly in RAPGAP. In this region the final partons are assigned (collapsed) to a random meson state during fragmentation stage in JETSET, i.e. $\pi^0, \eta^0, \omega, \rho, \eta', \ldots$, with equal probability. To improve this situation we have modified routines in RAPGAP and JETSET such that collapsing into states, i.e. $\pi^0, \eta^0, \eta', \ldots$, were forbidden and the ratios for collapsing into allowed vector meson states are given by VDM model.

For systematic checks we have also used a MC sample generated by POMPYT [96]. POMPYT like RAPGAP, is a MC realization of a factorizable model for high energy diffractive processes, within the PYTHIA [97] framework. The initial-state radiation effects were handled by PYTHIA, and are based on a next-to-leading-order exponentiated description (see PYTHIA manual, p. 81). The probability for finding a Pomeron in the proton, the Pomeron flux factor, was taken as that of Donnachie and Landshoff [44]

$$f_{\mathbb{P}/p}(x_{\mathbb{P}}, t) = \frac{9\beta_0^2}{4\pi^2}[F_1(t)]^2 x_{\mathbb{P}}^{1-2\alpha_{\mathbb{P}}(t)}$$

where $\beta_0 = 3.24$ GeV^{-2} is the effective Pomeron-quark coupling, and the Regge trajectory as above $\alpha_{\mathbb{P}}(t)$ with $\epsilon = 0.085$ and the slope $\alpha' = 0.25$. The elastic proton form factor $F_1(t)$ is given by

$$F_1(t) = \frac{4m_p^2 - At}{4m_p^2 - t}\left[\frac{1}{1 - t/B}\right]^2$$

where m_p is the proton mass and A=2.8, B=0.7 GeV^{-2} are parameters fitted to data. For the quark momentum density in the Pomeron, the form

$$\beta f(\beta) = constant \cdot \beta$$

was used.

3.3 Detector Simulation

All generated events were subjected to the ZEUS detector and trigger simulation program MOZART. The detector simulation in MOZART is based on the GEANT [98] package and incorporates our present understanding and knowledge of all ZEUS detector components and their responses as measured in test beam runs. The GEANT package tracks particles through the active volumes of the detector, taking into account energy losses and multiple scattering in inactive material, as well as simulating physics processes such as particle decays in flight. The ZEUS trigger decision is based on signals from different components

and is implemented in the program ZGANA [99], which flags events with pass/fail as specified by ZEUS trigger requirements. Monte Carlo simulated events and ZEUS raw data are then processed by the offline reconstruction package ZEPHYR. From this stage on, both MC events and data are analyzed in identical fashion with EAZE, an analysis shell for user's physics program.

Figure 3.5 illustrates components of the ZEUS MC simulation, reconstruction, and analysis chain. The paths followed by Monte Carlo simulated events(left) and data(right) are indicated with arrows.

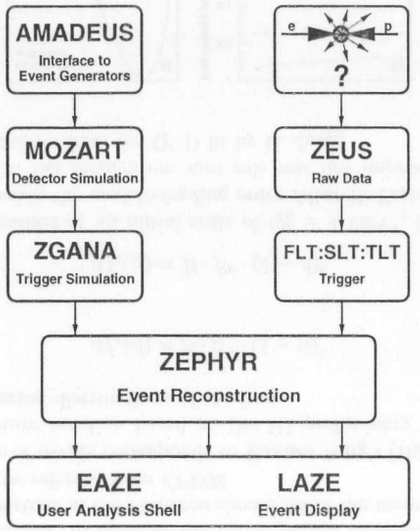

Figure 3.5: *Diagram of the ZEUS Monte Carlo, reconstruction and analysis chain.*

Chapter 4

The Data Sample

In this chapter we will concentrate on the preselection of Deep Inelastic Scattering (DIS) events collected during the '94 data taking period. At ZEUS a neutral current DIS event is defined by the presence of the scattered electron in the final state within the acceptance of the calorimeter ($Q^2 \gtrsim 4$ GeV^2), see figure 4.1. This simple signature thus provides clear guidance for the design of the trigger and the choice of the preselection cuts.

The DIS events represent only a small fraction of the interactions which occur in the ZEUS detector. There are numerous other processes, some from genuine ep interactions and others from non-ep interactions, which occur at a much higher rate and are considered here as background to the DIS sample. For example the trigger rate due to upstream interactions of the proton beam with residual gas in the beam pipe is of the order of $10 - 100$ kHz, while the rate of interesting ep physics events in the ZEUS detector is of the order of a few Hz. Therefore the role of the data preselection is to isolate the interesting ep processes from the other interactions, and to flag a sample of DIS candidates. This task is performed by the ZEUS three-level trigger system.

In this chapter, we will discuss the backgrounds contaminating the DIS sample, followed by the methods used for their recognition and rejection. Then we give a brief description of the ZEUS trigger logic, followed by a discussion of the resulting reduction of event rates.

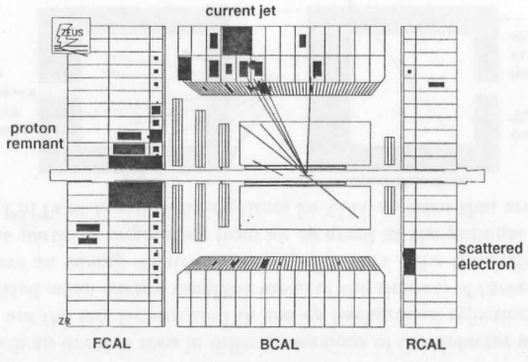

Figure 4.1: *Deep Inelastic Scattering event in the ZEUS detector for $Q^2 = 310$ GeV^2.*

4.1 Backgrounds

Photoproduction

The main source of background to the DIS sample is due to photoproduction events. In photoproduction events the electron is scattered at a small angles and escapes undetected down the rear beam-pipe ($Q^2 \lesssim 4$ GeV^2). Most of these events are rejected by requiring an electron to be identified in the final state. However, sometimes low energy hadrons may fake the energy deposit of an electron and thus lead to a wrong classification of the event as DIS candidate. This latter contamination becomes most serious at high W, but it is substantially reduced by rejecting events with a low energy scattered electron candidate or by means of the energy-momentum conservation cut described in section 4.3.

p-gas

Collisions of the proton beam with residual gas in the beam-pipe are responsible for the so called p-gas background. The p-gas rate is sensitive to the vacuum conditions, the flux of protons in the beam and the composition of the residual gas. p-gas events produce activity in the detector occur at a rate of about 50 kHz. This background is substantially reduced by applying the timing cuts and momentum conservation cut. The remaining contamination from p-gas events is estimated from the rate of events occurring during the p-pilot bunch crossings and later statistically subtracted from the final sample.

e-gas

Collisions of the electron beam with residual gas in the beam-pipe produce the so called e-gas background. This background is reduced by applying the timing cuts. The remaining background contamination is estimated as in the p-gas case from the e-pilot bunch crossings and statistically subtracted from the final sample. Background from synchrotron radiation is less serious and is effectively reduced by the use of absorbers and beam collimators as described in [74].

Beam halo

Protons in the beam halo interact with the beam-pipe wall or other beam-line components producing secondary particles which travel close to the direction of the proton beam. Many of these are penetrating muons. This background is very effectively removed by recognizing the characteristic pattern of energy deposition in the calorimeter, as well as by using calorimeter-timing information.

Cosmic muons

The cosmic muon activity in the ZEUS detector has a rate of about 5 kHz. Cosmic muons can be removed by applying cuts on the timing or on the characteristic pattern of energy deposition they leave in the calorimeter and CTD. Some of these events may produce energy deposits in the CAL which might pass all selection cuts and thus enter into the analysis. This remaining contamination from cosmic muons can be estimated by counting selected events coming from empty bunch crossings and scaled by the ratio of the number of empty bunches to the number of colliding bunches.

4.2 Timing Rejection Algorithms

The time at which an event is seen in different sections of the detector and the pattern of energy deposits are the key factors used in non-ep background rejection algorithms. The times are calculated as an energy weighted mean of the times t_i of those photomultipliers (PMTs) that have an energy deposit exceeding 200 MeV. The time offsets for all PMTs are set such that particles originating from an ep event at the nominal interaction point are recorded by PMTs at $t_i = 0$, yielding times for CAL sections that are on average zero.

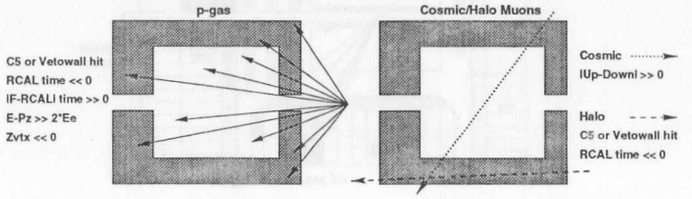

Figure 4.2: *Sketch of p-gas and cosmic/halo muon signatures in the ZEUS detector.*

The signatures for the beam-gas and muon backgrounds mentioned earlier are illustrated in figure 4.2. The illustrations show how the times at which particles from background events hit the detector, and background event topology give rise to their clear and recognizable identification. The beam-gas and beam-halo backgrounds can be efficiently removed by a cut on the average CAL section times (t_F, t_R) and on their differences. The calorimeter is also divided into upper and lower halves providing two additional times (t_{up} and t_{down}), which are used in rejection of cosmic muons. The information from C5 and/or Vetowall is also used to remove these backgrounds [100].

4.3 Momentum Conservation

An important variable that characterizes an ep event is the conserved quantity δ defined by

$$\delta \equiv \sum_i (E - p_z)_i = \sum_f (E - p_z)_f \tag{4.1}$$

where the first sum runs over initial and second sum runs over final state particles. For ep events where all final state particles are detected, $\delta = 2 \cdot E_e$. The measured δ distribution will be broader due to measurement errors, initial state radiation and/or particles escaping undetected down the rear beam-pipe. The latter two of these will lead to a long tail towards smaller δ values for the DIS spectrum. Since the positive z-direction has been chosen to point in the proton direction, particles which escape down the forward beam-pipe have $E - p_z \approx 0$ and therefore give a negligible contribution to the sum.

Different final states measured in the ZEUS detector produce different δ distributions; therefore δ is a good discriminator against background processes. For DIS events where the electron is contained within the calorimeter, we expect $\delta \approx 2 \cdot E_e$. In contrast, p-gas events occurring inside or upstream of the main detector produce very low or unphysically high values of δ. Photoproduction events where the scattered electron stays in the beam pipe, but which are selected because a hadronic energy deposit has been falsely interpreted as the scattered electron, predominantly give low values of δ. Therefore, vetoing events with low or high δ values is a very effective rejection procedure against these backgrounds.

4.4 The ZEUS Trigger

As was mentioned in the introduction to this chapter, the main characteristic of a DIS event is the presence of the scattered electron in the final state within the acceptance of the calorimeter. All three trigger stages described below for DIS events are therefore entirely based on the properties of the electron signal in the calorimeter. The timing, pattern recognition and δ-cut are used exclusively for background rejection.

First Level Trigger

The FLT triggers required for events to be selected as a DIS candidates are summarized below:

- RCAL-IsoE The IsoE [101] trigger flags events with isolated electromagnetic energy deposit (*e-candidate*) in the RCAL by searching a group of up to 4 trigger towers with $E_{EMC} > 2.5$ GeV that are surrounded by *quiet* trigger towers.
- REMCth The REMCth trigger flags events with a total electromagnetic energy deposit in the RCAL > 3.75 GeV, *including* the towers around the beam-hole.
- REMC The REMC trigger flags events with a total electromagnetic energy deposit in the RCAL $>$ 2.0 (3.4) GeV, *excluding* the towers around the beam-hole.
- BEMC The BEMC trigger sums the energy deposits from the entire BCAL EMC-section and flags events that have more than 4.8 GeV.

A three-fold veto based on information from the C5, Vetowall and SRTD was also implemented. Events satisfying a logical .OR. of the above FLT slots and *not* firing in coincidence with any of the above three vetos are passed to the second level trigger.

Second Level Trigger

At the SLT stage, longer times and more detailed component information are available to apply more complex and flexible veto algorithms. These algorithms mainly use calorimeter information and are summarized below:

- Timing The beam-gas and beam-halo backgrounds are efficiently removed by a loose cut on the average CAL section times and on their differences, see figure 4.3(a).
- Sparks This veto is used to reject so-called *spark* events from the FLT sample. These events are characterized by a sudden discharge in one of the PMTs. These events are recognized by a large energy imbalance in one cell while the rest of the calorimeter remains quite.
- Cosmics Cosmic muon events are removed by considering the time difference between the upper and lower halves of the calorimeter, see figure 4.3(b).
- δ This veto is used to reject events with unphysically large values of δ. The maximum δ that an ep event may have is $\sim 2 \cdot E_e$. These events are mainly due to beam-gas and are vetoed if $(E - P_z)_{CAL} > 75$ GeV; see figure 4.3(c).

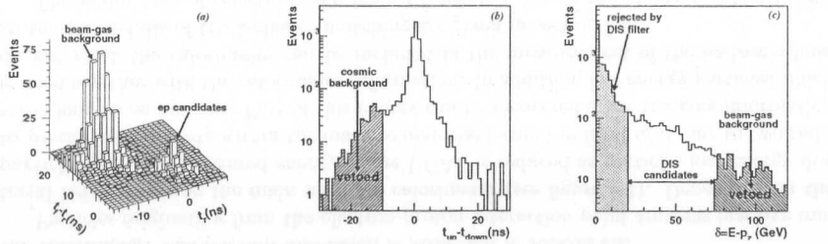

Figure 4.3: *SLT distribution for pass-through events: (a) $t_{FCAL} - t_{RCAL}$ versus t_{RCAL} times. The peak at the origin which is well separated from the background contains the events originating from the IP. (b) CAL $t_{up} - t_{down}$ times. The hatched area shows events rejected by the cosmic veto cut. (c) δ distribution at the preselection level. The hatched areas show events rejected by SLT DIS filter and δ veto.*

To select DIS event candidates at the GSLT level, the physics filter uses information from the calorimeter and LUMI-γ detectors. The filter is simply a cut on δ quantity,

$$\delta = \sum_i E_i \cdot (1 - \cos\theta_i) + 2 \cdot E_\gamma^{lumi} > 20\text{GeV},$$

where E_i is the cell energy, θ_i is the polar angle of the cell from the nominal IP, E_γ^{lumi} is the energy measured in the photon calorimeter, and the sum is over all calorimeter cells. The events with an initial state radiation photon, which is seen in the luminosity monitor, are also flagged as DIS candidates by inclusion of the second term in the above equation. This selection mainly rejects photoproduction events.

Third Level Trigger

The TLT veto filters take full advantage of more numerous components and more precise component information which are available at this level. The additional information allows imposing tighter rejection cuts than was possible at earlier levels and, as well, to apply pattern recognition algorithms to make further background rejection. The physics filter for selecting DIS events at TLT requires at least one of the electron identification algorithms 'Local' [102] or 'Elec5' [103] to find an electron candidate with $E_e' \geq 4$ GeV and increases the SLT δ cut to 25 GeV. This cut further rejects photoproduction events. The rejected event, if not selected by another physics filter, is discarded; otherwise the event is written to tape for offline reconstruction.

4.5 The Data Summary Tape

The events stored on tape are later reconstructed offline with the ZEUS reconstruction package, ZEPHYR. During the offline reconstruction complete information for the detector components becomes available. This information permits stricter selection cuts to be made and more complex physics filters to be implemented. This was not possible during earlier stages due to time limitation. The main DIS selection at this level uses the reconstructed event vertex to compute the δ quantity correctly. The information characterizing the given event is recorded in one of the four trigger words. The event record together

with the trigger words is then written out to a disk in a reduced format, the so-called mini Data Summary Tape (DST). These trigger words make subsequent selection of events with desired characteristics very fast and efficient.

Luminosity delivered by HERA and recorded on tape (gated) by ZEUS in the '94 running period is shown in Table 4.1. The less than optimal performance of essential detector components during data taking further reduced gated luminosity to the so-called *evtake* sample. The *evtake* selection requires that:

- The luminosity monitor is fully functional;
- The magnetic field is on;
- The CTD is at full high voltage with no large dead regions;
- The UCAL is operational without a significant number of dead channels.

After the offline reconstruction phase an extensive Data Quality Monitoring (DQM) is carried out to check the stability of event rates and various kinematic quantities as a function of run. Runs which show severe problems in the reconstruction of an important variable are identified and excluded from the analysis; the remainder form the so-called *distake* selection. For analysis presented in this thesis the final integrated luminosity is 2.6 pb^{-1}.

	$\mathcal{L}$ = nb^{-1}
HERA delivered	5106.372
ZEUS on tape	3301.972
evtake	2949.921
distake	2611.853

Table 4.1: *Breakdown of integrated luminosity in 1994.*

Chapter 5

Event Reconstruction

The standard ZEUS offline event output consists of reconstructed tracks of charged particles, the primary interaction vertex from the tracks and energy deposits and timing information for all the cells of the calorimeter which passed a minimum threshold cut. There are several experimental problems that make the reconstruction of event kinematics from the above information far from perfect. In this chapter we will describe the improvements we have made in the reconstruction of the events which minimize biases and improve the resolution of all the kinematic variables relevant for this analysis.

The depleted uranium of the ZEUS calorimeter provides a very stable and time independent signal which is used for monitoring of the photomultipliers (PMT) and setting the absolute calibration scale. This signal also leads to energy deposits within the UCAL which do not originate from ep interactions, which we denote as *noise*. Typically about 1 GeV of energy is deposited within the entire UCAL due to this noise contribution. Kinematic variables, mainly those which probe the hadronic final state (i.e. $M_X, y_{jb}, \ldots$), are affected by this component. Therefore, to improve reconstruction of the hadronic variables a reduction of the noise contribution is needed. In section 5.1 the details of the noise reduction procedure are further discussed.

So far, ZEUS diffractive analyzes, as well as many other analyzes, relied mainly on the high-resolution depleted-uranium scintillator calorimeter. All the variables based on the hadronic final state were reconstructed assuming that each calorimeter cell contributes as a massless particle. This approximation is in particular not appropriate for determination of small diffractive masses, since a typical single particle hadronic shower consists of more than 5 cells. By combining the cells as massless particles we introduce into the system a fake mass solely generated by the geometrical granularity of the calorimeter. The way out is to cluster the cells into calorimeter objects which correspond to single particles or jets of particles. In this study a new scheme for clustering cells has been developed, based on both topological and physical properties of hadronic and electromagnetic showers in the calorimeter. The relevant discussion is presented in section 5.2.

Particles originating from the electron-proton interaction point traverse inactive material before reaching the main uranium calorimeter (see figure 5.1). Depending on the particle types, the measured energy in the UCAL is reduced as particles lose energy due to preshowering effects within the inactive material located in front of it, one to two radiation lengths on average. Part of this energy can be recovered if the tracking information is used together with the calorimeter information. In addition, low energy particles which do not reach the calorimeter can be included in the measurement of the hadronic final state. The details of track-cluster matching are given in section 5.3.

The major task of selecting deep inelastic events relies on the ability to identify efficiently the scattered electrons in a wide range of energies. There are several experimental

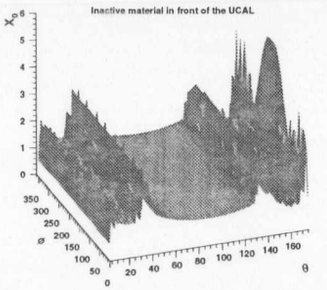

Figure 5.1: *Distribution of inactive material in front of the UCAL as implemented in the detector simulation package, in units of radiation length X_0 as a function of θ and ϕ.*

problems that make this task difficult. Particles scattered in the direction of the incoming electron, a configuration favored by the cross section, have low momenta. This configuration is typical for the low-x regime, where the final state electron is accompanied by the fragments of a low energy recoiling jet (see figure 5.2). As the particle energy decreases, it becomes harder to distinguish electron from pion showers based on the pattern of energy deposits in the calorimeter. This task is made even more difficult by the fact that the electrons are not isolated. A previously developed neural network based electron finder was used in this analysis. However, its efficient pattern recognition does not ensure a proper measurement of the electron energy which is biased by the overlaping hadronic debris. In addition, the hadronic energy attributed to the electron distorts the measurement of the invariant mass in the calorimeter. This problem is addressed in section 5.4.

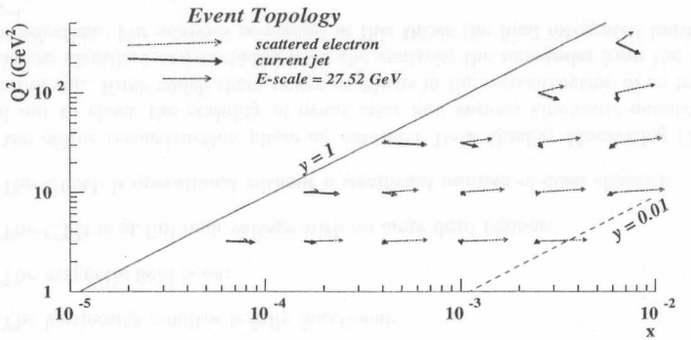

Figure 5.2: *Schematic representation of the opening angle in the LAB frame between the scattered electron and the current jet for various points in the $Q^2 - x$ plane.*

Dedicated studies of the energy scale of the calorimeter have shown a mismatch between the data and the MC simulation of the calorimeter response. The origin of this mismatch was found to be due to a combination of effects, partly due to the energy scale in the data and partly due to the MC simulation of showers. The relative normalization was established by comparing energies in the calorimeter with the corresponding tracking information. The details of this study are presented in section 5.5.

In the final step of the event reconstruction, the calorimeter clusters and tracking information are combined into physical objects corresponding to a single particle or a jet of particles with the optimal energy resolution. The strategy of the track-cluster association is discussed in section 5.6, where advantages of this approach are demonstrated.

5.1 Reduction of Uranium Calorimeter Noise

The uranium signal (UNO), denoted as pure *noise*, can be obtained from calorimeter calibration triggers. The MC noise parameterization is based on this information. Figure 5.3 shows the comparison of the cell UNO signal in the data and in the MC for all EMC, HAC1 and HAC2 cells. A very good agreement is observed. The measured energy distribution of the noise per cell is centered around zero and has an approximate Gaussian shape. The standard deviations of these spectra are ~ 18 MeV in the EMC sections and ~ 27 MeV for the HAC sections.

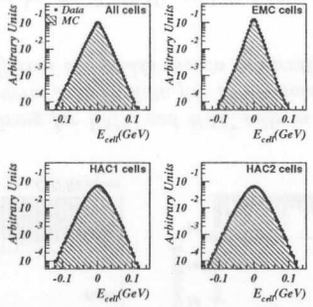

Figure 5.3: *Comparison of UNO signal for data and MC.*

During reconstruction, a standard noise suppression cut of 60 MeV for EMC cells, 100 MeV for HAC0 cells and 110 for HAC1/HAC2 cells is applied to the entire UCAL. After this cut, on average 6 EMC and 2 HAC noise cells per event still remain, from a total of 5918 cells. This remaining noise component will affect the reconstruction of the kinematic variables which probe the hadronic final state, in particular the M_X reconstruction of the low mass diffractive states. Therefore, in order to improve the reconstruction of the hadronic variables, we need to minimize the *noise* contribution coming from the ZEUS uranium calorimeter.

The study of noise reduction is pursued by selecting the so called *random trigger events*, which are taken during each run and sample the status of the UCAL in between ep interactions, wherein all energy deposits in the UCAL must be due to noise. The MC sample for this study was obtained by passing empty events through the ZEUS MC chain.

In figure 5.4 the noise distribution from random trigger events and the MC simulation are compared in terms of the number of cells which fire and the total energy deposited in the UCAL. The comparison between data and MC in figure 5.4(a, a') shows a clear disagreement, in contrast to the good agreement of the UNO signal for single cells as shown in figure 5.3. This difference is due to additional sources of noise, such as noisy or sparking PMT's, which are not simulated in the MC.

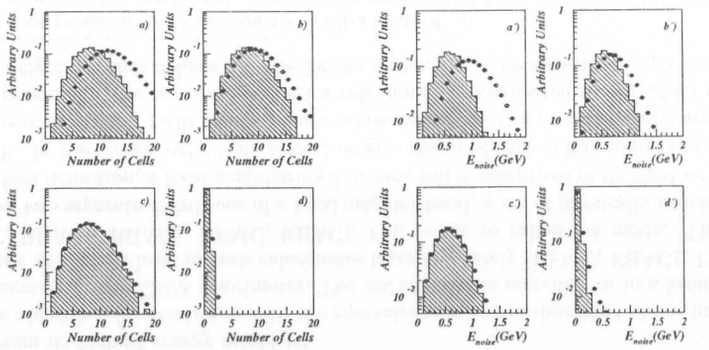

Figure 5.4: *Comparison between noise contribution for data (dots) and MC (histogram), in terms of the number of cells that fired and total energy deposited in the UCAL. (a,a') distributions after standard noise suppression. (b,b') distributions after removing mini sparks. (c,c') distributions after removing hot cells. (d,d') distributions after removing single isolated cells with energy below 120(160) MeV EMC(HAC).*

Mini sparks are due to faulty PMT's, and are identified by observing that an energy imbalance $Imb = E_l - E_r$ of the left (E_l) and right (E_r) PMT is directly proportional to the energy of the cell, $E_{cell} = E_l + E_r$. The striking difference between data and MC samples can be clearly observed in figure 5.5, where the correlation between the imbalance and the energy for single isolated cells is shown separately for random trigger and DIS data and MC samples, respectively. In the data sample we observe a clear correlation

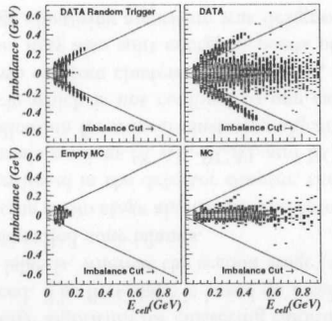

Figure 5.5: *Energy imbalance versus cell energy for single isolated cells taken from a random trigger and DIS event sample, separately for data and MC.*

between the imbalance and the energy for single isolated cells, which is not present in the MC sample. This difference is related to the fact that no mini spark simulation is implemented in the ZEUS detector simulation. In addition, in the MC sample the width of the imbalance distribution is narrower, indicating a deficiency in the simulation of energy sharing between the PMT's of individual cells. Mini sparks in data can be removed by introducing an energy dependent imbalance cut which is only applied to single isolated cells

$$|Imb| \; < \; 0.7 \cdot E_{cell}(\mathrm{GeV}) + 0.018(\mathrm{GeV}). \qquad (5.1)$$

The so called hot cells manifest themselves by firing with an unusually high frequency, well above the 3σ threshold cut. This behavior is attributed to cells where one PMT is dead and the second one is faulty. For these cells the energy of the dead PMT is set to the energy of the faulty one, thus resulting in an imbalance of zero at reconstruction time. In figure 5.6 the frequency of firing, i.e. the number of events in which a cell fired divided by the total number of events, for EMC and HAC cells for random trigger events and MC is presented. The hot EMC(HAC) cells are identified as those for which the frequency of firing is higher than 0.008(0.002) for FCAL and BCAL, and 0.005(0.002) for RCAL.

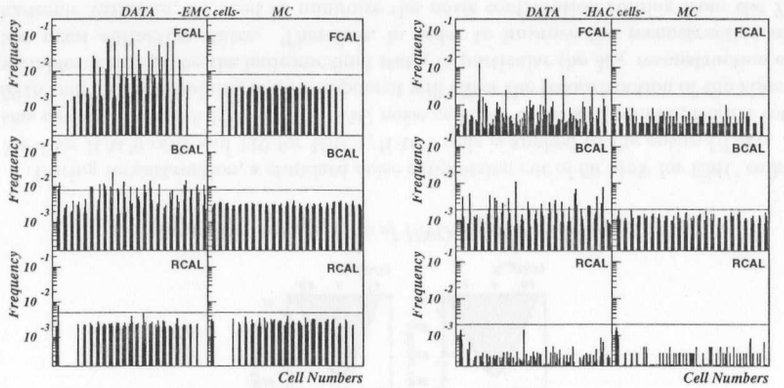

Figure 5.6: *Frequency of firing for EMC and HAC cells in selected random trigger data and empty MC. Clearly several cells in data fire at unusually high frequency (hot cells). The solid lines indicate different thresholds chosen to identify hot cells.*

After removing mini sparks, fig. 5.4(b,b'), and in addition hot cells, fig. 5.4(c,c'), the agreement between the random trigger sample and the empty MC is dramatically improved. Still, the average amount of *noise* contribution to an event is around 600 MeV. Therefore, a further reduction of noise contribution is needed. This is achieved by removing single isolated cells, in addition to the above 2 cuts, with energy below 120(160) MeV in EMC(HAC) sections. A further improvement is obtained as shown in figures 5.4(d,d').

To summarize, the following noise suppression cuts are applied to both data and MC:

- single isolated mini sparks are removed by requiring Eq. 5.1 to be fulfilled,
- single isolated hot cells are removed,
- single isolated cells with energy below 120(160) MeV EMC(HAC) are removed.

It is important to point out that the mini spark and hot cell suppression cuts do not affect the MC simulation.

5.2 Calorimeter Cluster Reconstruction

Particles entering the ZEUS calorimeter will shower and deposit their energy in several adjacent detector cells. The role of a clustering algorithm is then to merge cells which, in an ideal case, belong to the shower of a single particle. The formed clusters can then be classified. This classification is possible [105], since shower properties of electromagnetic particles are different from those of hadronic particles. Furthermore some clusters can be matched to charged tracks and replaced by them, thus permitting a broader spectrum of physics analysis as well as better determination of the kinematic variables.

In this section a two stage algorithm for clustering calorimeter cells associated with a particle or a jet is introduced. The first stage is based on local clustering with equivalence relations and leads to cell islands, whereas the second stage is based on global clustering, and is used to create the so-called cone islands.

The reason for introducing a two stage algorithm is dictated by the construction of the ZEUS calorimeter. As mentioned in the detector chapter, the calorimeter is divided into three, spatially separated main sections FCAL, BCAL and RCAL. This spatial separation introduces a serious complication for a local clustering algorithm in handling the energy deposits of a single particle which is not confined to one calorimeter section, since the energy will be split into two or more clusters. Furthermore, shower fluctuations, as well as the preshowering effects, may also split energy deposits of a single particle. To solve this problem a second stage clustering algorithm was designed[1].

5.2.1 The Cell Island Algorithm

The Cell Island clustering algorithm is based on two ideas. The ideas are to consider clustering in a local neighborhood only and to use an equivalence relation to assign cells to islands.

Consider each cell and its local neighborhood. If the cell has sufficient energy, it becomes a candidate to be connected with one of its neighbors. The connections are made to the highest energy nearest neighbor or to the highest energy next to nearest neighbor. This procedure is repeated for each cell and produces a unique assignment of a cell to an island. It is interesting to note that such a simple algorithm comes remarkably close to what would be done by eye. After all, it is hard to imagine a reason to separate a cell from its highest energy neighbor[2].

The algorithm for clustering with the equivalence relations described above has been implemented for the ZEUS calorimeter. The cell islands are searched for in a local neighborhoods at the cell level in each calorimeter layer separately (FEMC, FHAC1, FHAC2, BEMC, BHAC1, BHAC2, REMC, RHAC). This is the so called 2-d mode. The code provides two separate definitions of a local neighborhood, a set of physically nearby cells. In the first definition, a local neighborhood of each cell is comprised of its eight neighboring cells. In the second definition, a local neighborhood of each cell is comprised of only its nearest neighbors. Cells whose energy values are higher than its neighbors, are called "local maxima". The requirement that a cell should be connected to one of its highest energy neighbors, thus defines the *rule* for the connection. The algorithm implementation

[1]The strategy and the realization are due to Allen Caldwell.

[2]The shower profiles can be with good accuracy approximated by an exponential fall off from the shower maximum.

is shown schematically in figure 5.7 for two separate definitions of a local neighborhood, where arrows indicate the connection to the highest energy neighbor.

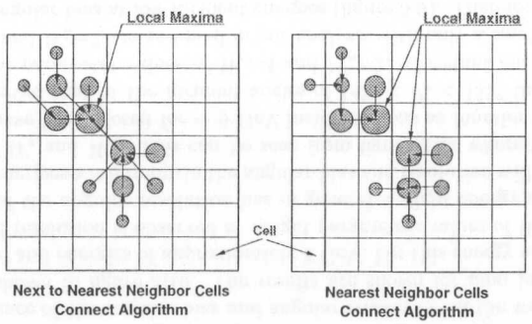

Figure 5.7: *Schematic representation of the cell island clustering.*

The global, detector dependent problem has been replaced by a simpler question of which connections to make in a specified local neighborhood. The detector dependence is essentially hidden in the definition of a local neighborhood. For the sake of simplicity the clusters thus formed will be called cellIslands in what follows.

5.2.2 The Cone Island Algorithm

As was mentioned in the introduction, the energy deposit of a single particle can often be split by the local clustering algorithm. Therefore, a second pass, the cone island clustering algorithm, has been suggested to collect the cellIslands which belong to a shower of a single particle or a jet of particles.

The cone island algorithm takes as input the cellIslands and performs a clustering in the $\theta - \phi$ space. The matching of cellIslands starts from HAC2 cellIslands and works inwards. For each HAC2 cellIsland, the angular separation to all HAC1 cellIslands is determined. This angular separation is translated to a probability according to a distribution determined from a single pion MC. The probability as a function of an angular separation is shown in figure 5.8. A link is made from the HAC2 cellIsland to the HAC1 cellIsland giving the highest probability, provided this probability is larger than a user supplied cut. If no valid link to a HAC1 cellIsland has been found, an attempt is made to link the HAC2 cellIsland directly to an EMC cellIsland. In a second step, a similar procedure is performed over HAC1 cellIslands and a valid link to an EMC cellIsland is searched for. In a third step, EMC cellIslands can be connected to other EMC cellIslands. A different probability cut can be applied for matching EMC cellIslands to each other.

Once the linking of cellIslands has taken place, the coneIsland information is generated by combining all calorimeter cells which point to the same EMC coneIsland. In the case of several EMC cellIslands being joined together, the seed cellIsland is the highest energy EMC cellIsland. The possible links are HAC2 $\rightarrow$ HAC1 $\rightarrow$ EMC, HAC2 $\rightarrow$ EMC, HAC1 $\rightarrow$ EMC, and EMC $\rightarrow$ EMC.

The two probability cuts for linking HAC2 $\rightarrow$ HAC1 (0.1) and HAC2 $\rightarrow$ EMC, HAC1 $\rightarrow$ EMC, and EMC $\rightarrow$ EMC (0.3) were chosen such as to give the best mass resolution for diffractive events.

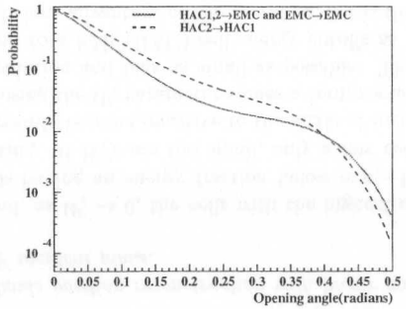

Figure 5.8: *The probability assigned to an angular separation as a function of the angular separation between the cellIslands (in radians).*

5.2.3 Cluster Position Reconstruction

In order to determine the angle for a given cluster it is necessary that both the vertex and the cluster position be accurately determined. In this section we turn our attention to the cluster position reconstruction, which is not only important for the calculation of angles but also for the track-cluster matching. The position reconstruction, described in this section, is applied to all calorimeter clusters associated with the hadronic final state. The scattered electron position reconstruction is discussed in section 5.4.3.

The usual method to estimate the cluster position is to calculate the center of gravity (COG) of the shower [106]:

$$\vec{r}_{COG} \equiv \frac{\sum_i w_i \vec{r}_i}{\sum_i w_i} \tag{5.2}$$

where $\vec{r}_i = (x_i, y_i, z_i)$ is the geometrical center of a cell i within the cluster and the weight factors w_i are taken as the energy E_i deposited in that cell. Together with the vertex position, the cone island angle can then be calculated.

The use of eq. 5.2 with linear energy weights yields systematic biases in the reconstructed cone island position. These systematic biases are due to the varying cells projectivity as seen from the vertex, which translate into systematic biases of the calculated cone island angle. This is seen in figure 5.9 where the difference, $\Delta\theta = \theta_{isl} - \theta$, between the calculated cone island angle (θ_{isl}) and the incident angle of a pion (θ), as well as the angular resolution as a function of the incident pion angle, are shown.

Rather than using linear energy weights, we propose to use eq. 5.2 with two modifications. First, since each calorimeter cell is read out on opposite sides by two PMTs, we propose to correct the geometric center of each cell, in one dimension, by the energy imbalance information. That is, we take $x_i = (x_0)_i + \delta x$ where $(x_0)_i$ is the geometric center of a cell and δx is given by

$$\delta x = \frac{\lambda}{2} \ln(\frac{E_R}{E_L}).$$

The expression for δx was extracted from the test beam data [105] with $\lambda = 54$ cm, where the formula was found to work properly within ± 8 cm from the center of a cell. In the outer regions close to the WLSs (< 2 cm) we take $\delta x = \pm 10$ cm, although it can be parameterized by a polynomial. Second, instead of taking weights which are linear in the

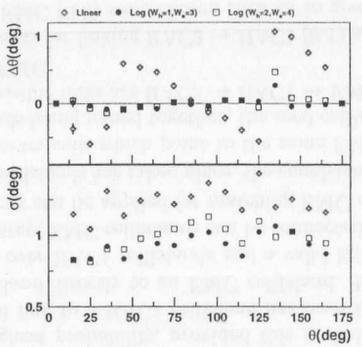

Figure 5.9: *coneIslands position reconstruction with linear and logarithmic weights for approximately 3 GeV incident pions.*

energy deposited in a cell, we propose following the suggestion in [107], to use weights given by the following expressions:

$$w_i(\mathrm{EMC}) = \max\{0, [W_e + \ln(\frac{E_i}{E_T})]\}$$
$$w_i(\mathrm{HAC}) = \max\{0, [W_h + \ln(\frac{E_i}{E_T})]\}, \quad (5.3)$$

where once again E_i is the energy deposited in a cell i, E_T is the total energy of the shower $E_T = \sum E_i$, and W_e, W_h are tuned parameters. The logarithmic energy weights take into account the exponential falloff of the shower energy distribution from the shower maximum. The reason for introducing two parameters W_e, W_h is to account for the different sizes of the EMC and HAC cells.

An example of the results obtained by using the corrected cell centers and logarithmic weights of eq. 5.3 in eq. 5.2 with (W_e=3,W_h=1) and (W_e=4,W_h=2) is shown in figure 5.9 as full dots and open squares, respectively. It is seen that the systematic biases as observed for the linear case have been substantially reduced together with a large decrease of the fluctuations in the calculated angle at a given incident angle (see figure 5.9).

The dependence of the angular bias and angular resolution on the weight parameters W_e and W_h is shown in figure 5.10. The results are shown for pion incident angles of $145° < \theta_\pi < 155°$ and energies of approximately 3 GeV. For this energy a minimum in the angular bias and resolution is observed at weight parameters values of W_e=3 and W_h=1. This minimum of the angular resolution has in general a slight energy dependence. For higher incident energies a minimum in the angular bias and resolution will occur at slightly higher values of W_e and W_h. This can be seen from figure 5.11 where the angular bias and resolution have been ploted for $\sim$ 6 GeV incident pions as function of incident pion angle. It is observed that at the incident angles of $145° < \theta_\pi < 155°$ the minimum now occurs for weight parameter values of W_e=4 and W_h=2. Constant energy independent values of W_e=4 and W_h=2 are assumed in our analysis with only a small loss in angular resolution and angular bias at low incident energies (figure 5.9). Therefore, the sensitivity of the choice of the W_e and W_h weight parameters on angular biases and resolutions have to be included in a systematic check of the physics results.

The observed dependence of the angular bias and resolution on the parameters W_e and W_h can be understood by inspecting eq. 5.3. The parameters serve two functions: first to

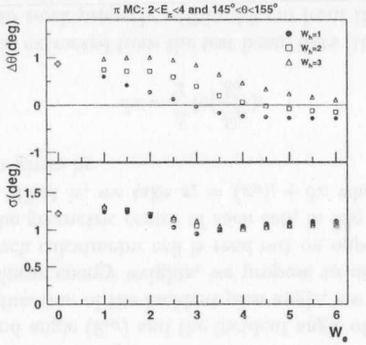

Figure 5.10: *The dependence of the angular bias and angular resolution on the weight parameters W_e and W_h for incident pions at the incident angles as indicated in the figure.*

define a threshold on the fraction of the total shower energy which a cell must exceed in order to be included in the position weighting, and secondly, to set the relative importance of the tails of the shower in the position weighting. As $W_i \to \infty$, all cells with energy above the detection threshold will be weighted equally, and so the calculated position will be the geometric centroid of the cells in the shower, and the angular resolution will be worse.

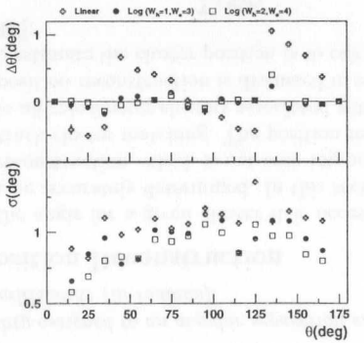

Figure 5.11: *coneIslands position reconstruction with linear and logarithmic weights for approximately 6 GeV incident pions.*

On the other hand, as $W_i \to 0$, the cells with the highest energy are weighted more heavily, whereas cells having an energy fraction below $\exp(-W_i)$ are excluded entirely from position weighting. If W_i's are too small, only a few cells dominate the position calculation and the results become sensitive to the angle of incidence.

Therefore, in choosing the W_i parameter values a compromise has to be made to keep both the angular resolution and bias as small as possible. The chosen values of W_e=4 and W_h=2 correspond to a EMC(HAC) cell energy cutoffs at 1.8%(13.5%) of the total shower energy. An obvious advantage of the use of eq. 5.3 is that on one hand the effect of shower fluctuations are damped by the logarithmic weighting, and on the other hand the agreement between the data and the MC simulation of shower shapes is less crucial.

5.3 Track-Cluster Matching

Track information has not been used so far in the reconstruction of the kinematic variables which depend on the hadronic final state. It is clear that the description of the hadronic final state can be improved if calorimeter clusters are replaced by the associated tracks when momentum is low. This is because for charged low energy particles the track's momentum and angle determination, as well as the resolution, are much more precise than that of the CAL. In order to perform the matching between calorimeter objects and tracks we have developed an algorithm based on the principle of the *Distance of Closest Approach* (DCA). A detailed description of the ZEUS track reconstruction package may be found in [104]. Here we present a brief overview of the track extrapolation to the calorimeter cluster COG.

Each track is extrapolated by the standard ZEUS software to the surface of the calorimeter. In this second step, tracks are further extrapolated into the calorimeter, assuming a linear trajectory given by the track momentum unit vector at the end of the helix swim (EHS). The distance of closest approach is defined as the shortest distance between a track trajectory and a calorimeter cluster:

$$\vec{L} = \vec{C}_{clus} - \vec{R}_{ehs} - S\hat{p},$$

where $\vec{C}_{clus}$ is the vector from the vertex to the calorimeter cluster COG, $\vec{R}_{ehs}$ is the vector from the vertex to the end of the helix swim, S is the swim distance and $\hat{p}$ is the track momentum vector direction at the EHS. The swim distance, S, is given by $S = (\vec{C}_{clus} - \vec{R}_{ehs}) \cdot \hat{p}$. The distance of closest approach is thus a function of cluster position, helix parameters and the swim distance:

$$\Delta_{DCA} \equiv |\vec{L}| = l(\vec{C}_{clus}, \vec{R}_{ehs}, \hat{p}; S). \tag{5.4}$$

The error associated with Δ_{DCA} can also be calculated.

The track-cluster association can now be based either on the distance of the closest approach or on a χ^2 probability. The choice of which matching method to use is dictated by the properties of the hadronic final state being analyzed. In the inclusive DIS sample the density of particles in the final state is high; the final state consists of the scattered lepton and approximately $\langle n_{prt} \rangle \propto \ln(W^2)$ particles on average. In these events the calorimeter clusters are mixed; some clusters are due to energy deposits of single particles whereas others are due to energy deposits of several particles, the so-called "*jet*" clusters. The resolution on the jet cluster position is not an appropriate quantity to be used in the χ^2 formula for matching purposes; rather, it is the lateral extent of the jet that is the relevant quantity.

In our analysis, in which we have to match tracks to both single particle clusters as well as to jet clusters, we have chosen to use the method based on the DCA selection criteria. Specifically, we say that a track and a cluster are associated if the following condition is satisfied:

$$\Delta_{DCA} \leq \max(r_{min}, r_{clus})$$

where r_{clus} is the radius of a cluster, calculated by projecting the cluster cells onto a surface perpendicular to a ray from the vertex to cluster COG, and r_{min} is a tuned parameter, determined from a test sample of single particles.

The r_{min} parameter value was extracted using a single pion MC sample. In figure 5.12 the efficiency of matching a single pion track to a calorimeter cluster is shown as function

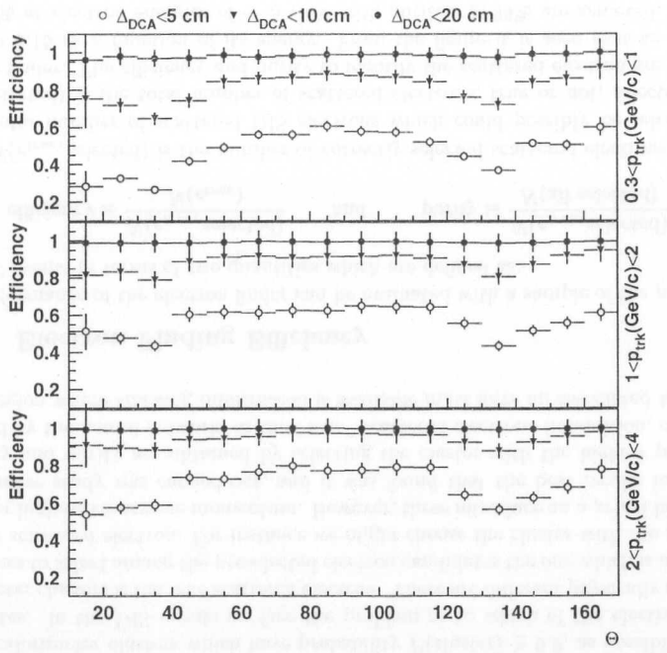

Figure 5.12: *Efficiency of matching calorimeter clusters and tracks for the single charged pion MC as a function of polar angle θ in three bins of p_{trk} and three DCA values.*

of the polar angle θ for three r_{min} parameter values and three track momentum ranges. From the figure it is seen that a high efficiency $\sim 100\%$ in the FCAL, BCAL and RCAL regions and $> 98\%$ in F/BCAL and B/RCAL super crack regions can be achieved for r_{min} parameter value of 20 cm at low track momenta, which grows to 100% for higher track momenta in the entire θ interval. Therefore, we adopt an r_{min} value of 20 cm with only a small loss in track cluster matching efficiencies at low incident energies in the F/BCAL and B/RCAL transition regions.

In figure 5.13 we show the probability density, or normalized number of track-cluster matches per unit area, as a function of distance of closest approach for inclusive DIS data and single pion MC. The data matches were selected by requiring a DCA to be less than 30 cm and $E_{clus}/p_{trk} \leq 1$, where the latter condition is imposed to reject matches for which E_{clus} could contain energy of particles not associated with the track. It is seen that, for both inclusive DIS data and a single pion MC, the distributions peak at $\Delta_{DCA} \sim 0$ cm and have an approximate half Gaussian shape.

The half widths of the distributions show an obvious θ and energy dependence. The widths are wider at smaller energies than at higher energies. They are narrower in the central region than in the forward and backward regions where the amount of inactive material is greater. Furthermore, it is seen that the agreement between data and MC is good, where the small discrepancies are possibly due to an inaccurate parameterization of the inactive material in the MC detector simulation.

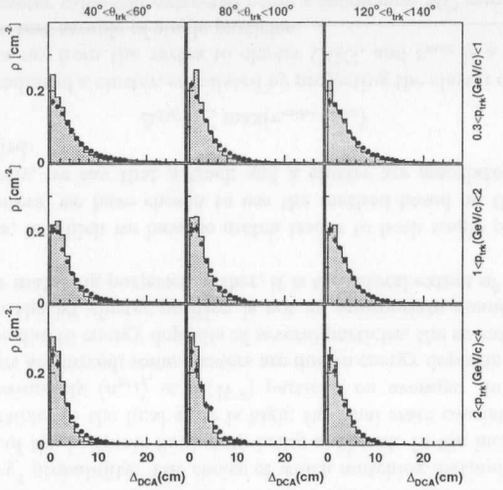

Figure 5.13: *Probability density as a function of distance of closest approach of a track to a cluster for data (dots) and single pion MC (histogram).*

5.4 Electron Identification and Reconstruction

The signature of a neutral current DIS event is the presence of a scattered electron in the final state. Thus, correct and efficient identification of the scattered electron and precise reconstruction of its position and energy are of vital importance for the analysis of DIS events. Momentum conservation requires the scattered electron to balance the transverse momentum of the hadronic system, resulting in an azimuthal back-to-back event topology. Consequently the electron is well isolated and relatively easy to find over a large part of the accessible (x,Q^2) plane. However at high y (low x), where the energy transfer from the electron to the struck quark is relatively large, the current jet goes in the rear direction and the scattered electron has a rather low energy. The resulting overlap of the hadronic component and the electron in the detector space makes it difficult to separate them and identify the latter. Furthermore, as the electron energy decreases, it becomes harder to distinguish electron from pion showers based on the pattern of energy deposits in the calorimeter.

5.4.1 Electron Finding Algorithm

In this analysis a feed-forward neural network with error back-propagation (FFBP) algorithm [109], SirA95, was used to identify electromagnetic particles based upon their showering properties in the segmented calorimeter. At the time when the SirA95 was developed, the clustering used for shower reconstruction was based on an algorithm similar to the cell island algorithm, however the objects which were clustered were calorimeter towers. These are the so-called TowerIslands [111]. The pattern of energy deposits within the TowerIsland was then translated into a set of 16 rotationally invariant moments, the so-called Zernike moments. The input to the neural network consists of the 16 Zernike moments and the total energy of the cluster. The details of the training of the neural

network algorithm are described in [110] and references therein.

The neural network output can be redefined to represent the probability that a given TowerIsland is due to an electromagnetic object. The clean electromagnetic patterns will have $P(\text{cluster}) \sim 1$, while the hadronic ones will have $P(\text{cluster}) \sim 0$. The distribution of probability is presented in figure 5.14, where the separate contributions of electromagnetic $(e^{\pm})$ and hadronic clusters $(\pi^{\pm})$ are also indicated.

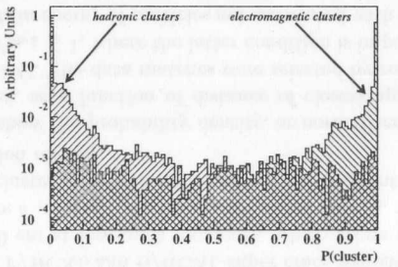

Figure 5.14: *Probability distribution for a given cluster to be an electromagnetic cluster* $P(\text{cluster})$ *using the SirA95 neural network classifier.*

From figure 5.14 it is seen that the higher the probability, the more likely it is that the cluster is due to an electromagnetic particle. Therefore, as a first step we preselect all the calorimeter clusters which have probability $P(\text{cluster}) \geq 0.9$, as possible electron candidates. In the DIS events we face the problem as to which of the electromagnetic calorimeter clusters is the *true* scattered electron. There are different physically motivated techniques to select among the preselected electron candidates the one which is most likely the *true* scattered electron. For instance we might choose the cluster with the maximum energy or highest transverse momentum. However, these introduce an a *priori* bias. Thus, an extensive study was carried out, and it was found that the best results in terms of efficiency and purity are obtained by selecting the cluster with the highest probability provided by the neural network, as the "*true*" scattered electron. In addition, candidates in the region where tracking information is available must have an associated track.

5.4.2 Electron Finding Efficiency

The performance of the electron finder can be evaluated with a sample of the preselected DIS MC events in terms of two quantities which are defined as:

$$\text{efficiency} \equiv \frac{N(e_{true}, \text{selected})}{N(e_{true})} \qquad \text{and} \qquad \text{purity} \equiv \frac{N(e_{true}, \text{selected})}{N(\text{all selected})},$$

where $N(e_{true}, \text{selected})$ is the number of correctly selected scattered electrons, $N(e_{true})$ is the total number of scattered DIS electrons which could possibly be selected, and $N(\text{all selected})$ is the total number of scattered electrons, true or not, selected by the electron finder. The efficiency and purity to identify the scattered electron are presented in figure 5.15 as a function of its energy. From the figure it is seen that an efficiency of $\approx 70\%$ at electron energies of ~ 5 GeV with purities $\gtrsim 95\%$ are achieved. It is also observed that the efficiencies and purities for electron finding increase rapidly with energy and reach $\approx 100\%$ at electron energies 15 GeV and greater.

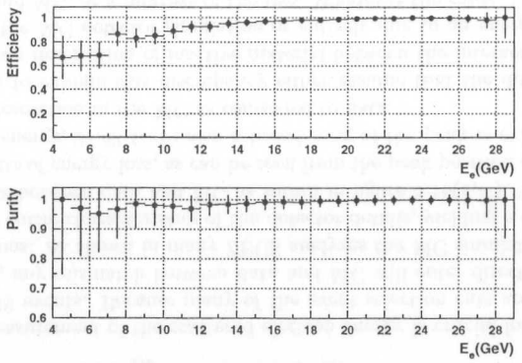

Figure 5.15: *Efficiency and purity to identify the scattered electron as a function of calorimeter measured energy.*

The fact that the scattered electron has to traverse inactive material before reaching the calorimeter results in preshowering and hence a considerable energy loss and a broadening of the electron energy deposit in the calorimeter. Thus the efficiency for identifying the DIS electron as a function of the energy profile is expected to drop, since it becomes harder to distinguish electromagnetic from hadronic showers based on the pattern of energy deposits in the calorimeter alone. Several studies indicate that the MC does not describe all characteristics of the detector simulation in full detail. In particular the distribution and composition of inactive material in the detector is simplified and seems to be incomplete in some regions close to the rear beam-hole.

For example, as seen in figure 5.16(a,a'), the distributions of the number of cells assigned to the cluster identified as the scattered electron are systematically higher in data than in the MC. This indicates that the tails of the electromagnetic showers are not well reproduced by the MC detector simulation. As a consequence one might question whether the electron finding efficiency in data is the same as in the Monte Carlo. In order to answer this question, we need to take a closer look at the neural network input parameters.

The neural network classifier, SirA95, uses as input the spatial energy deposit distribution of a TowerIsland expanded in terms of the energy weighted moments. Only terms up to a certain order are used. The higher order terms are neglected, since they may be sensitive to the tails of the energy distribution which, as we saw above, are not properly simulated in the MC. This choice of input parameters indicates that it is the energy weighted profile of the shower and not the number of cells assigned to the scattered electron which should be used for correction factor determination of electron finding efficiency between data and Monte Carlo.

In figure 5.16(b,b'), the distributions of the energy weighted radius probing the transverse spread of the shower are shown. Notice that here the agreement between data and MC is reasonable. The corresponding efficiencies and resulting correction factors derived from the usage of this variable, in the kinematic range of this analysis, were done in the way as described in [116]. All correction factors were found to be consistent with 1.0 within errors. In addition we have also studied the electron finding efficiency, in data and MC, as a function of the electron calorimeter energy using elastic QED Compton events.

This method is fully described in [115]. Using this method the correction factors were also found to be consistent with 1.0 within errors. Therefore, no extra correction factor needs to be applied to data as compared to MC in our analysis.

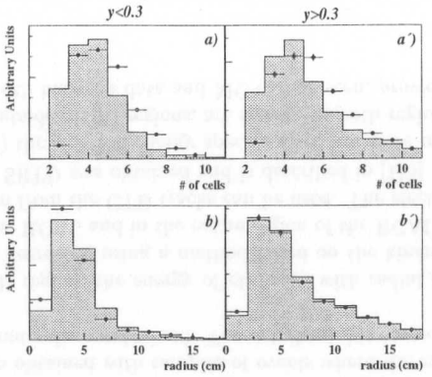

Figure 5.16: *(a,a') Normalized distributions of number of cells and (b,b') energy weighted radius associated with the cluster identified as the scattered electron, for two y ranges. The mean values for # of cells in data (dots) are systematically higher than for the MC (histogram), whereas the energy weighted radius distributions between data and MC are in reasonable agreement. For explanation see text.*

5.4.3 Electron Position Reconstruction

In addition to the event vertex, the impact point of the scattered electron in the calorimeter provides the second space point, from which the electron scattering angle is reconstructed. The calorimeter cells belonging to the electron candidate are used to determine its position. If this position lies within the acceptance of the SRTD, the position reconstruction is then further improved with SRTD information. Due to the $1/Q^4$ dependence of the cross section the events with a scattered electron in the SRTD region dominate our data sample.

I. Calorimeter Position Determination

The electron y_e and x_e coordinates are reconstructed separately. The y_e is measured from the energy leakage from the central row of cells (containing the highest energy one) and the two rows above and below it, and is based on the logarithmic weight average. The x_e coordinate is measured using the three cells of the central row only. The geometric centers of these three cells are corrected by the energy imbalance information. From these three x-positions the final x_e COG is calculated using weights proportional to $\log(E_{cell})$. All parameters for y_e and x_e COG determination were adjusted such that their values are quoted at a reference plane (FCAL: z_e=226.13 cm, RCAL: z_e=-152.13 cm). The BCAL position reconstruction is quoted at R_e = 124.0 cm. The position resolution using calorimeter information alone is $\approx$ 1 cm in x and between 0.4 and 1.2 cm in y depending on impact position. This and further details concerning the calorimeter position reconstruction are described in [112].

II. SRTD Position Determination

The position resolution of the SRTD, which has a finer granularity, is superior to that of the calorimeter. The SRTD position reconstruction has been shown to have a resolution of ~ 3 mm. When the electron calorimeter position lies within the region covered by the SRTD ($-34.0 < x_e < 32.0$ cm; $-33.3 < y_e < 32.7$ cm; $z_e = -147.25$ cm), the SRTD information is used to improve position reconstruction and resolution. Using SRTD, a reliable position reconstruction can be obtained up to 1 cm from the edge of the beam-hole. Figure 5.17 shows x_e and y_e electron position reconstruction with the SRTD in the four towers surrounding the RCAL beam-hole. A detailed overview of the SRTD hit reconstruction and electron position determination using the SRTD can be found in [113].

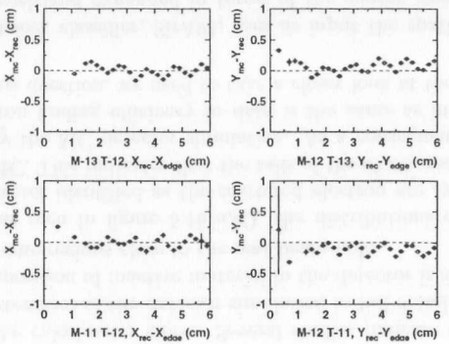

Figure 5.17: *The x_e and y_e position reconstruction with the SRTD for electrons in the four RCAL towers surrounding the beam-hole. The true extrapolated position coordinates from MC (x_{mc},y_{mc}) are compared with those reconstructed (x_{rec},y_{rec}) as a function of distance from the edge of the beam-hole (x_{edge},y_{edge}).*

5.4.4 Electron Energy Measurement

The correct measurement of the scattered electron energy is crucial for kinematic reconstruction of DIS events. Because many of the event selection cuts are based on energy (i.e. δ, E'_e,...), any mismatch between data and MC will enter directly into the acceptance calculations. As shown in many ZEUS analyzes the MC simulation does not seem to describe the entire characteristics of the detector details, yielding a discrepancy in the electron spectra between data and MC as shown in figure 5.18(a,a'). Both distributions show clear effects of energy loss, as can be seen from the peak position deviating from the electron beam energy, 27.52 GeV; also a broadening of the peak is evident, indicating a better energy resolution in the MC as compared to data.

The models to explain this discrepancy either assume that the difference is entirely due to inaccurate description of inactive material between the interaction point and the calorimeter in the MC detector simulation or entirely due to an energy scale mismatch between data and MC, or a mixture of the two. Whatever the cause, these effects should be corrected for. This can be done independently in data and MC by using specially

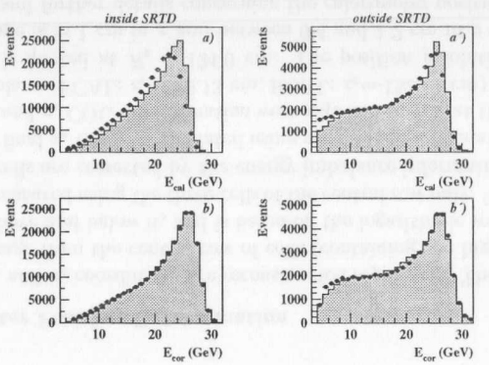

Figure 5.18: *(a,a') uncorrected and (b,b') corrected electron energy spectra for data (dots) and MC (histogram). The uncorrected electron energy spectrum in the data peaks at a lower values and is broader as compared to the MC, indicating that the energy loss and resolution is not completely simulated in the MC. The agreement after correction between data and MC is good. For details see text.*

selected kinematically constrained events. For events at low y, the electron energy is kinematically expected to peak at the nominal beam energy of 27.52 GeV, the so-called kinematic peak (KP) events. The elastic QED Compton process leads to events in which the electron and photon energies add up to the nominal electron beam energy. The other reaction which is used is the exclusive production of ρ^0 in the deep inelastic regime.

In the SRTD region a method based on presampler techniques can be used, to correct the electron energy loss in inactive material. The signal within the SRTD will be proportional to the number of particles in the shower, which in turn is related to the degree of preshowering. Thus using the measured energy in the CAL and the signal from the SRTD it is possible to correct for the amount of energy which has been lost. The energy correction was obtained with samples of events where the energy of the scattered electron can be kinematically constrained. The details of this correction method are fully described in [114].

Outside the SRTD region, the energy of electrons with radial distance up to 70 cm in the RCAL can be corrected using a method based on the kinematic peak events. In the outer region of the RCAL and in the entire region of the BCAL an energy correction based on a calibration from the CTD tracks can be used. The electron energy correction in the region outside SRTD was obtained and is described in [115].

In figure 5.18(b,b') the electron energy spectra after the afore mentioned corrections, for both inside and outside SRTD regions, are shown. In both regions good agreement in peak position and width between data and MC can be seen, providing confidence in the applied corrections.

5.4.5 Electron Cluster Splitting

In the kinematic domain of low-Q^2 and low-x both the current jet and the DIS electron scatter into the RCAL with similar energies. Often, in this domain, the TowerIsland cluster algorithm is not able to separate the energy deposits of the electron from those

which belong to particles of the current jet. Thus the electron is not isolated, and energy deposits in the calorimeter which belong to the current jet get associated to the electron cluster. In this case the reconstruction of the kinematic variables is biased. Furthermore, this situation may lead to incorrect electron energy correction procedure, since corrections were tuned on events for which scattered electrons were well isolated.

The difference, E_h, between the measured energy of the scattered electron cluster (E_{CAL}^{meas}) and the corresponding true electron[3] energy in the detector (E_{CAL}^{true}) is a measure of how much additional energy from the current jet has been included into the electron cluster, i.e.

$$E_h = E_{CAL}^{meas} - E_{CAL}^{true} .$$

For non-isolated electrons E_h is positive and is expect to increase as x decreases. In figure 5.19 the amount of hadronic energy, E_h, is presented for different W and Q^2 intervals. It is seen, that as W increases ($W^2 \approx Q^2/x$) the amount of hadronic energy in the electron cluster increases, as expected. It is also seen that as Q^2 increases E_h decreases. This is because as Q^2 increase, the p_t of the hadronic final state increase as well, i.e. $Q^2 \propto p_T^2$ at fixed W.

The amount of hadronic energy which is attributed to the electron cluster depends on the clustering algorithm. The TowerIslands which do not use the full granularity of the calorimeter can be split into smaller objects, such as cell islands. This is done by reclustering the cells belonging to the TowerIsland using the cellIsland algorithm, see section 5.2.1. The energy and cells belonging to the scattered electron are now taken to be the energy and cells of the highest energy cell island. The distribution of E_h measured relative to the cell island is also shown in figure 5.19. It is seen that the amount of hadronic energy remaining in the cellIsland associated with the scattered electron is reduced. We have checked the effect of this procedure by looking at the purities in the bins of the selected final sample. It was found that purities increase by up to 5% for high W and low Q^2 bins.

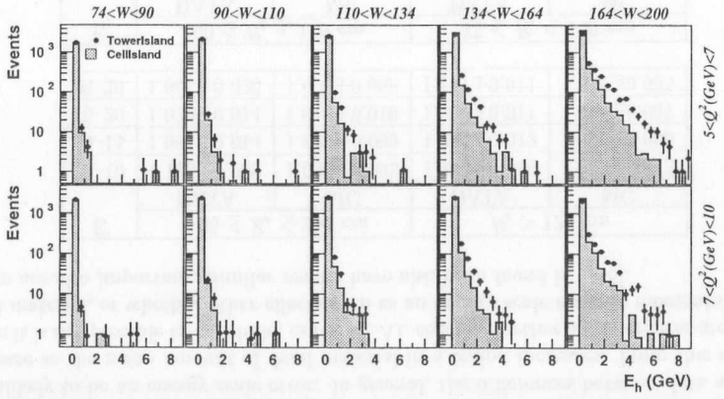

Figure 5.19: *The amount of hadronic energy (E_h) associated with the TowerIsland and cellIsland cluster of the identified scattered electron. For explanation see text.*

[3]Here by electron we mean both electron and the final state radiated γ_{fsr}.

5.5 Calorimeter Energy Scale

The calorimeter energy scale can be studied by using a sample of isolated calorimeter clusters with a matching track. Using this method we can compare data with data and MC with MC in a completely unbiased way. If the corrections for MC and data are the same, this will give an indication that the amount of dead material present in the detector is adequately described and simulated in the MC. If the corrections are not the same and are energy dependent then this will be an indication of inadequate description of dead material in the MC simulation. The scale problem will show itself by a constant offset in all measured energy bins.

The complete details of this analysis, for identified scattered electron, are described in [117]. Here we will only briefly mention the method used and the conclusions reached as the result of this study.

Let us denote by S the correction factor applied to the calorimeter energy, E, which is needed in order to make it equal to the track momentum, p_{tr}. In order to determine S we study the distribution of the normalized residual, which we define by the variable f:

$$f = 2(S \cdot E - p_{tr})/(S \cdot E + p_{tr})$$

and tune S so that f is centered around zero. f is the measure of the fractional error if ΔE is small. The justification for this formula comes from the fact that while for different absorber thickness the mean value of the electron energy spectra are significantly shifted towards lower values, the distribution remains approximately Gaussian.

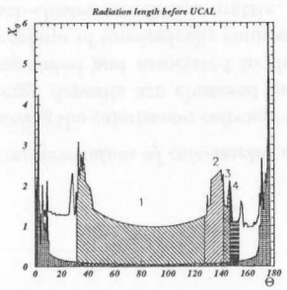

Figure 5.20: *Radiation length in front of the calorimeter as seen from the nominal interaction point. The squared shaded area is the amount of radiation length for $R \leq 20$ cm. The other hashed areas correspond to the 4 regions which we have investigated, see text.*

The selected sample (see [117]) was subdivided into 4 distinct regions, as shown in figure 5.20. The regions were chosen such that the average amount of dead material traversed by the electron was approximately constant. The S factors for the 4 different regions and 4 energy bins are listed in Table 5.1. The S factors are correlated with the amount of dead material and energy; larger S factors are found in regions with more dead material and at lower energies, as expected.

The S factors determined in the MC are consistent with the amount of dead material put into the simulation. However, the determined S factors show a statistically significant difference between data and MC in all the 4 regions. Specifically, in the BCAL the S factors in the data are a factor 1.06 larger than those in the MC in all energy bins,

indicating the possible presence of an energy scale problem. For the RCAL, the ratios of data/MC S factors in a given region are also roughly energy independent.

However, these ratios depend very much on the region, such that the bulk of the effect is unlikely to be an energy scale error. In general, the differences between data and MC increase as the mean amount of dead material in a region increases. From this analysis alone it is not possible to conclude, in the RCAL region, whether all differences are due to dead material, or whether other effects such as an energy scale error or momentum scale errors are also important. Similar results have also been found in [118].

E	$-95 \leq Z_e \leq 200$ cm		$R_e > 120$ cm	
	DATA	MC	DATA	MC
5–10	1.105±0.009	1.036±0.009	1.243±0.016	1.143±0.013
10–15	1.081±0.014	1.020±0.009	1.201±0.012	1.099±0.006
15–20	1.079±0.014	1.014±0.010	1.200±0.011	1.095±0.007
20–30	1.068±0.026	1.006±0.008	1.167±0.011	1.049±0.005

E	$100 \leq R_e \leq 120$ cm		$75 \leq R_e \leq 100$ cm	
	DATA	MC	DATA	MC
5–10	1.172±0.027	1.078±0.012	1.069±0.017	1.032±0.009
10–15	1.154±0.034	1.054±0.008	1.063±0.011	1.016±0.007
15–20	1.121±0.021	1.047±0.008	1.032±0.013	1.008±0.010
20–30	1.066±0.016	1.000±0.009	1.004±0.015	0.981±0.008

Table 5.1: S factors for BCAL and RCAL electrons.

In similar studies, of isolated charged hadrons in the BCAL region, a comparable discrepancy between data and MC, of 8.5±2.0%, was found [119]. In another study [115], based on the requirement of the transverse momentum balance between the electron and hadronic final state, discrepancy of ∼4–6% in the BCAL and ∼1–3% in the RCAL was found between data and MC.

As a result of all these studies, the energy scale in the BCAL and RCAL have been corrected (lowered) by 6% and 3% respectively in the MC reconstruction of the energy deposits. This is done in order to make the MC simulation consistent with the real data taken with the ZEUS calorimeter. From these studies the uncertainty on the energy scale correction is estimated to be ∼ 3%.

5.6 The Hadronic Energy Flow Algorithm

In this section the *hadronic energy flow algorithm* to reconstruct the four momenta of all the particles in the event is presented, based on a global approach to the calorimeter and tracking information. The basic concept is to use tracking information instead of calorimeter information wherever the former provides better energy resolution. The remainder will consist of calorimeter energy clusters corresponding to neutral particles or jet of particles. In this approach low energy charged particles which do not reach the calorimeter are naturally included. A schematic representation of calorimeter and tracking information and their relation are shown figure 5.21.

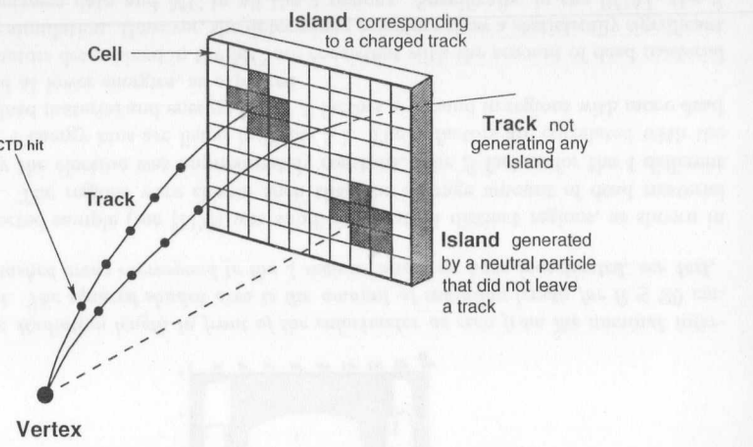

Figure 5.21: *Schematic representation of calorimeter and tracking information.*

In the first step, after removing the calorimeter cells and track assigned to the scattered electron, the calorimeter energy deposits are clustered into cone islands. In the next step charged tracks are extrapolated and associated to these calorimeter objects. The outcome of this operation are groups of topologically connected tracks and clusters. These groups form the so-called track-cluster association matrix. The matrix is then processed according to the following rules:

1. Charged tracks not associated to any calorimeter object are counted as pions;
2. Calorimeter objects not associated to any track are counted as neutral energy in such a way that $E^2 = p^2$;
3. Calorimeter objects associated with more than 3 tracks, the so-called "jet" clusters, are counted as one jet in such a way that $E^2 = p^2$.[4]

For all other track-cluster combinations an additional group of rules is required, since a decision whether to take a track or a cluster has to be made. This group of rules is discussed below.

The decision to take a track instead of a calorimeter object (to make a match) is based on two requirements. The first requirement is that the energy deposit to which the track is associated is due to the associated track alone. The second requirement is that the momentum resolution of the track is better than the energy resolution of the associated calorimeter object.

To make these arguments quantitative we have studied the E_{isl}/p_{trk} ratio in the single pion MC sample. Figure 5.22 shows the average value of ratio versus the polar angle of the track. It is seen that the ratio is about 0.9 in all calorimeter regions except in the calorimeter crack regions where it is lower, about 0.8. This ratio is associated with an error which has to be taken into account when making a match.

[4]Note, that jets of particles are usually energetic enough so that the assumption that they are massless does not affect the final result.

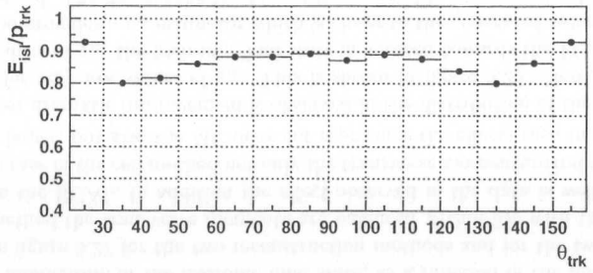

Figure 5.22: *Average values of E_{isl}/p_{trk} ratio as function of track angle, θ_{trk}.*

The track momentum resolution has been measured to be $\sigma_{p_t}/p_t = 0.005\,p_t \oplus 0.016$, where p_t is the transverse momentum in the laboratory frame measured in GeV. The calorimeter energy resolution under ideal test conditions was measured to be $\sigma/E = 18\%/\sqrt{(E)}$ for electromagnetic and $\sigma/E = 35\%/\sqrt{(E)}$ for hadronic particles. In the experimental setup the presence of inactive material in front of the calorimeter as well as non-uniformity decrease the resolution. The resolution parameters were increased [120] to 25% if $E^{Isl}_{emc}/E^{Isl}_{tot} > 0.9$, and 40% otherwise, where E^{Isl}_{emc} is the energy on an island in the EMC section. The comparison of track momentum resolution and calorimeter energy resolution for electromagnetic and hadronic particles is show in figure 5.23. The tracking resolution is much better at low particle energies and becomes comparable to the electromagnetic(hadronic) calorimeter resolutions around $p_t \sim 13(18)$ GeV.

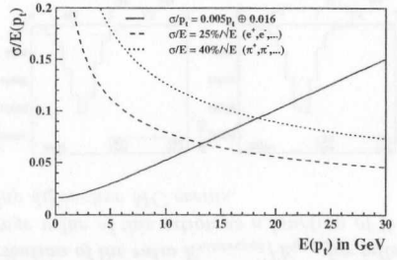

Figure 5.23: *Calorimeter and track resolution.*

Therefore, the requirements to replace the calorimeter object by a track or set of tracks are:

1. $E_{ils}/p_{trk} < 0.9 + \Delta(E_{isl}/p_{trk})$
2. $\Delta p_{trk}/p_{trk} < \Delta E_{isl}/E_{isl}$

The first requirement ensures that no energy associated to a neutral particle is rejected. The second requirement improves the energy resolution. The distribution of the E_{isl}/p_{trk} values for all track-cluster matches based on $\Delta_{DCA} \leq 20$ cm for the single pion MC are shown in figure 5.24 (dots). The same ratio for all those track-cluster matches that satisfy the above requirements are also shown (histogram). These additional requirements lead to a small loss of true track-cluster matches.

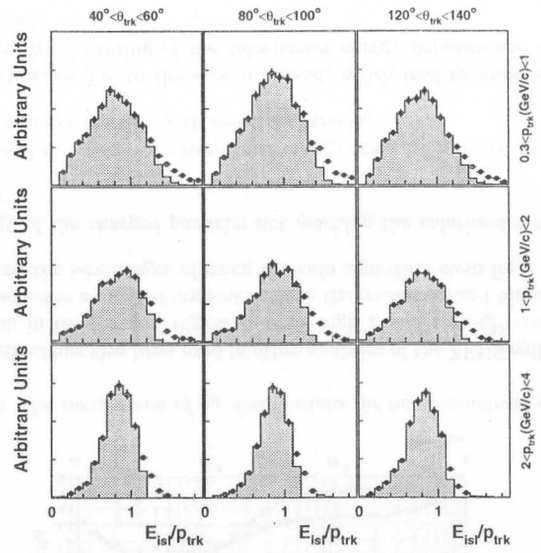

Figure 5.24: *E_{isl}/p_{trk} ratio for different track angles, θ_{trk}, and momenta, p_{trk}, as denoted in the figure.*

The output of the energy flow algorithm is a set of *energy flow objects* (or "particles") characterized by their energy and momenta. The energy flow objects (EFOs) are also know as Zeus Unidentified Flow Objects or *zufos*.

5.6.1 Test of the Energy Flow Algorithm

To assess the merits of using zufos in the determination of kinematic variables we have used samples of selected diffractive and DIS MC events. In the selection we required the presence of the reconstructed scattered electron, and, as in the final analysis, we limited ourselves to the kinematic range defined by $7 < Q^2 < 140$ GeV^2 and $60 < W < 200$ GeV.

For the diffractive events in which the products of photon dissociation are well-contained in the calorimeter, we have compared the total energy measured to that expected from the generated particles. The results of this comparison are shown in figure 5.25. While in the cell method the measured energy is only 72% of that generated, with zufos it is 90%. From studies of particle production at the generated level we know that on average 1% of the energy is carried away by neutrinos, 1-2% is lost due to noise cuts, and a further 2-3% is lost due to the spiraling charged particles. The estimate for the energy lost in the inactive material in front of the calorimeter is 24%. About 70% of this energy is recuperated by using zufos. The improvement in the energy measurement is present for all energies. The same improvement is observed in the reconstruction of the invariant hadronic mass, as seen in figure 5.26. This illustrates that by using the zufo algorithm, the effect of energy loss due to the inactive material is substantially reduced.

For the inclusive DIS events we have compared the transverse momentum balance between the scattered electron and the hadronic final state for the zufo and cell methods in

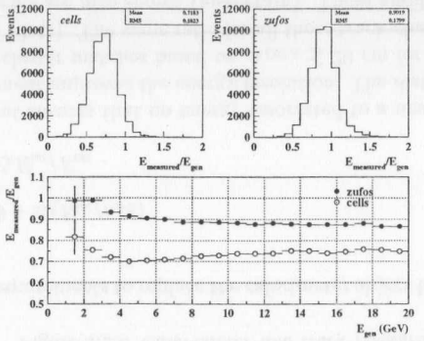

Figure 5.25: *The distribution of the ratio $E_{measured}/E_{gen}$ for cells and zufos reconstruction methods, and the average value of this ration as a function of the generated energy, E_{gen}, for a sample of RapGap diffractive MC events.*

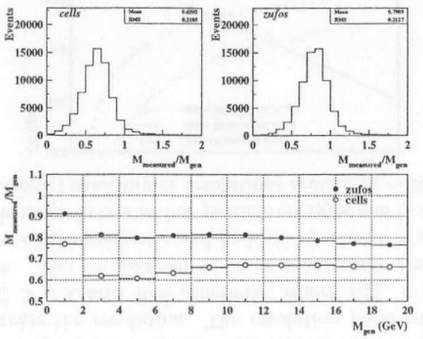

Figure 5.26: *The distribution of the ratio of $M_{measured}/M_{gen}$ for cells and zufos reconstruction methods, and the average value of this ratio as a function of the generated mass, M_{gen}, for a sample of RapGap diffractive MC events.*

the data and MC samples. The ratio $\langle \delta_{P_t} \rangle = P_t^{had}/P_t^e$, where P_t^e is the transverse momentum of the scattered electron in the laboratory system and the P_t^{had} is the corresponding transverse momentum of the hadronic final state, as a function of the hadronic angle γ_h is shown in figure 5.27 for the two reconstruction methods and for the two samples. For the zufo method the transverse momenta are balanced within 5% with the largest effect observed in the BCAL. In addition the effect observed in the data is well reproduced in the MC. In case of the cell method not only the transverse momentum imbalance is almost four times larger, but also the MC does not reproduce the effects seen in data.

The most dramatic improvement is observed in the distribution of the y_{jb} variable, in particular for very low values of y_{jb}. This is shown in figure 5.28. Note, that in events with low values of y_{jb}, the hadronic final state is boosted towards the FCAL region. The zufo method provides a y_{jb} estimator which is closer to the generated value of y than does the cell method. The decrease in the bias of the y variable is mainly due to the method of clustering and position reconstruction. The improved agreement between the distribution

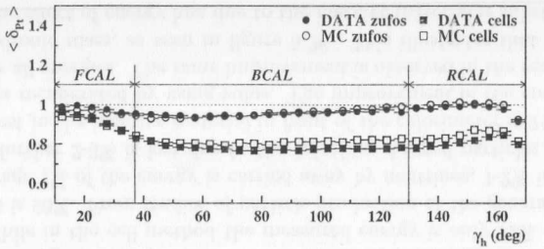

Figure 5.27: *The ratio of $\langle \delta_{P_t} \rangle = P_t^{had}/P_t^e$ as a function of hadronic angle γ_h for two reconstruction methods and the data and MC samples as denoted in the figure. For clarity the correspondence between γ_h and the calorimeter sections are also shown.*

of y_{jb} in the data and the MC with the zufo method, also shown in the figure, will lead to a smaller systematic error in the measurement of the cross sections at low y.

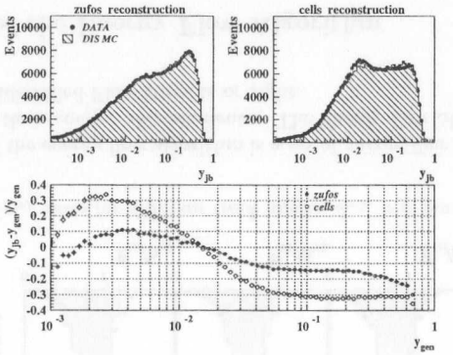

Figure 5.28: *The comparison of y_{jb} distributions for two reconstruction methods.*

The zufo method has also been used in other analyses of the ZEUS collaboration, such as jet production in the forward region and the high x and high Q^2 cross section measurements; in each case a marked improvement in the resolution and biases was observed.

To summarize, the advantages of using the zufo algorithm stem from the following:

- The energy of the charged particles not reaching the calorimeter active volume is recovered;
- The effects of the inactive material and energy scale are reduced by replacing some of the calorimeter clusters with associated tracks;
- The uncertainties due to the shower spread, which lead to granularity effects are reduced by the clustering of the calorimeter energy deposits and cluster position reconstruction.

Chapter 6

Selection of the DIS Event Sample

In chapter 4 the event preselection for the NC DIS candidates with the three-level trigger system and a physics filter was described. In total 971,168 NC DIS candidates remained after the preselection requirements and were reconstructed as described in the previous chapter. The sample selected up to this point still contained backgrounds due to loose cuts applied at the preselection stage. In addition, due to fiducial effects, part of the preselected sample exhibits large migrations in the kinematic phase space. In order to enhance the purity of the sample of DIS events and to increase the precision of the reconstruction of kinematic variables, further selection cuts are necessary. In this chapter the steps leading to the final sample are discussed, and the characteristics of the sample are presented.

6.1 Trigger Condition

The DIS trigger definitions at the FLT level changed during the '94 running period. The RCAL-IsoE trigger was put in coincidence with the REMCth trigger after collecting $\sim$ 30% of the luminosity. The REMC trigger threshold also changed from 2.0 GeV in the early runs to 3.4 GeV. Therefore, to analyze the whole data sample with a uniform trigger condition, we have imposed the tightest trigger condition used during the '94 data taking period, the so called *STANDARD_18OCT94* trigger. The same trigger condition was also imposed on all MC samples. The trigger efficiencies in the data and the MC were found to agree within 0.5%, for all three triggers.

In addition for almost 60% of the luminosity used in the present analysis the RCAL-IsoE trigger was not working in one of the trigger towers around the RCAL beam hole, due to a dead Trigger Encoder Card (TEC). To take this into account the TEC effect was simulated in the MC. The events are then weighted for the fraction of the luminosity in which the problem existed. As a systematic check, instead of using the MC simulation, we made a cut to exclude this region, $-33.5\text{cm} < x_e < -8.5\text{cm}$ and $-32.5\text{cm} < y_e < -7.5\text{cm}$.

6.2 Timing Cuts

At the preselection stage a large fraction of the beam-gas (p-gas, e-gas) background was removed by a cut on the average CAL section times (t_{FCAL}, t_{RCAL}) and on their differences. However, offline analyses indicated [121] that a small fraction of this background still remained in the selected sample. Therefore, a more refined timing cut was imposed;

we required the timing cuts at the final selection stage to be

$$|t_{FCAL} - t_{RCAL}| < 6\,\text{ns}, \quad |t_{FCAL}| < 6\,\text{ns}, \quad \text{and} \quad |t_{RCAL}| < 6\,\text{ns}, \tag{6.1}$$

in order to further reduce the beam-gas background. This will be referred to as the *timing cut* in the following. The timing cut was applied only to data events since no reliable calorimeter timing information is available in the MC event simulation.

6.3 Box Cut

It is important to ensure an accurate reconstruction of the electron impact position and measurement of its energy, since both of these quantities enter into the calculation of kinematic variables on which some selection cuts are based. In the region close to the beam-pipe, the reconstruction of the electron impact position and energy is poor, due to energy leakage into the beam-hole. In figure 6.1 the effect of energy loss for electrons from the kinematic peak is shown as a function of distance from the edge of the beam-hole, for towers to the right of and below the RCAL beam-hole.

While the expected value of the energy is 27.52 GeV, the measured value tends to be lower when the electron impact position is within 3 cm of the edge. The effect is particularly marked in the y direction. The effect in the other towers around the beam-hole is essentially identical. As suggested by these results the electron impact position was required to be at least 3 cm away from the beam-hole edge.

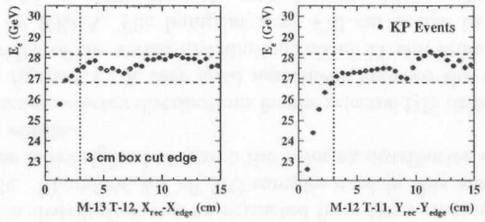

Figure 6.1: *The average measured electron energy for electrons at the kinematic peak, KP, as a function of the distance of the electron position to the edge of the RCAL beam-hole, shown for the towers right of (M-13, T-12) and below (M-12, T-11) the RCAL beam-pipe. The horizontal dashed lines represent a $\pm 5\%$ deviation from the expected electron beam energy. The dotted line indicates a 3 cm edge cut for fiducial requirements.*

Furthermore, the electron finding efficiency drops when the electron impact position is near the crack region between the two RCAL calorimeter halves. Electrons entering in to the crack region deposit a substantial amount of energy in the RCAL HAC section, and are misidentified. The crack between the two calorimeter halves affects also the performance of the SRTD, which by design is attached to the face of the calorimeter. Therefore, we require that the electron impact position be at least 2 cm away from the calorimeter/SRTD crack.

For almost all '94 runs considered in this analysis, one of the two PMTs in one EMC cell of the RCAL was not functioning. In such a case, the deposited energy is estimated by doubling the signal in the functioning PMT. However the position reconstruction is

worsened. A better solution is to cut away events with the the electron impact position between 7cm $< x_e <$ 31cm and $-32\text{cm} < y_e < -18\text{cm}$.

Figure 6.2 shows the acceptance of the SRTD with the imposed cuts as well as the faulty trigger tower and EMC cell.

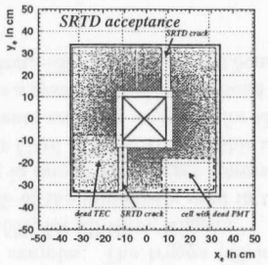

Figure 6.2: *Scatter plot of the electron impact position in the SRTD. The two 'L'-shaped regions indicate the nominal acceptance for the two SRTD halves. The cells affected by the dead trigger tower and the cell with the dead PMT are indicated in the figure.*

6.4 Electron Energy Cut

At large y, where the current jet goes into the direction of the rear calorimeter, low energetic particles ($\lesssim$ 5 GeV) might fake the pattern of energy deposits typical for the scattered electron. Hence, the probability to misidentify the DIS electron increases at high y. The electron finding efficiency decreases from greater than 90% at electron energies of 10 GeV to about 60% at electron energies of about 5 GeV.

To avoid electron misidentification (i.e. control the photoproduction background) and to have reliable electron finding, the scattered electron energy was required to be,

$$E'_e > 10 \text{ GeV},$$

where E'_e is the corrected energy of the scattered electron. This cut will be referred to as the *electron energy* cut in the following.

6.5 Vertex Cut

For the calculation of angles and the kinematic variables which require angular information, it is important that the vertex location be known. In the '94 data sample the resolution of the z-vertex position was found to be about $\sigma_{z_{vtx}} \simeq 2.3$ mm in the rear and central regions and to decrease to more than 3 mm towards the forward region. The vertex finding efficiency depends on the true interaction point as well as on the properties of the hadronic final state. As the interaction point moves towards the RCAL, the efficiency for finding a vertex increases. This is due to the increased acceptance in the CTD of charged particles from the proton remnant. However, the event acceptance decreases because electrons, scattered through a small angle, are less likely to be detected in the rear calorimeter. This is illustrated in figure 6.3 where the change in acceptance as function of Q^2 is shown by comparing the samples for two different vertex distributions (also shown).

Due to this effect the measured distribution in the DIS sample is distorted compared to the original. Since the acceptance is based on the MC simulation, it is the initial vertex distribution which is needed for the MC simulation.

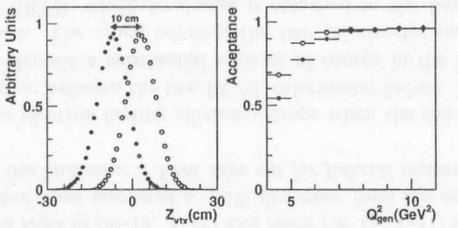

Figure 6.3: *The z_{vtx} vertex distribution for two MC samples and the corresponding acceptance as a function of Q^2.*

The real vertex distribution can be extracted from the minimum bias photoproduction event sample. Therefore, for all MC samples used in this analysis, the generated vertex distribution is reweighted to match the z-vertex distribution of the minimum bias photoproduction events.

The reconstructed z-vertex distributions for the selected DIS data and the MC sample are compared in figure 6.4. A very good agreement between the data and the MC is observed. The width of the vertex distribution, about 11 cm, reflects the proton bunch length provided by HERA. The bump at $z \approx +70$ cm is due to the satellite proton bunches, arriving 4.8 ns earlier than the main bunches, and created by the HERA 208 MHz feedback system. Events reconstructed without a tracking vertex are assigned to the nominal vertex position at $z_{vtx} \equiv +3$ cm which accounts for the spike. The resolution of the x- and y-vertex position is about 1 mm and is larger than the transverse proton beam spread of about 50 μm. Therefore, we always set the x- and y-vertex position to the mean values corresponding to the minimum bias sample distributions: 0.12 cm in x and -0.13 in y.

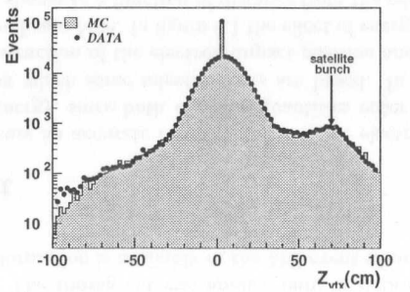

Figure 6.4: *z-vertex distribution for the selected DIS candidates and the DIS MC sample. Events without a tracking vertex are set to $z_{vtx} \equiv +3$ cm, which accounts for the spike.*

A small disagreement between data and MC can be seen in the upstream region, $z \lesssim -70$ cm, where data has more events than the MC. This is presumably due to the presence of the residual beam-gas background in the data sample. In order to reject this background and to reduce any acceptance uncertainties, a vertex cut of -50 cm $\leq$

$z_{vtx} \leq 100$ cm, was applied. We also applied a vertex cut, -28 cm $\leq z_{vtx} \leq 40$ cm, to investigate acceptance effects and to check for any influence of the satellite contribution, as a systematic check.

6.6 The y_{el} Cut

In photoproduction events, isolated electromagnetic calorimeter clusters in the FCAL tend to be misidentified as the scattered electron. Most of these events are characterized by a large y-value as reconstructed from the electron method. The requirement of a minimum energy of 10 GeV limits the maximum value of y_{el} and therefore by imposing the cut,

$$y_{el} < 0.95,$$

these background events are removed.

6.7 δ-cut

Most of the background events are rejected at preselection stage (see chapter 4) by requiring either an electron to be identified in the final state or by applying of the energy-momentum conservation cut (δ-cut). Figure 6.5 shows the comparison of the δ distributions, after the preselection cuts, for the data and the DIS MC. At low(high) $\delta < 40$ GeV (> 70 GeV) values there is a disagreement between data and MC. The disagreement at low values of δ is due to the remaining presence of the high W photoproduction events, for which δ tends to be high. The discrepancy at high δ is due to the remaining contribution of p-gas events. To reject these backgrounds further, stricter cuts on δ values was applied,

$$40\text{GeV} < \delta < 70\text{GeV},$$

and will be referred to as the *δ-cut* in the following. An added advantage is that this cut also removes events with a large energy initial state radiation photon.

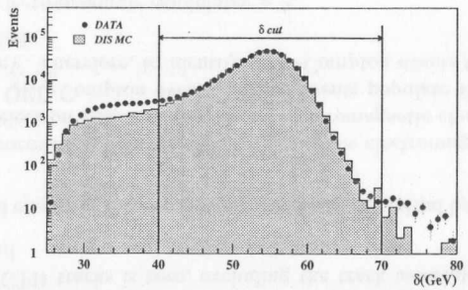

Figure 6.5: *Comparison of the δ distributions after the preselection cuts for the data and the DIS MC. The vertical lines show the range selected for this analysis. The MC sample was normalized to the number of events in data between δ values of 50 and 60 GeV.*

6.8 The y_{jb} Cut

In events where both the hadronic transverse momentum and y_{jb} are small, calorimeter noise, albedos and resolution effects can have significant impact on the reconstruction of the hadronic angle, γ_h. The average values of the residuals, $(\gamma_h - \gamma_{true})/\gamma_{true}$, as a function of y_{jb} are shown in figure 6.6. The error bars represent the RMS of the corresponding distributions. At low y_{jb} a bias in the reconstruction of γ_h is observed, which disappears at larger values of y_{jb}. A marked improvement in the resolution with increasing y_{jb} is also observed. To improve the accuracy of the DA kinematic variables reconstruction, we require,

$$y_{jb} > 0.02 .$$

This cut, referred to as the *y_{jb}-cut* in the following, is applied to both data and MC.

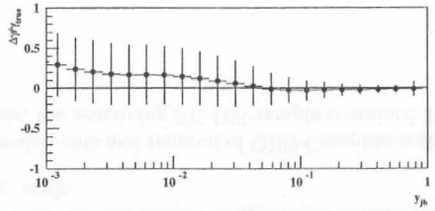

Figure 6.6: *The average values of $\Delta\gamma/\gamma_{true}$, where $\Delta\gamma = (\gamma_h - \gamma_{true})$, as a function of y_{jb}. The error bars represent the RMS of the corresponding distributions.*

6.9 Cosmic and Halo Muons Rejection

Muons as products of interactions in the upper atmosphere penetrate the ZEUS detector almost vertically and deposit very little energy in the calorimeter. However, in some cases the muon interacts in the calorimeter and produces a shower, which mimics a scattered electron. These cosmic events are characterized by a large EMC energy deposit, while the number of active cells and hence the total calorimeter energy are very small. Usually only two tracks are reconstructed in the CTD.

Another source of background are the beam-associated halo muons. They leave characteristic signals in FCAL and RCAL or hits in several adjacent cells in the BCAL, that line up and can be matched to hits in the muon chambers.

Most of the muon background events are rejected at the trigger level. However, the rates of these events are very high, and a small fraction passes all the preselection cuts. Only dedicated topological algorithms which are too time consuming to be applied at the trigger level can reject these events. Those are applied in the offline analysis.

6.10 QED-Comptons Rejection

Elastic QED-Compton events, $ep \rightarrow ep\gamma$, which are not simulated in the MC, are another source of background and can be efficiently removed on an event by event basis. These events are characterized by,

- 2 identified electromagnetic clusters in the calorimeter,
- the entire energy within the calorimeter is contained in these two clusters,
- number of CTD tracks is zero, excluding the track associated with the scattered electron, and
- the summed energy of the two clusters is close to the initial beam energy $E_e = 27.52$ GeV.

In figure 6.7 the correlation between the energies of the electromagnetic cluster identified as the scattered electron (E_e) and the second electromagnetic cluster (E_γ) is shown for a MC sample of QED-Compton events. These events populate the region of (E_e+E_γ) between 20-35 GeV. Therefore, to identify QED-Compton events the following selection algorithm is applied:

1. number of electromagnetic candidates = 2,
2. back-to-back in azimuthal angle,
3. number of tracks = 0, excluding the scattered electron track,
4. $E_{CAL} - E_\gamma - E_e \leq 0.4$ GeV, E_{CAL} is the total energy in the CAL,

In figure 6.7 the correlation between E_e and E_γ is shown for data events. The data follow the pattern expected from the MC, indicating a substantial contribution of QED-Compton events.

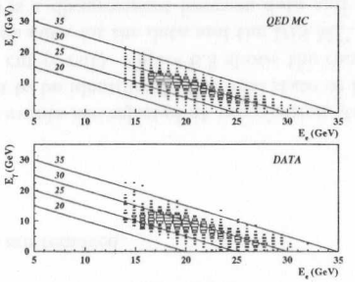

Figure 6.7: *The correlation between the energies of the electromagnetic cluster identified as the scattered electron (E_e) and the second electromagnetic cluster (E_γ) for QED-Compton MC events, without applying any cuts. The same correlation is shown for data events, after applying selection cuts (see text).*

The efficiency for rejecting QED-Compton events, with the above algorithm, was checked with QED-Compton MC and was found to be greater than 98%. We also checked the effect of the rejection algorithm on the diffractive MC sample and we found that less than 0.5% of diffractive events are rejected by this algorithm. As a systematic check, instead of removing the events from the data, we have subtracted statistically from the final event sample the cross section normalized QED-Compton events. We found no significant differences in the extracted diffractive cross section, using the rejection algorithm or statistical subtraction procedure. Therefore, the events passing the above selection algorithm were identified and removed from the sample.

6.11 Summary of the Final Sample Selection

In this chapter the selection of events in order to reach the final NC DIS sample was presented. In general, the preselection cuts were tightened, and new cuts were added to increase the purity of the sample and to limit the correction factors that will be used later to extract the diffractive cross section. To summarize, the following criteria were applied to select final sample NC DIS events:

- Box cut Events with a scattered electron impact point in the RCAL inside a box of 26 cm × 26 cm around the beam-pipe are rejected. This ensured that the impact point was at least 3 cm away from the edge of the RCAL and therefore guaranteed full containment of the electromagnetic shower in the calorimeter;
- Electron energy cut $E'_e > 10$ GeV, where E'_e is the corrected energy of the scattered electron. This cut ensured high and well understood electron finding efficiency and suppresses background from photoproduction;
- Vertex cut -50 cm $< z_{vtx} <$ 100 cm. This cut was performed for events with a reconstructed tracking vertex and suppresses beam-gas background events;
- y_e cut $y_e < 0.95$. This condition removed events where fake electrons were found in the FCAL;
- δ cut 40 GeV $< \delta <$ 70 GeV. This cut removed events with large initial state radiation and further reduced the background from photoproduction;
- y_{jb} cut $y_{jb} > 0.02$. For the Double-Angle method, this ensured a reliable measurement of the γ_h angle.

After the above selection cuts and removal of QED-Compton scattering events and residual cosmic ray events, the remaining NC DIS sample contained 316,091 events.

Chapter 7

Extraction of the Diffractive Sample

In this chapter, we first discuss possible methods of selecting diffractive sample with the ZEUS detector. A description of the method chosen in this analysis is than given in detail in section 7.1.3.

The aim of this analysis is to measure the cross section for diffractive production of mass M_X as a function of W and Q^2. The resolution and binning in W and Q^2 variables are described in section 7.2, followed by a discussion of the mass determination in section 7.2.1.

The reliability of extracting the diffractive contribution has been tested on a controlled MC sample and the results are presented in section 7.3.

Finally, the unfolding procedure and the radiative corrections needed to determine the Born cross section from the measured number of events in the bins are discussed in section 7.4 and section 7.5, respectively.

7.1 Extraction Methods

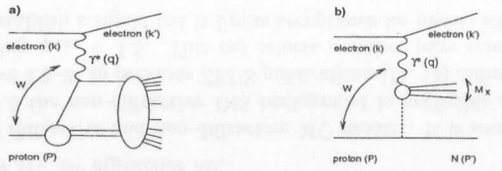

Figure 7.1: *a) Schematic diagram describing particle production in deep inelastic electron proton scattering. b) Schematic diagram describing particle production by diffractive dissociation in a deep inelastic ep interaction.*

The dominant mechanism of Deep Inelastic Scattering in which the color transfer between the struck quark and the proton remnant is responsible for populating the rapidity interval between them with hadrons is shown schematically in figure 7.1a. The experimental signature of a Pomeron exchange (color singlet exchange) would consist of a quasi-elastically scattered proton, well separated in rapidity from the remaining hadronic system as illustrated in figure 7.1b.

Thus, by *diffractive* Deep Inelastic Scattering, we mean a process of the type,

$$e + p \to e' + X + p',$$

where X denotes the final state corresponding to the photon dissociation and p' denotes the final state scattered proton well *separated* in rapidity space from the state X. By "well separated" we mean, following J.D. Bjorken, that the rapidity gap between X and p' is *non-exponentially suppressed.*

7.1.1 Selecting Events with Leading Proton Spectrometer

In diffractive scattering the momentum transfer squared t is expected to be small ($|t| \lesssim 1$ GeV^2) and the scattered proton escapes through the beam pipe without being detected in the central detector. These events can be selected by using the ZEUS leading proton spectrometer (LPS) which detects the scattered proton at small angles (up to 1 mrad) with respect to the incoming proton beam, and measures its momentum, as well. The uncorrected $x_L = p'_z/p_z$ spectrum measured in the LPS for the DIS events is shown in figure 7.2. A prominent peak at $x_L \simeq 1$ is observed. The diffractive candidate events are selected by demanding that the scattered proton carry a fraction of the incident proton beam momentum, x_L, greater than 0.97. With this selection a rather clean sample of diffractive candidate events can be obtained.

The drawback of the LPS detector is its limited geometrical acceptance of about 6%. For the '94 data analysis about 400 events were available in the Q^2 range between 5 and 20 GeV^2. For details of the analysis performed with the LPS selection see [122].

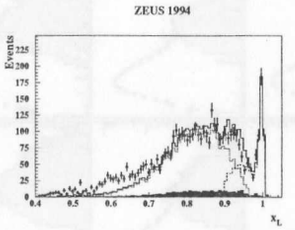

Figure 7.2: *The observed x_L spectrum in the data (dots). Overlaid is the result of fitting the distribution with a sum (full line) of the contribution due to proton dissociation (shaded area), of the contribution due to pion exchange (dotted line) and of the single photon dissociation signal (dashed line). For details see [122]*

7.1.2 Selecting Events with Large Rapidity Gap

As expected a large fraction of diffractive processes, observed at ZEUS and H1, does have a rapidity gap in the main detector between the scattered proton system and the hadronic activity generated by the dissociation of the photon, while large rapidity gaps are suppressed in non-diffractive DIS events. Therefore the presence of a rapidity gap has been used as a selection criterion for diffractive events [11, 18].

In figure 7.3a the η_{max} distribution for data is shown. Here η_{max} is the pseudorapidity of the most forward going "particle" (zufo). The measured distribution is compared to

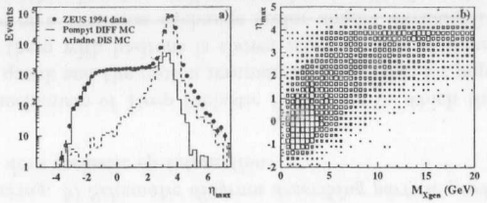

Figure 7.3: *a) The observed η_{max} spectrum in the data (dots). Overlaid is the result of fitting the diffractive (POMPYT) and non-diffractive (Ariadne) models. b) η_{max} versus the generated mass M_X for diffractive MC.*

a weighted sum of diffractive and non-diffractive MC models. It is seen, that for values of η_{max} up to 1–1.5 the non-diffractive DIS background is negligible and increases for values of η_{max} above 1.5–2. In previous ZEUS publications [11, 18] diffractive events were selected by requiring $\eta_{\max} < 1.5$. This cut selects a rather pure sample of diffractive events, useful to establish a signal but it limits acceptance for events with large M_X (see figure 7.3b).

In a later analysis [123] the cut on the direction of the total hadronic energy flow of the event determined from all the detected particles in the final state was used, in addition to the smaller rapidity gap ($\eta_{max} < 2.5$) cut, allowing a larger acceptance of diffractive events at higher M_X masses. The price of the extended selection criterion was a higher background which had to be subtracted statistically based on the non-diffractive MC models.

7.1.3 The M_X Method

The so called M_X method was developed in [19] for the diffractive analysis of small mass diffraction in the 1993 ZEUS data. The method of separating the diffractive and non-diffractive contributions is based on their very different M_X distributions.

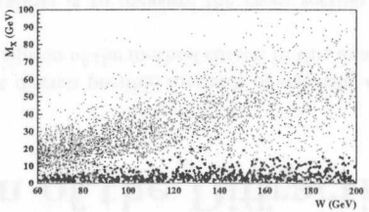

Figure 7.4: *Scatter plot of M_X versus W for data. The events with $\eta_{max} < 1.5$ are shown as large dots; they concentrate at small values of M_X.*

As a first illustration, figure 7.4 shows the distribution of M_X versus W for the data. Two distinct classes of events are observed, one concentrated at small M_X, the second extending to large values of M_X. Most of the events in the low M_X region exhibit a large rapidity gap, which is characteristic of diffractive production. This is shown in figure 7.4 where the events with a large (small) rapidity gap, $\eta_{max} < 1.5$ ($\eta_{max} > 1.5$) are marked by different symbols. A cut of $\eta_{max} < 1.5$ corresponds to a visible rapidity gap larger than 2.2 units since no particles were observed between the forward edge of the calorimeter

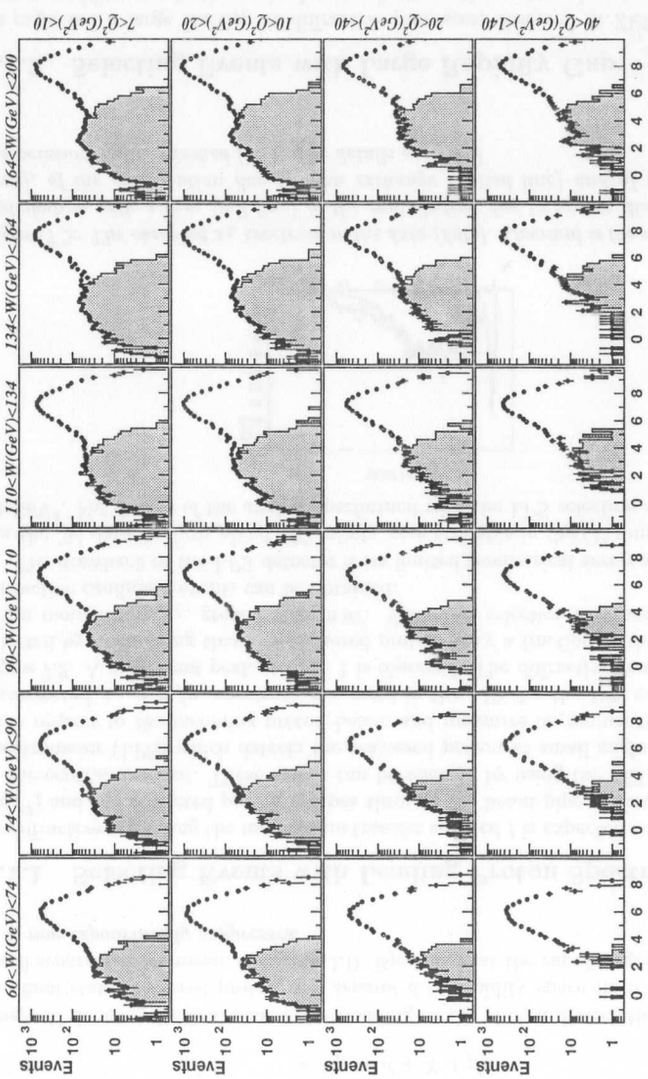

Figure 7.5: *Distributions of $\ln(M_X^2)$ for data, in all W and Q^2 intervals used in this analysis. The shaded histograms show the events which have $\eta_{max} < 1.5$ corresponding to a rapidity gap in the detector larger than 2.2 units.*

($\eta = 3.7-4.3$) and $\eta = 1.5$. For $\eta_{max} < 1.5$ the contribution from non-diffractive scattering is expected to be negligible [11].

The properties of the above scatter plot can be understood best when displayed as a function of $\ln M_X^2$ for different W and Q^2 intervals. In figure 7.5 we show the $\ln M_X^2$ distributions for all W and Q^2 intervals, used in this analysis. The distributions are not corrected for acceptance. In this representation, two distinct groups of events are observed. One can be seen to form a plateau-like structure at low $\ln M_X^2$, most notably at high W values. The second group, peaks at large values of $\ln M_X^2$ and exhibits a steep exponential fall-off towards smaller $\ln M_X^2$ values. Also note, that at a fixed Q^2 the mass peak moves to higher values as W increases, revealing more of the plateau-like structure at low $\ln M_X^2$ values. As already seen, most of the events under the plateau structure possess a large rapidity gap. This is illustrated by the shaded histograms which represent the events with $\eta_{max} < 1.5$.

It can also be seen, that the shape of the exponential fall-off is independent of W, a property which is best seen when the $\ln M_X^2$ distributions are replotted in terms of the scaled variable $\ln(W^2/M_X^2)$. This is shown in figure 7.6 where the $\ln(W^2/M_X^2)$ distributions are overlaid for three W intervals and four Q^2 intervals. The position of the high mass peak in $\ln M_X^2$ grows proportionally to $\ln W^2$ and the slope of the exponential fall-off towards small $\ln M_X^2$ values is approximately independent of W.

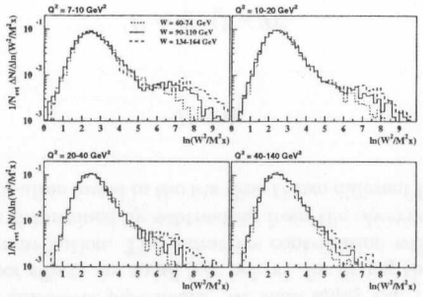

Figure 7.6: *Distribution of* $\ln(W^2/M_X^2)$ *for the* W *and* Q^2 *as indicated in the figure. Here* M_X *is the corrected mass; the distributions are the measured ones, not corrected for acceptance effects.*

As discussed in detail in [19], the exponential fall-off and the scaling in $\ln(W^2/M_X^2)$ are expected for non-diffractive DIS where the incident proton is broken up and the remnant of the proton is a colored object. This gives rise to a substantial amount of initial and final state state QCD radiation, followed by fragmentation, between the remnant and the current jet. According to pQCD the probability for producing a rapidity gap Δy between the emitted partons or, assuming parton-hadron duality, particles is expected to be exponentially suppressed.

The exponential behavior can be easily understood within a toy model in which the density of produced particles is constant as a function of rapidity y. For a center of mass energy, W, the rapidity distribution extends over a range $\ln W^2$ as depicted in figure 7.7, where the relation to the ZEUS detector is preserved (y increases to the left). For the sake of the argument we assume that the y distribution is flat between an effective y_{eff}^{max} and y_{eff}^{min}. The ZEUS central detector covers only part of the rapidity space, starting at

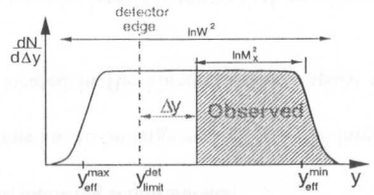

Figure 7.7: *Toy model*

y_{limit}^{det}. Let's further assume that for a given non-diffractive event the mass measured in the calorimeter is M_X^2 and the particle closest to the detector edge has been observed at $y_{limit}^{det} + \Delta y$,

$$\Delta y = \ln \frac{W^2}{M_X^2} - \underbrace{(y_{eff}^{max} - y_{limit}^{det})}_{\sim constant}. \tag{7.1}$$

Thus the distribution of $\ln(W^2/M_X^2)$ follows that of Δy.

The average number of particles expected in a rapidity interval Δy is,

$$\langle n \rangle = constant \cdot \Delta y.$$

If we further assume that the fluctuations in the local particle multiplicity is Poissonian, the probability of observing zero particles in Δy is

$$P_{\Delta y}(0; \langle n \rangle) = e^{-\langle n \rangle} = e^{-c\Delta y}.$$

Since in multi-particle production, the distribution of particles in the central region exhibits a plateau, we expect large rapidity gaps to be exponentially suppressed as $e^{-c\Delta y}$. Thus we also expect an exponential suppression of low $\ln M_X^2$ values in non diffractive events.

In reality, in $\gamma^* p$ interactions the rapidity distribution is not flat in the photon fragmentation region. However, as has been shown by the H1 Collaboration, in the central region the distribution is fairly flat [124]. Thus we expect the results of the toy model to be applicable to the real DIS data.

In principle, the exponential fall-off of the $\ln M_X^2$ distribution should start at the maximum value of $\ln M_X^2$ allowed by kinematics and acceptance, $\max(\ln M_X^2) = \ln W^2 -$ (2-3). The data in figures 7.5 and 7.6 break away from the exponential behavior towards high values of $\ln M_X^2$ leading to a rounding-off. It mainly results from the finite size of the selected W intervals, the edge of the calorimeter acceptance in the forward direction ($\eta_{edge} = 3.7$ to 4.3) and the finite resolutions with which W and M_X are measured. With good accuracy the exponential fall-off is observed for $\ln M_X^2 \leq \ln W^2 - \eta_0$, with $\eta_0 \approx 3$, over more than two units of rapidity.

In diffractive events, the system X resulting from the dissociation of the photon is, in general, almost fully contained in the detector while the outgoing proton or low mass nucleonic system, N, escapes through the forward beam hole. Furthermore, diffractive dissociation prefers small M_X values and leads to a mass distribution of the form $dN/dM_X^2 \propto 1/(M_X^2)^{(1+n)}$ or

$$\frac{dN}{d\ln M_X^2} \sim \frac{1}{(M_X^2)^n}, \tag{7.2}$$

approximately independent of W. At high energies and for large M_X one expects $n \approx 0$ leading to a roughly constant distribution in $\ln M_X^2$. Such a mass dependence is seen in diffractive dissociation of pp scattering (see e.g. [7]).

To summarize this section, the diffractive contribution is *identified* as the excess of events at small M_X above the exponential fall-off of the non-diffractive contribution with $\ln M_X^2$. This definition is equivalent to the requirement of selecting a sample of events that are characterized by *not exponentially suppressed rapidity gap* Δy between system X and the edge of the detector. The exponential fall-off permits the subtraction of the non-diffractive contribution and therefore the extraction of the diffractive contribution without assuming a precise M_X dependence of the latter. The M_X distribution is expected to be of the form

$$\frac{dN}{d\ln M_X^2} = D + c\exp(b\ln M_X^2), \quad \text{for } \ln M_X^2 \leq \ln W^2 - \eta_0 \tag{7.3}$$

Here, D denotes the diffractive contribution, the second term represents the non-diffractive contribution and $\ln W^2 - \eta_0$ is the maximum value of $\ln M_X^2$ up to which the exponential behavior of the non-diffractive part holds. We shall apply Eq. 7.3 in a limited range of $\ln M_X^2$, where detector effects are small (see below), for fitting the parameters b and c of the non-diffractive contribution. The diffractive contribution will *not* be taken from the fit result but will be determined by subtracting from the observed number of events the non-diffractive contribution found in the fits. For D two different forms will be considered; either

$$D = d_0 \tag{7.4}$$

or

$$D = d_1 \cdot (1-\beta)^{\lambda} \tag{7.5}$$

where d_0, d_1 and λ are parameters. The second form was chosen so that the distortions of the diffractive contribution at high masses could be taken into account in the fit (see discussion below).

7.2 Reconstruction of Diffractive Events

The aim of this analysis is to measure the cross section for diffractive production of mass M_X as a function of W and Q^2. We chose the Double-Angle (DA) method to reconstruct kinematical variables of the events, because it is less sensitive to scale errors in the energy measurement of the final state particles. The events must then be divided into bins, so that the cross section can be evaluated in each of them. To obtain the most precise physics picture, the kinematic phase space, and the number of bins, should be as large as possible. However, there are limitations, due to the detector acceptance, resolution and available number of events.

In our analysis, the Q^2 range is taken to be between 7 and 140 GeV^2. The low Q^2 limit is motivated by the requirement that the low mass states, dominated by the decay products of the vector mesons production, be contained in the calorimeter. This is equivalent to a minimum transverse momentum in the detector which is guaranteed if Q^2 is larger than 7 GeV and W is not too high. The upper Q^2 limit is dictated by the available event statistics.

In order to determine the W range we have studied the quality of reconstructing Q^2_{DA} and W_{DA}. The result is presented in figure 7.8, where the average values of the fractional deviations $\Delta W_{DA}/W$ and $\Delta Q^2_{DA}/Q^2$ as a function of the true W are shown, for three mass intervals. The *offsets*, are defined as $\Delta W_{DA} = W_{DA} - W$ and $\Delta Q^2_{DA} = Q^2_{DA} - Q^2$. Systematic offsets of W_{DA} and Q^2_{DA} from their true values at low and high W values are observed. The deviations are particularly marked for W_{DA} at low W and for Q^2_{DA} at high W, in all three mass intervals. The measurement will thus be limited to the range of W between 60 and 200 GeV.

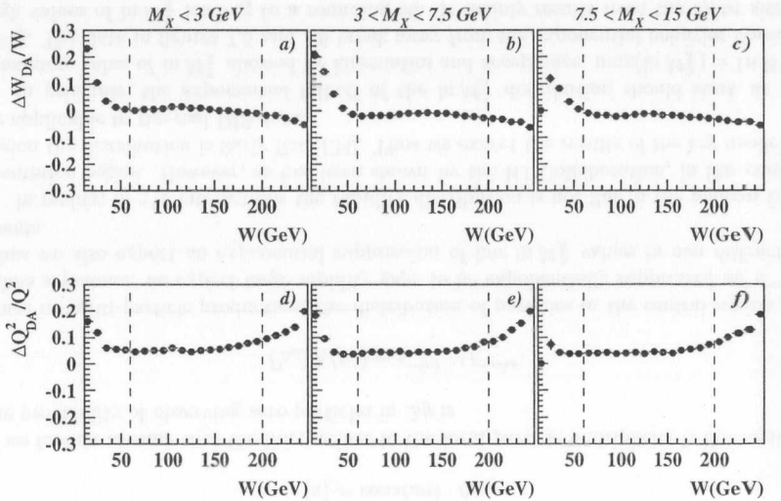

Figure 7.8: *The average values of the fractional deviations* $\Delta W_{DA}/W$ *and* $\Delta Q^2_{DA}/Q^2$ *as a function of the true* W*, for three mass intervals as indicated in the figure. The* offsets, *are defined as* $\Delta W_{DA} = W_{DA} - W$ *and* $\Delta Q^2_{DA} = Q^2_{DA} - Q^2$.

The requirement that events should be reconstructed in the kinematic region $60 < W < 200$ GeV and $7 < Q^2 < 140$ GeV^2 reduces the total number of selected DIS events to 164,978. This is more than 6 times the increase in the number of events available in the 1993 diffractive analysis.

The number of bins in the three dimensional space of W, Q^2 and M_X that we want to study is limited by the following requirements:

- the population in bins has to be large enough to avoid large statistical fluctuations;
- the bins must be located in the kinematic phase space where the acceptance of events is high;
- the bin dimensions must be large enough so that an adequate fraction of the events originating in a given bin are measured in the same bin.

These requirements can be quantified by introducing bin quality parameters, acceptance and purity, where

$$acceptance \equiv \frac{\#\text{ of events generated and remaining in bin } j}{\#\text{ of events generated in bin } j}$$

and

$$purity \equiv \frac{\#\text{ of events generated and reconstructed in bin } j}{\#\text{ of events reconstructed in bin } j}$$

Both quantities are determined using the diffractive MC sample. The acceptance is a measure of the combined effect of the event selection efficiency and detector fiducial acceptance, whereas the purity is the measure of the bin contamination due to event migration from adjacent bins. The purity is therefore sensitive to the resolution and systematic shifts in the reconstruction of the kinematic variables. To fulfill the requirement of high purity the bin dimension is required to at least satisfy the following conditions:

$$\begin{aligned} \Delta Q^2 &\gtrsim \sigma(Q^2), \\ \Delta W &\gtrsim \sigma(W), \\ \Delta M_X &\gtrsim \sigma(M_X). \end{aligned}$$

We chose four Q^2 intervals, 7 - 10 GeV^2, 10 - 20 GeV^2, 20 - 40 GeV^2, and 40 - 140 GeV^2, the average values being 8 GeV^2, 14 GeV^2, 27 GeV^2, and 60 GeV^2, respectively. The intervals in W were chosen so as to have equidistant bins in $\ln W^2$ providing approximately equal number of events in each W bin. For the bin width, $\Delta \ln W^2 = 0.4$ was used, commensurate with the resolution for $\ln W^2$.

The resolutions in $\ln W^2$ using zufos and cell methods were determined with the diffractive Monte Carlo sample. The average value of $\Delta \ln W^2$ and its RMS are shown in figure 7.9 as a function of W. The resolution improves as W and/or Q^2 increase; it is substantially better for the zufo method as compared to the cell method. The resolution obtained with zufos is less than 0.24 at low W and Q^2 values, decreasing to 0.09 for the highest W and Q^2.

The resolution in Q^2 using the cell and zufos methods was determined in an analogous manner. In figure 7.10 the offset $\Delta Q^2 = Q^2_{rec} - Q^2_{gen}$ and RMS, for the two reconstruction methods and the different Q^2 and W intervals, are shown. The zufo method yields slightly smaller RMS values. The RMS spread increases slowly with W but stays well below one third of the widths of the chosen Q^2 intervals.

The plots showing resolution and migration of kinematic variables, as well as the acceptance and purity for all the bins considered, are presented in appendix A (see figures A.1 - A.7). For most of the bins used the acceptance is greater then 60%. The bins purity are typically greater then 50%.

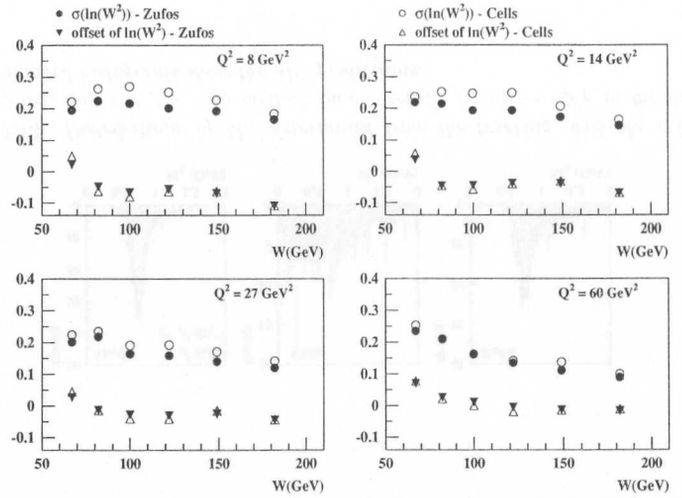

Figure 7.9: *The RMS and offset* $\Delta \ln W^2 = \ln W^2_{rec} - \ln W^2_{gen}$ *for* $\ln W^2$ *as a function of* W *for different* Q^2 *intervals for the zufo (full symbols) and cell methods (open symbols).*

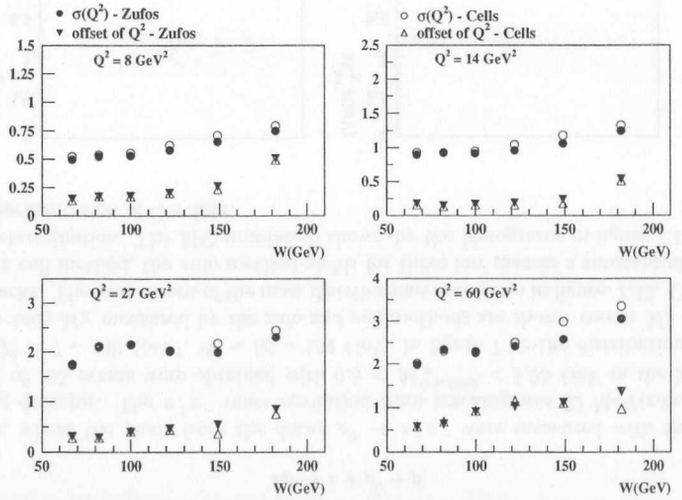

Figure 7.10: *The RMS and offset* $\Delta Q^2 = Q^2_{rec} - Q^2_{gen}$ *for* Q^2 *as a function of* W *for different* Q^2 *intervals for the zufo (full symbols) and cell methods (open symbols).*

7.2.1 Mass Determination

The mass M_X of the system X was determined according to the following equation:

$$(M_X^{meas})^2 = (\sum_j E)^2 - (\sum_j p_x)^2 - (\sum_j p_y)^2 - (\sum_j p_z)^2 \,, \tag{7.6}$$

where sums, $\sum_j$, run either over all calorimeter cells or over all zufos not assigned to the scattered electron. The mass M_X^{rec} reconstructed in this way has to be corrected for energy losses in the passive material in front of the calorimeter.

The correction factor $f(M_X)$, for $M_X^{gen} < 15$ GeV, was obtained using the diffractive MC sample, from the average ratio of reconstructed to generated mass M_X,

$$f(M_X^{MCrec}) = \frac{M_X^{MCrec}}{M_X^{MCgen}} \,,$$

as a function of M_X, W and Q^2. In the range $1.5 < M_X < 15$ GeV, the dependence of $f(M_X^{rec})$ on W, Q^2 and M_X was found to be small ($\pm 3\%$). The correction factor, as a function of M_X is shown in figure 5.26, averaged over W and Q^2. It was found to be $f_{cell}(M_X^{rec}) = 0.68$ for the cell method and $f_{zufo}(M_X^{rec}) = 0.80$ for the zufo method. The same correction factor was used for masses below 1.5 GeV.

The correction was applied to obtain from the reconstructed mass the corrected mass value, $M_X^{cor} = M_X^{rec}/f(M_X^{rec})$.

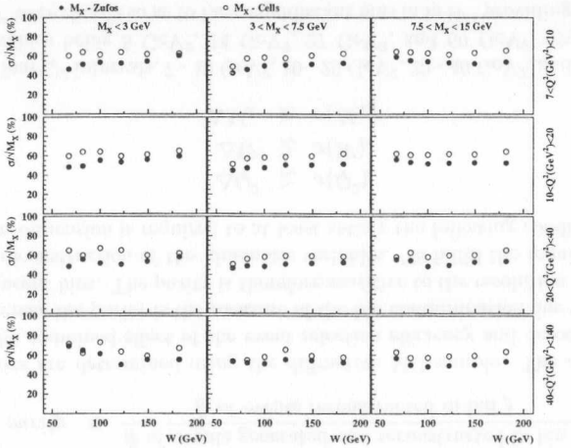

Figure 7.11: *The scaled mass resolution (r.m.s.) $\sigma(M_X)/\sqrt{M_X}$ obtained with the zufo (solid dots) and cell (open dots) as a function of W for different M_X and Q^2 intervals.*

Figure 7.11 shows $\sigma(M_X)/\sqrt{M_X}$ as a function of W for the different M_X and Q^2 intervals. For both methods, the distributions are centered around zero. However, the mass resolution is better with the zufo method. The resolution changes little with M_X, W or Q^2. On average $\sigma(M_X)/\sqrt{M_X} \approx 50\%\text{GeV}^{\frac{1}{2}}$ for the zufo method and about 20% larger for the cell method.

A test of the MC result for the mass measurement at low M_X values was performed studying the reaction

$$ep \to e + \rho^0 + p,$$

in data, where the pions from the decay $\rho^0 \to \pi^+\pi^-$ were measured with the central tracking detector. The $\pi^+\pi^-$ mass resolution from tracking was 22 MeV(r.m.s.) [108]. A total of 195 events were obtained with $0.5 < M_{\rho^0}^{tracking} < 1.25$ GeV in the kinematic range $Q^2 = 7 - 140$ GeV^2, $W = 60 - 134$ GeV. In figure 7.12 the distributions of (the uncorrected) M_X measured by the zufo and cell methods are shown versus M_X obtained from tracks. The projections of the mass distributions are shown in figure. 7.13. Compared with the cell method, the zufo method yields for these low masses a substantially better mass determination. The MC simulation shown by the histograms in figure 7.13 gives a good representation of the data.

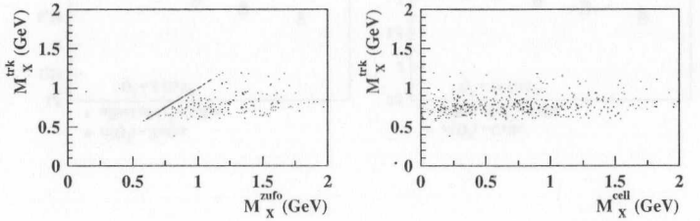

Figure 7.12: *Event candidates for $ep \to e\rho^0 p$ in the data. Left: the mass M_X^{trk} determined from tracks versus the mass M_X^{zufo} determined by the zufo method; Right: M_X^{trk} versus M_X^{cell}.*

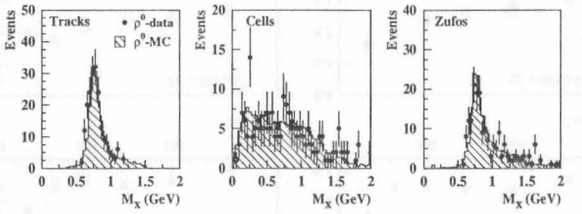

Figure 7.13: *Distributions of M_X determined from the tracking, with the cell method (uncorrected) and with the zufo method (uncorrected), for $ep \to e\rho^0 p$ in the data. The skewed hatched histograms show the MC predictions.*

In summary, the W, Q^2 and M_X determinations with zufo's are superior to the cell method. For this reason, only the results obtained with the zufo method will be presented. All M_X results presented below refer to M_X^{cor}.

7.3 Test of the M_X Method

7.3.1 Comparison of MC Simulation with data

In figure B.1 the $\ln M_X^2$ distributions for data (full points) are compared with the CDM-BGF MC model predictions for non-diffractive production (histograms). The MC distributions were normalized such that they agreed in the peak region with the number of events observed in the data. The normalization factor was found to be approximately W independent and weakly dependent on Q^2. The MC simulation reproduces the gross features of the peak at large masses coming from non-diffractive production but one observes a systematic shift of the peak towards lower $\ln M_X^2$ values by about 0.4 (0.35, 0.2, 0.1) units at $Q^2 = 7$ (10, 27, 60) GeV^2. In order to obtain a better description of the data the MC distributions were shifted by these amounts producing the distributions shown in figure B.2 which give a satisfactory agreement with the data in the region of the exponential fall-off. In the following these shifted MC distributions will be used for simulating the non-diffractive contribution.

For MC simulation of the diffractive contribution RAPGAP (HJP1) was used. In figure B.3 the $\ln M_X^2$ distributions are shown for diffractive events at the generator level and at the detector level for all (W, Q^2) bins. At the generator level M_X is defined as the mass of the generated system X. In comparison with the MC-generated distributions the MC-measured distributions show a depletion of events at the high mass end, which show up as an excess at lower mass values ($\ln M_X^2 \approx 4 - 6$). These distortions are caused mainly by particles lost through the forward beam hole. The distortions are small in the region used in the fitting and will be taken into account by the extended fit, see Eq. 7.5.

In figure B.4 the sum of the MC predictions for the non-diffractive and diffractive contributions are compared with the data. Each of the two contributions was multiplied by normalization factor chosen such as to obtain the best overall agreement between simulation and data.

7.3.2 Testing of the Fit Procedure

In order to test the fit procedure, for extraction of the non-diffractive contribution, the combined diffractive and non-diffractive MC sample was used. In a first step the exponential slope b for the non-diffractive part was determined from the non-diffractive sample alone yielding the *expected* values for the slope b. In a second step the slope b was determined from the fit to the combined sample and compared with the *expected* values.

The fits were performed in the range $\ln Q^2 < \ln M_X^2 < \mathrm{Max}(\ln M_X^2)$. The lower limit for $\ln M_X^2$ was chosen according to the expectation of the diffraction models, that for $M_X^2 > Q^2$ the diffractive contribution is of the form given by Eq. 7.4. The upper limit $\mathrm{Max}(\ln M_X^2)$ was chosen as the maximum value of $\ln M_X^2$ up to which the data exhibit an exponential behavior. The maximum value of $\ln M_X^2$ was determined by fitting the $\ln M_X^2$ distributions for each (W, Q^2) interval with a varying maximum value of $\ln M_X^2$. In most (W, Q^2) intervals a boundary as a function of $\mathrm{Max}(\ln M_X^2)$ was observed beyond which the χ^2 probability for the fit dropped rapidly. The boundary marks the location where the distribution starts to deviate from an exponential behavior. The boundary was found to be at $\ln M_X^2 = \ln W^2 - \eta_0$, with $\eta_0 \approx 3$.

In figure B.5 the $\ln M_X^2$ distributions for the non-diffractive sample at the detector and the generator levels, are presented. The mass M_X at the generator level is defined

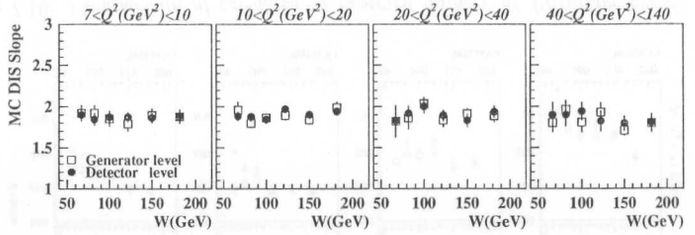

Figure 7.14: *Distribution of the slope b obtained from fitting the non-diffractive contribution predicted by CDM-BGF at the generator (open points) and detector (solid points) as a function of W for the Q^2 values indicated.*

as the invariant mass of all particles with $\eta < 4.5$. The slope b determined from fitting the $\ln M_X^2$ distributions to Eq. 7.3 (with $D = 0$) is shown in figure 7.14 for all W, Q^2 bins and within the $\ln M_X^2$ intervals described above. Within errors, the same b value is obtained at the generator and the detector levels. The fits were also performed allowing D in Eq. 7.3 to be a free parameter. The results, again, within errors yielded the same b values. From this MC test it is seen, that both sets of distributions, at the generator and detector levels, show the same exponential fall-off and that the exponential fall-off of the non-diffractive contribution is not affected by detector effects.

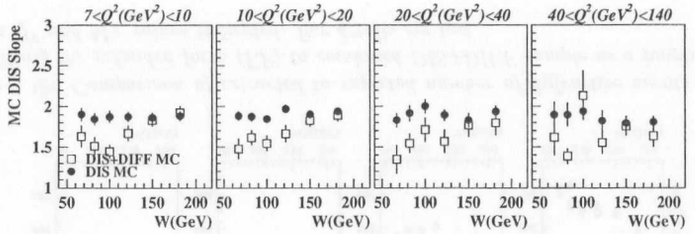

Figure 7.15: *Distribution of the slope b obtained from fitting the non-diffractive contribution predicted by CDM-BGF at the detector level (solid points) and extracted by fitting the standard form (SF) to combined DIS+DIFF sample (open points) as a function of W for the Q^2 values indicated. For details see text.*

In figures B.6 and B.7 the MC measured $\ln M_X^2$ distributions for the combined sample are shown. Two types of fits were performed. In the so-called standard form (SF) the diffractive contribution D in Eq. 7.3 was assumed to be constant (Eq. 7.4); in the extended form (EF) D was assumed to be given by Eq. 7.5. The corresponding results from the fits for the non-diffractive contribution together with the non-diffractive sample are shown in the figures. The values of the slope b from the SF fit are compared in figure 7.15 with the *expected* values. The SF results in lower b values at low W's and yields b values which are consistent with the input values for the last two W intervals in all Q^2 intervals. The reason for this can be clearly seen in figure B.6. In the low W intervals there is not enough of a plateau-like structure to constrain the d_0 parameter in the standard fit. In addition, the

loss of particles down the beam-hole further leads to distortions at high $\ln M_X^2$ values by making the diffractive spectrum under the high mass peak not plateau-like, thus leading to shallower b slopes. In the high W intervals the plateau is well visible and allows to constrain the d_0 and b slope very well. The distortions of the diffractive spectrum at high W begin past the point of $\ln M_X^2$ maximum value up to which the fit is performed. Therefore, at high W we find the slopes to be consistent with the expected values.

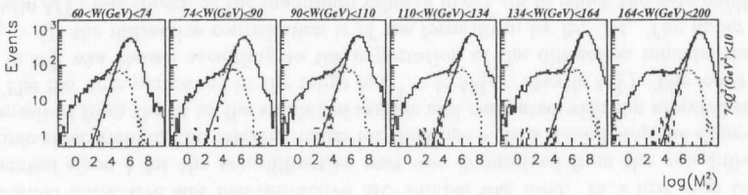

Figure 7.16: *Example of an extended fit for $Q^2 = 8$ GeV. The solid histogram shows the combined diffractive and non-diffractive MC samples. The dashed histogram shows the non-diffractive sample. The dotted histogram shows the diffractive sample. The straight solid line indicates the non-diffractive contribution and the curves indicate the combined diffractive and non-diffractive contributions, as determined from the extended fit.*

Example of the fits to the extended form, for $Q^2 = 8$ GeV, are shown in figure 7.16. In the figure the results obtained for the non-diffractive contribution are indicated by straight lines and the curves indicate the combined diffractive and non-diffractive contributions. The values of the slope b from the extended fit, in all (W, Q^2) intervals, are compared in figure 7.17 with the *expected* values. It is seen, that the fits with the extended form yield b values consistent with the expected values. They are consistent with being independent of W and Q^2, as well.

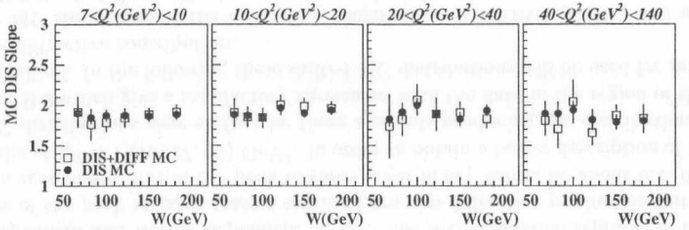

Figure 7.17: *Distribution of the slope b obtained from fitting the non-diffractive contribution predicted by CDM-BGF at the detector level (solid points) and extracted by fitting the extended form (EF) to combined DIS+DIFF sample (open points) as a function of W for the Q^2 values indicated. For details see text.*

As mentioned before, the number of diffractive events in a given M_X bin will be determined by subtracting from the observed number of events the non-diffractive contribution as obtained from the fit. In figure 7.18 the number of diffractive events obtained from the extended fits for different W and Q^2 values are compared with the *expected* number of

diffractive events present in the diffractive MC sample. The number of diffractive events found with the extended fits agree very well with the input values in all M_X, W, Q^2 bins. The agreement is good up to $\pm 4\%$, except for one bin at high M_X, Q^2 and low W, where the background due to non-diffractive contribution is higher than 60%.

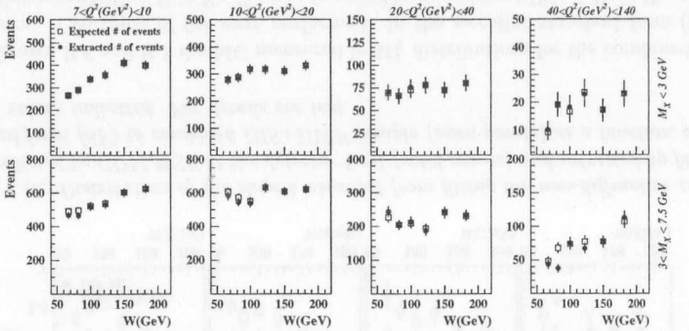

Figure 7.18: *Comparison of extracted to expected number of diffractive events obtained from fitting the extended form (EF) to combined DIS+DIFF sample as a function of W for the Q^2 and M_X values indicated. For details see text.*

For the standard form fit (see figure 7.19) the agreement is satisfactory in all W and Q^2 intervals only for low M_X bins. In the high M_X and low W regions the number of extracted diffractive events is significantly lower as compared to the expected numbers. This was anticipated, since the extracted b slopes were found to be shallower than expected. For the high W bins and for all Q^2 and M_X bins the agreement is also satisfactory within $\pm 4\%$.

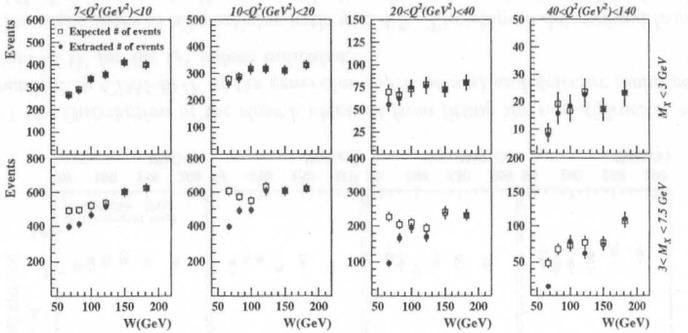

Figure 7.19: *Comparison of extracted to expected number of diffractive events obtained from fitting the standard form (SF) to combined DIS+DIFF sample as a function of W for the Q^2 and M_X values indicated. For details see text.*

As noted above, the slope b of the input distributions with good precision is independent of W and Q^2. For this reason, the statistical precision for the subtraction of the non-diffractive contribution can be improved by fitting all bins with a common b value. This common value of b was determined as the average of the b values from those W and Q^2 bins where in the mass range $3.0 < M_x < 7.5$ GeV the background contribution from non-diffractive scattering was less than 10% (last two W intervals and first three Q^2 intervals) which ensures that the behavior of the diffractive and non-diffractive parts are well separable. This prescription yielded for the MC combined non-diffractive and diffractive samples the value of $b = 1.86 \pm 0.05$, in good agreement with the b values found from the fits to the non-diffractive sample alone, $b = 1.87 \pm 0.03$. The standard and extended fits were then repeated using the common slope value as a fixed parameter for b. The number of diffractive events obtained in this way are compared in figures 7.20 and 7.21 with the input numbers, for the SF and EF fits, respectively. Good agreement is observed for all W and Q^2 intervals at low M_X values. In the second mass interval $3.0 < M_X < 7.5$ GeV the agreement is also satisfactory, except for the lowest W intervals where the number of extracted events is found to be systematically lower with respect to number of expected events. For these bins we find that the amount of background due to non-diffractive component is typically greater than 20-30%, as estimated from the extrapolation of the slope into the low mass region.

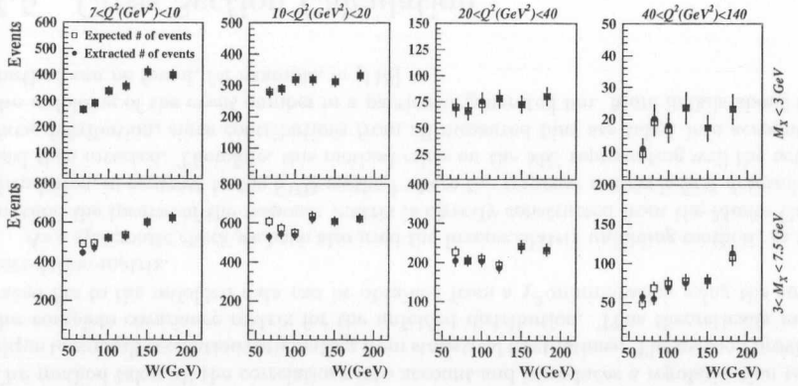

Figure 7.20: *Comparison of extracted to expected number of diffractive events obtained from fitting the standard form (SF), with a fixed slope for non-diffractive contribution, to combined DIS+DIFF sample as a function of W for the Q^2 and M_X values indicated. For details see text.*

In summary, the non-diffractive contribution in the W, Q^2 and M_X bins under study will be determined in two steps. In a first step the $\ln M_X^2$ distributions in all W, Q^2 bins will be fit using Eq. 7.3, and the slope b will be treated as a free parameter. Then the common slope b will be determined as an average over the fitted b values from those W and Q^2 bins where the non-diffractive contribution to the bin $3.0 < M_X < 7.5$ GeV, according to the fit, is less than 10%. In the second step, the fits will be repeated using the common slope value as a fixed parameter. Application of this procedure to MC

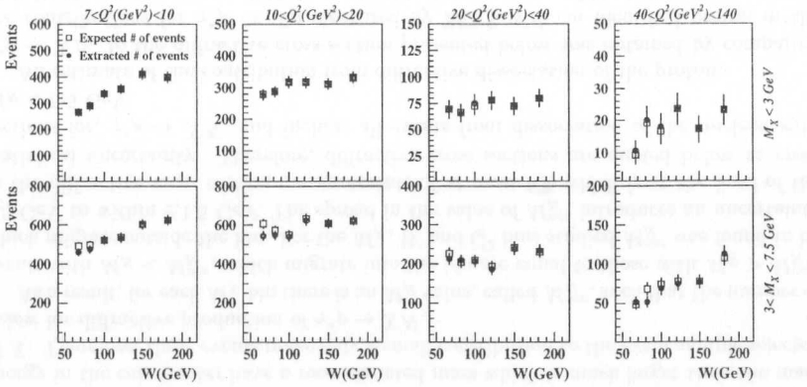

Figure 7.21: *Comparison of extracted to expected number of diffractive events obtained from fitting the extended form (EF), with a fixed slope for non-diffractive contribution, to combined DIS+DIFF sample as a function of W for the Q^2 and M_X values indicated. For details see text.*

measured events shows that the diffractive contribution can be extracted reliably from the combined diffractive and non-diffractive samples. Since the extended form for the diffractive contribution yields somewhat better results, this form will be used for the final values. As a systematic check we will include the results from the EF using slopes as determined in each interval separately. In addition, only bins which are found to have less than 30% of background due to non-diffractive component as determined from the fits, will be used in the final analysis.

7.4 Unfolding

After the background subtraction the measured number of events in the bins do not yet reflect the true number of diffractive events. Here, as in any other experiment, the distributions of experimentally measured quantities differ from the corresponding real distributions due to finite detector resolutions. Furthermore the ZEUS trigger system and the final data selection criteria result in acceptance losses in the detector. This can be represented mathematically as follows:

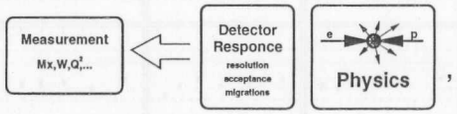

,

where the response of the detector is coded in a response matrix. The general procedure to correct the observed data for these smearing, migration and acceptance or efficiency effects is called "unfolding", and consists of finding the inverse of the response matrix.

The unfolding problem belongs to a class of ill-posed problems [125], which are unstable against small variations in the initial system. Because of inevitable statistical errors

in the measured distribution and the presence of noise, the solution is usually oscillating and the exact solution is lost. This problem has been studied in various forms, giving rise to a number of methods described in literature. For instance, a method based on Bayes theorem was proposed in [126]. The author managed to avoid partly the inversion difficulties by using a non-linear iterative procedure, leading asymptotically to the unfolded distribution. Another way of overcoming the instability of unfolding is to use some kind of regularization condition, based on some a *priori* information about the solution. For example, we can demand that the true solution has minimum curvature (i.e. is quite smooth).

In this thesis the unfolding procedure was based on the *Singular Value Decomposition* (SVD) [127] of the response matrix and is applicable to multidimensional distributions. The method takes all the correlations into account and introduces a regularization technique to smooth oscillations originating from statistical fluctuations. The method provides the complete covariance matrix for the unfolded distribution. Thus theoretically motivated fits to the unfolded data can be obtained from a χ^2-minimization using the entire correlation-matrix.

As a systematic check we have also used the Inverse Matrix unfolding method. In this method the inverse of the response matrix is directly constructed from the Monte Carlo simulation, in contrast to the SVD method where the response matrix is first determined and then inverted. Therefore, this method relies on the MC representing well the actual data distribution, since contributions from all measured bins are taken into account in the unfolding of the event number in a particular generated bin. More details about this method can be found, for example, in [115].

7.5 Cross Section Calculation

The Born cross section for a bin in Q^2, W and M_X can be determined from the unfolded number of events in the bin, N, by the following equation:

$$\frac{d^3\sigma(W,Q^2,M_X)}{d\ln W dQ^2 dM_X} = N \cdot \frac{1}{\Delta \ln W \Delta Q^2 \Delta M_X} \cdot \frac{1}{\mathcal{L}} \cdot \frac{1}{(1+\delta_r)} \tag{7.7}$$

where

- $\Delta \ln W \Delta Q^2 \Delta M_X$ – is the volume of the bin in Q^2-W-M_X space,
- $\mathcal{L}$ – is the integrated luminosity, and
- δ_r – is the QED radiative correction needed to convert the measured cross section into the Born cross section.

The radiative corrections, δ_r, were calculated using the RapGap Monte Carlo, which is interfaced to HERACLES for simulation of radiative effects. In figure 7.22 the value of $\delta_r = (\sigma^{rad} - \sigma^{Born})/\sigma^{Born}$ is shown for all the bins considered in this analysis. The σ^{rad} was determined by running RapGap MC with QED radiative corrections turned on. The σ^{Born} was determined in a similar manner, but with QED radiative correction turned off. The radiative corrections are typically less than $\pm 10\%$. These corrections were applied to every bin, on a bin by bin bases. The dependence of radiative corrections on the pomeron structure function was estimated to be negligible [128].

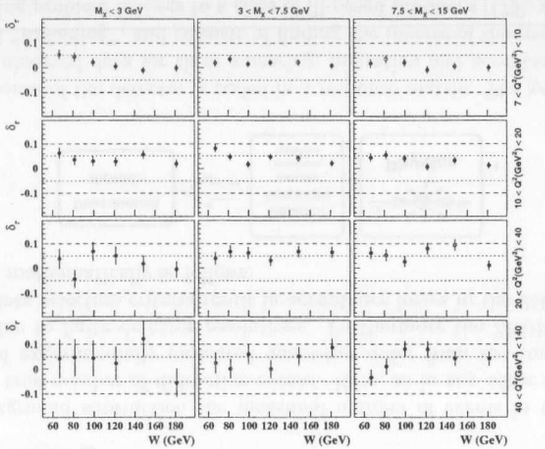

Figure 7.22: *Radiative corrections needed to convert the measured cross section into the Born cross section.*

7.6 Contribution from nucleon dissociation

The contribution from the diffractive process where the proton dissociates into a small mass which remain undetected in the experiment,

$$ep \to e + X + N,$$

was studied with Monte Carlo simulation based on the triple-Regge formalism [46] and an M_N distribution as measured in the single diffractive dissociation in pp (and $\bar{p}p$) scattering. Analysis as a function of M_N showed that for $M_N < 2$ GeV basically no energy is deposited in the calorimeter while for events with $M_N > 6$ GeV there are almost always energy deposits in the calorimeter. In general events where decay particles from N deposit energy in the calorimeter have a reconstructed mass which is much larger than the mass of X. Therefore, these events make only a small contribution to the event sample selected below for diffractive production of $\gamma^* p \to XN$.

As a result, for each M_X bin there is an M_N value, called M_N^{acc}, such that the number of events with $M_N < M_N^{acc}$, which migrate into the bin are equal to those with $M_N > M_N^{acc}$, which migrate outside the bin. For the M_X, W and Q^2 bins studied M_N^{acc} was found to be 5.5 GeV to within ± 1.5 GeV. The spread in the value of M_N^{acc} introduces an uncertainty in the diffractive cross section measurements of at most 6% which is at the level of the statistical uncertainty. Therefore, diffractive cross sections are quoted below as cross sections for, $\gamma^* p \to XN$, and include all events from dissociation of the nucleon with $M_N < 5.5$ GeV.

An estimate of the contribution from diffractive dissociation of the proton, $\gamma^* p \to XN$, to the diffractive cross section presented below was obtained by comparing the contributions for $\gamma^* p \to Xp$ measured by ZEUS with an identified proton in the LPS [122] and for $\gamma^* p \to XN$ determined in this analysis. This led to the fractional contribution from double dissociation $r^{dissoc} \equiv XN/(Xp + XN) = 31 \pm 13\%$.

Chapter 8

Diffractive Cross Section

8.1 Diffractive ep to $\gamma^* p$ Cross Section

The cross section of interest to understand the properties of diffractive dissociation of virtual photon is the $\gamma^* p$ absorption cross section. A virtual photon emitted by an electron appears in two polarization states, transverse (T) and longitudinal (L). The total $\gamma^* p$ cross section is usually understood, by analogy to the structure function formalism, as the sum of the longitudinal, σ_L, and transverse, σ_T, contributions.

The relation between the diffractive $ep \to eXp$ cross section and the $\gamma^* p \to Xp$ cross section can be expressed as follows [22]:

$$Q^2 \frac{d\sigma^D_{ep}(M_X, W, Q^2)}{dM_X\, d\ln W^2 dQ^2} = \frac{\alpha}{2\pi} Y_+ \sigma^D_{\gamma^* p} \left[1 - \frac{y^2}{Y_+} \frac{R}{1+R}\right], \tag{8.1}$$

where $Y_+ = 1 + (1-y)^2$ and $R = \sigma^D_L / \sigma^D_T$.

In order to determine $\sigma^D_{\gamma^* p} = \sigma^D_L + \sigma^D_T$, some knowledge of R is necessary. Assuming a finite value of R the correction to $\sigma^D_{\gamma^* p}$ can be substantial only at high W values, since $y \approx W^2/s$. In the extreme case that $\sigma^D_L \gg \sigma^D_T$, the correction term will increase $\sigma^D_{\gamma^* p}$ by at most 11% for the highest W bin (164 - 200 GeV). If $\sigma^D_L = Q^2/M_X^2 \cdot \sigma^D_T$, as in the Vector Dominance Model [6], the correction term increases $\sigma^D_{\gamma^* p}$ by at most 10% (6%, 2%) for the bins with the highest W, Q^2 values and $M_X < 3$ GeV ($3 - 7.5$ GeV, $7.5 - 15$ GeV).

Since the measurement of R can not be performed it will be set to zero in the analysis and possible consequences of this assumption will be quantified in the discussion of the results. Therefore, the $\sigma^D_{\gamma^* p}$ is obtained from ep cross section as follows:

$$\frac{d\sigma^D_{\gamma^* p}(M_X, W, Q^2)}{dM_X} \equiv \frac{d(\sigma^D_T + \sigma^D_L)}{dM_X} \approx \frac{2\pi}{\alpha} \frac{Q^2}{Y_+} \frac{d\sigma^D_{ep}(M_X, W, Q^2)}{dM_X\, d\ln W^2 dQ^2}. \tag{8.2}$$

8.2 The Diffractive Differential Cross Section $\frac{d\sigma^D_{\gamma^* p}}{dM_X}$

The mass distribution for all W and Q^2 intervals in terms of $\ln M_X^2$ were subjected to the fit procedure described before. The fits were performed for the two forms (SF and EF) for D with the slope b as a free parameter. The resulting values for b are presented in figure 8.1. The observed behavior of the slope values was similar to that seen in the test with the controlled MC samples. The standard form resulted in lower b values at low W's

and agreed with the slopes obtained from the extended fit at high W's. For the extended form fit the slopes, within errors, were found to be W and Q^2 independent.

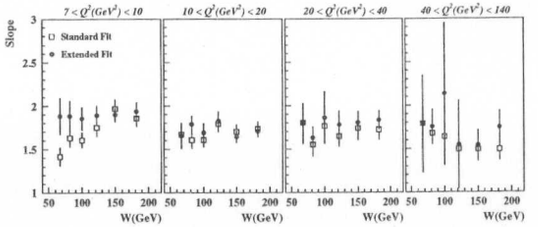

Figure 8.1: *Average slope values for SF and EF fits to the $\ln M_X^2$ distribution in data.*

Therefore, as was stated earlier, we determined the common b slope from the W = 134-164, 164-200 GeV and Q^2 = 7-10, 10-20, 20-40 GeV^2 intervals, where the non-diffractive contribution to the bin $3.0 < M_X < 7.5$ GeV was found to be less than 10%. The average value of $\bar{b}$ came out to be 1.80±0.04 and 1.78±0.04 for the extended and standard form fits, respectively. Note, that these values are lower that those observed in the MC test, $\bar{b}_{MC} = 1.87 \pm 0.03$. The disagreement between data and MC makes background subtraction with the MC samples unreliable. The fits were repeated using the $\bar{b}$, determined from the EF fit, as the common value for all W and Q^2 intervals. The results are presented in figure 8.2, showing the $\ln M_X^2$ distributions together with the fitted curves. The solid straight lines show for all Q^2 and W bins the exponential fall-off of non-diffractive contribution.

The number of diffractive events, N^D_{meas}, was determined in all Q^2 and W bins for the three M_X intervals by subtracting from the observed number of events, N_{obs}, the contribution from remaining beam gas scattering, N^{gas}, and the nondiffractive contribution, $N^{nondiff}$, obtained from the EF fit with a fixed $\bar{b}$ slope,

$$N^D_{meas} = N_{obs} - N^{gas} - N^{nondiff}.$$

The N^{gas} background was determined from the number of events, that passed the final selection cuts and originated from unpaired proton or electron (pilot) bunches and was scaled with the ratio of the currents in the paired and unpaired bunches. The distributions in $\ln M_X^2$ for data and the background due to e- and p-gas are shown in figure 8.2. The beam gas background is concentrated at low $\ln M_X^2$, Q^2 and high W values; they are negligible for Q^2 above 20 GeV^2. The maximum contribution found in any of the bins was 25% from electron-gas and 10% from proton-gas scattering.

From N^D_{meas} the number of produced diffractive events, was obtained with the SVD unfolding procedure which takes into account bin-to-bin migration, trigger efficiency and acceptance losses. The number of unfolded events is denoted by N^D_{prod}.

For the final result, only bins where the fraction of non-diffractive background was less than 30% and the purity was above 30% are quoted. The average purity in a W, Q^2 and M_X bin was about 50%.

The average differential cross section for ep scattering, in a W, Q^2 and M_X bin, was obtained by dividing the number of unfolded events, N^D_{prod}, by the luminosity, the bin widths and the QED radiative correction, see Eq. 7.7. For the unfolded sample, the first mass bin was assumed to range from $2m_\pi$, where m_π is the pion mass. The diffractive differential cross section $d\sigma^D_{\gamma^* p}/dM_X$ was determined according to Eq. 8.2.

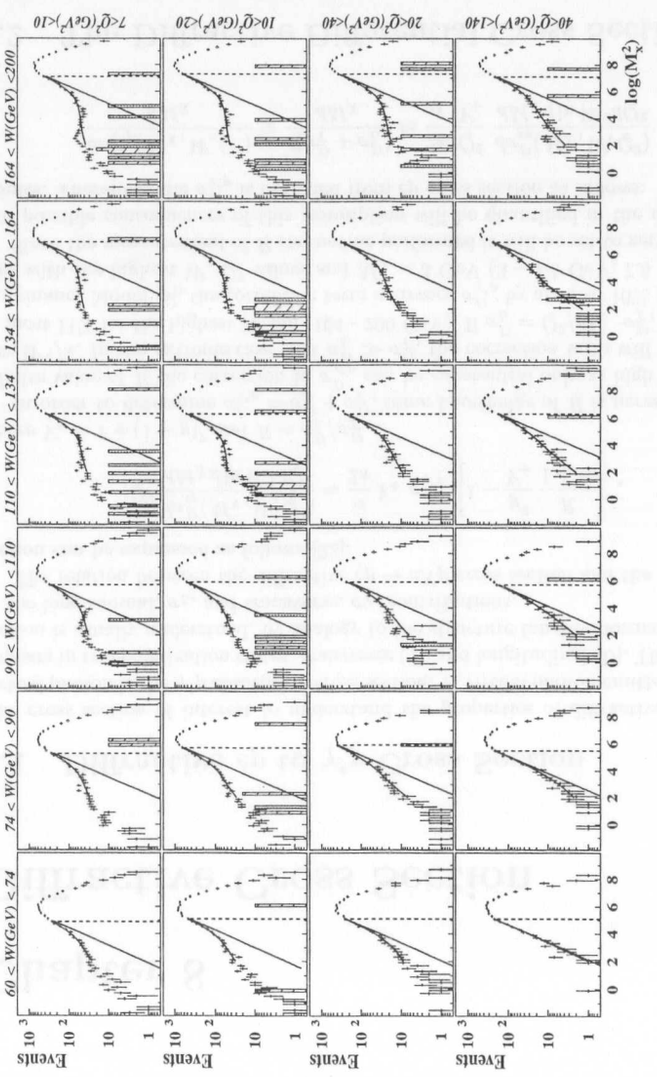

Figure 8.2: *Distributions of* $\ln(M_X^2)$ *for data, in* W *and* Q^2 *intervals as indicated in the figure. The skewed histogram shows the contribution of e-gas and shaded histogram the contribution due to p-gas, scaled with the ratio of the currents in the paired and unpaired bunches. The straight solid line indicates the non-diffractive contribution and the curves indicate the combined diffractive and non-diffractive contributions, as obtained with a fixed slope from the extended fit. For details see text.*

In the last step, we applied the so called bin center correction and all the cross sections are quoted at M_X = 2, 5, 11 GeV and Q^2 = 8, 14, 27, 60 GeV^2. For W the results are quoted at the logarithmic means of the W intervals.

This procedure was based on a parameterization of the diffractive cross section using the model of Bartels et al. [129] (BEKW), which describes the shapes of the observed distribution fairly well. The main correction comes from the ratio of kinematical factors, and makes the correction model independent.

The results for the diffractive cross section $\gamma^* p \to XN$, $M_N < 5.5$ GeV, are presented in figure 8.3 as a function of W and in figure 8.4 as a function of Q^2. The inner error bars show the statistical error. The full bars show the statistical and systematic errors added in quadrature. The systematic errors were obtained by varying the experimental cuts and were based on the considerations discussed in the next section.

The energy dependence of the diffractive cross section in figure 8.3 is seen to rise with W at all Q^2 values for the M_X values of 2 and 5 GeV. From comparison with published data [130, 131, 132, 133], about 20% of the diffractive cross section observed in the mass bin $M_X < 3$ GeV at $7 < Q^2 < 20$ GeV^2 results from the production of the vector mesons $V = \rho^0, \phi$ via $\gamma^* p \to VN$.

In figure 8.4 a fast decrease with Q^2 is observed for small M_X which is similar to the behavior of DIS vector meson production [130, 131, 132, 133]. For high M_X region the decrease becomes slower, indicating that the high mass dissociation of the virtual photon becomes increasingly more important as Q^2 grows.

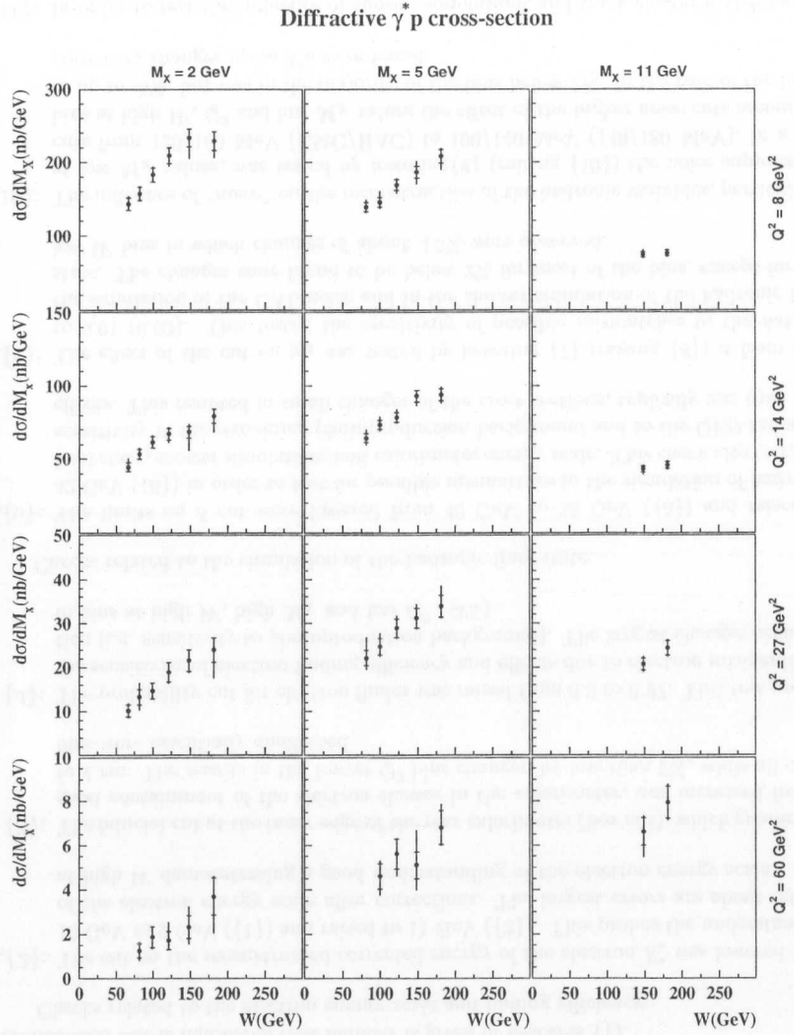

Figure 8.3: *The differential cross section $d\sigma^D_{\gamma^* p \to XN}/dM_X$ as function of virtual photon proton center of mass energy W, for the M_X and Q^2 values as denoted in the figure. The inner error bars show the statistical errors and the full bars the statistical and systematic errors added in quadrature. The overall normalization uncertainty of 3% is not included.*

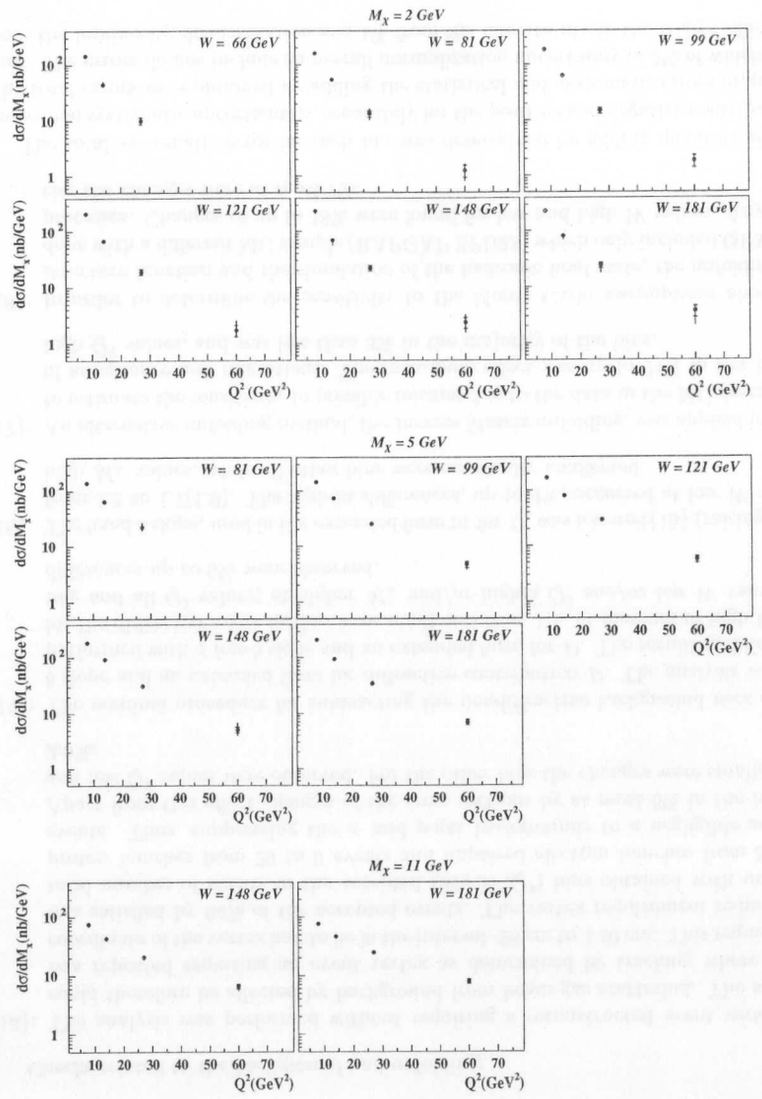

Figure 8.4: *The differential cross section $d\sigma^D_{\gamma^* p \to XN}/dM_X$ as function of Q^2, for the M_X and W values as denoted in the figure. The inner error bars show the statistical errors and the full bars the statistical and systematic errors added in quadrature. The overall normalization uncertainty of 3% is not included.*

8.2.1 Systematic Errors

The systematic errors on the cross sections were estimated by varying the cuts and algorithms used to select the events. The bin-by-bin changes from the nominal value were recorded. The systematic checks performed in this analysis are listed below and for reference each test is numbered (the number is given in brackets {}).

Checks related to the electron energy scale and finding efficiency:

{1},{2}: The cut on the reconstructed corrected energy of the electron E'_e was lowered from 10 GeV to 9 GeV ({1}) and raised to 11 GeV ({2}). This probes the understanding of the electron energy scale after corrections. The largest errors are about $\pm 0.5\%$ at high W demonstrating a good understanding of the electron energy scale.

{3}: The fiducial cut at the inner edge of the rear calorimeter (box cut), which guarantees good containment of the electron shower in the calorimeter, was increased from 3 to 4 cm. The results in the lowest Q^2 bins changed by less than 2%, while all other bins were essentially unaffected.

{4}: The probability cut for electron finder was raised from 0.9 to 0.97. This test probes the sensitivity of electron finding efficiency and effects due to electron misidentification (i.e. sensitivity to photoproduction background). The largest changes occurred in bins at high W, high M_X and low Q^2 (-3%).

Checks related to the simulation of the hadronic final state:

{5},{6}: The limits on δ cut were lowered from 40 GeV to 38 GeV ({5}) and raised to 42 GeV ({6}) in order to test for possible mismatches in the simulation of hadronic final state, shower simulations and calorimeter energy scale. This check also tests the sensitivity to the remaining photoproduction background and to the QED radiative effects. This resulted in small changes of the cross sections, typically less than 2%.

{7},{8}: The effect of the cut on y_{jb} was tested by lowering {7} (raising {8}) it from 0.02 to 0.01 (0.03). This tested the sensitivity of possible mismatches to the data in the simulation of the CAL noise and in the shower simulation of the hadronic final state. The changes were found to be below 2% for most of the bins, except for the low W bins in which changes of about +5% were observed.

{9},{10}: The influence of "noise" on the reconstruction of the hadronic variables, particularly at low M_X values, was tested by lowering{9} (raising {10}) the noise suppression cuts from 120/160 MeV (EMC/HAC) to 100/140 MeV (140/180 MeV). In a few bins at high W, Q^2 and low M_X values the effect of the higher noise cuts amounted to up to -5%, but was in the majority of the bins below 2%. In the case of the lower noise cuts changes up to 3% were found.

{11}: In order to test the influence of shower simulations and track-cluster matching the cell islands to cone island recombination probabilities were changed from 0.3/0.1 (HAC1(or EMC)→EMC and HAC2→HAC1) to 0.1/0.05. Except for a few bins at high W, low Q^2 and low M_X values, where the changes of up 3.5% were observed, the changes were typically less than 1.5%.

{12}: In order to test the influence of hadronic final state simulation, electron energy corrections and kinematic variable reconstruction, the energy and the cells of the the electron were taken that of the identified TowerIsland. The biggest difference 2.5% occurred at high W, low Q^2 and high M_X values, while all other bins were essentially unaffected. This indicates a good simulation of the hadronic final state.

Checks related to the background and unfolding:

{13}: The analysis was performed without requiring a reconstructed event vertex and could therefore be affected by background from beam-gas scattering. The analysis was repeated requiring an event vertex as determined by tracking where the z-coordinate of the vertex had to lie in the interval -28 cm to +40 cm. This requirement was satisfied by 94% of the accepted events. The vertex requirement reduced the total number of events in the accepted (M_X,W,Q^2) bins obtained with unpaired proton bunches from 20 to 0 events and unpaired electron bunches from 50 to 9 events. Thus, suppressing the e- and p-gas backgrounds to a negligible amount. Apart from this effect changes of the cross sections by at most 6% in the high W and low Q^2 values were observed. For the other bins the changes were smaller than 2.5%.

{14}: The nominal procedure for subtracting the nondiffractive background uses a fixed b slope and an extended form for diffractive contribution D. The analysis was also performed with a free b slope and an extended form for D. The resulting differences for the diffractive cross section were small, less than 1%, at medium to high W, low M_X and all Q^2 values; at higher M_X and/or higher Q^2 and/or low W values the differences up to 6% were observed.

{15},{16}: The fixed b slope, used in the extended form fit for D, was lowered{15} (raising {16}) from 1.8 to 1.7(1.9). The highest differences, up to 4%, occurred at low W and/or high M_X values, while all other bins were essentially unaffected.

{17}: An alternative unfolding method, the Inverse Matrix unfolding, was applied in order to estimate the sensitivity to possible mismatches to the data in the MC description of acceptance and migrations. The maximum effect was up to 24% in few bins at high Q^2 values, and was less than 3% in the majority of the bins.

{18}: In order to determine the sensitivity to the Monte Carlo assumptions about the structure function and the simulation of the hadronic final state, the unfolding was done with a different MC sample (RAPGAP ZPD93) which only included QPM type processes. Changes of up to 18% were found for low and high W values. Anywhere else the changes were at most 7%.

The total systematic error for each bin was determined by adding quadratically the individual systematic uncertainties, separately for the positive and negative contributions. The total errors were obtained by adding the statistical and systematic errors in quadrature. The errors do not include an overall normalization uncertainty of 3% of which 2% is from the luminosity determination and 1% from the uncertainty in the trigger efficiency.

8.3 W Dependence of Cross Section

In a Regge - type description [46, 134], the W dependence of the diffractive cross section is of the form

$$\frac{d\sigma^D_{\gamma^* p}(M_X, W, Q^2, t)}{dt dM_X} \propto (W^2)^{2\alpha_{I\!P}(0)-2} \cdot e^{(B+2\alpha'_{I\!P} \ln(W^2/(M_X^2+Q^2)))t} , \quad (8.3)$$

where $\alpha_{I\!P}(t) = \alpha_{I\!P}(0) + \alpha'_{I\!P} t$ is the Pomeron trajectory and B and $\alpha'_{I\!P}$ are parameters. The cross sections in each M_X and Q^2 interval were fitted to the form

$$\frac{d\sigma^D_{\gamma^* p}(M_X, W, Q^2)}{dM_X} \propto (W^2)^{(2\overline{\alpha_{I\!P}}-2)} , \quad (8.4)$$

where $\overline{\alpha_{I\!P}}$ stands for $\alpha_{I\!P}(t)$ averaged over the t distribution. The fit was performed by considering different $\overline{\alpha_{I\!P}}$ and the normalization constants in all M_X and Q^2 intervals as free parameters. The systematic uncertainties were estimated by repeating the fit independently for every source of systematic error. The observed deviations were added in quadrature. The results for each systematic check are shown in figure 8.5. The results of the fit are presented in figure 8.6 and the obtained values of $\overline{\alpha_{I\!P}}$ as a function of Q^2 for two mass values are summarized in figure 8.7.

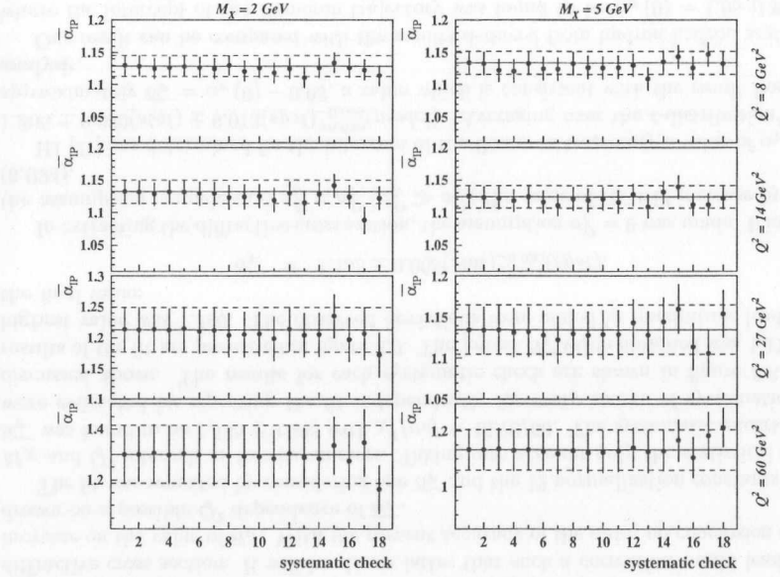

Figure 8.5: *Sensitivity of the value of $\overline{\alpha_{I\!P}}$ to the different sources of systematic uncertainties. The central line and the band show for the standard fit the value of $\overline{\alpha_{I\!P}}$ and ± 1 s.d. The dots give $\overline{\alpha_{I\!P}}$ value with its uncertainty obtained by repeating the analysis for each systematic check labeled 1 through 18 as described in the text.*

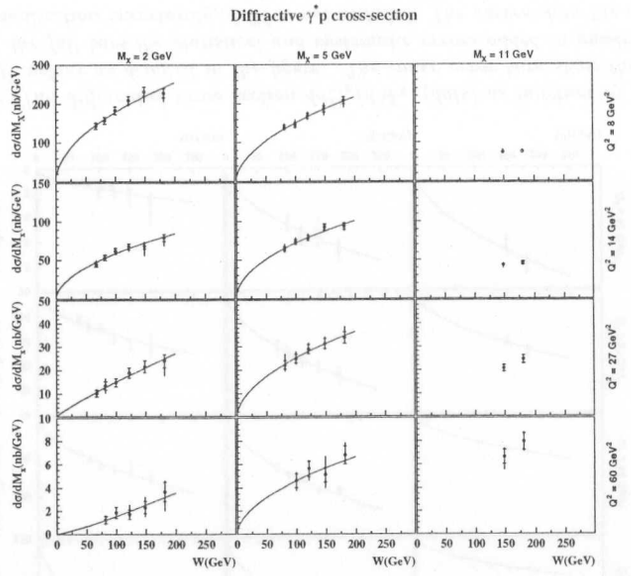

Figure 8.6: *The differential cross section $d\sigma^D_{\gamma^* p \to XN}/dM_X$ (dots) as function of W, for the M_X and Q^2 values as denoted in the figure. The inner error bars show the statistical errors and the full bars the statistical and systematic errors added in quadrature. The overall normalization uncertainty of 3% is not included. The curves show the results from fitting all cross sections to the form $d\sigma^D/dM_X \propto (W^2)^{(2\overline{\alpha_{I\!P}}-2)}$, by considering different $\overline{\alpha_{I\!P}}$ and the normalization constants in all intervals as free parameters.*

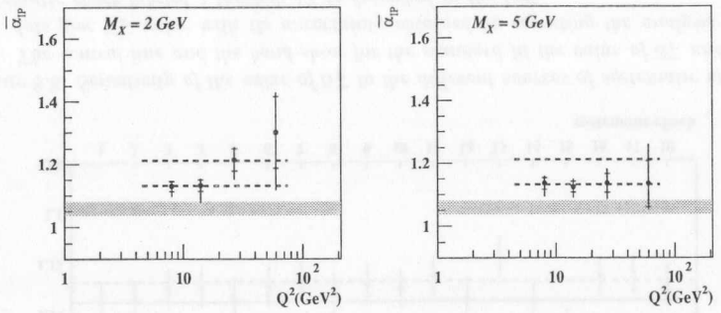

Figure 8.7: *Values of $\overline{\alpha_{I\!P}}$ as a function of Q^2 for two different M_X mass values. The shaded area corresponds to the 1σ range of $\overline{\alpha_{I\!P}} = \alpha_{I\!P}(0) - 0.03$, inferred from the fit of Cudell et al.[135]. A 1 sigma error band (dashed lines) for the measurement of $\alpha_{I\!P}(0)$ from the H1 Collaboration is superimposed. In order to compare with our measurement the H1 value was lowered by 0.03.*

In the fitted M_X and Q^2 bins the value of $\overline{\alpha_{I\!P}}$ lies above the estimates deduced from hadron-hadron scattering [135, 136], taking into account that the averaging over t-distribution tends to lower the value of $\alpha_{I\!P}(0)$ typically by 0.03. Note that no correction was made to account for possible contribution of longitudinally polarized photons to the diffractive cross section. It will be shown latter that such a correction would lead to an increase on the value of $\overline{\alpha_{I\!P}}$. With the present accuracy of the data, no conclusion can be drawn on a possible Q^2 dependence of $\overline{\alpha_{I\!P}}$.

The fit was repeated by considering one $\overline{\alpha_{I\!P}}$ and the 12 normalization constants for all M_X and Q^2 intervals as free parameters. Taking into account only the statistical errors, $\overline{\alpha_{I\!P}}$ was found to be 1.135 ± 0.008 with $\chi^2/ndf = 46.78/50$. The systematic uncertainties were estimated by repeating the fit independently for every source of systematic error discussed above. The results for each systematic check are shown in figure 8.8. The results of the fit are presented in figure 8.9. The lowest $\overline{\alpha_{I\!P}}$ value obtained was 1.118, the highest value was 1.146. The observed deviations were added in quadrature leading to the final value:

$$\overline{\alpha_{I\!P}} \;=\; 1.135 \pm 0.008(stat)^{+0.011}_{-0.030}(syst).$$

In extracting the diffractive cross section, the assumption $\sigma_L^D = 0$ was made. If instead, the assumption is made that $\sigma_L^D = \sigma_T^D$ ($\sigma_L^D \gg \sigma_T^D$) the value of $\overline{\alpha_{I\!P}}$ will increase by 0.012 (0.024).

H1 [21] has determined for the intercept of the Pomeron trajectory a value of $\alpha_{I\!P}(0) = 1.203 \pm 0.020(stat) \pm 0.013(syst)^{+0.030}_{-0.035}(model)$. Averaging over the t-distribution[1] gives approximately $\overline{\alpha_{I\!P}} = \alpha_{I\!P}(0) - 0.03$, a value which is consistent with the result from this analysis.

Our result can be compared with the results deduced from hadron-hadron scattering where the intercept of the Pomeron trajectory was found to be $\alpha_{I\!P}(0) = 1.08$ [136] and $\alpha_{I\!P}(0) = 1.096^{+0.012}_{-0.009}$ [135]. Averaging over t reduces these values by about 0.03[2] leading to $\overline{\alpha_{I\!P}} = 1.05$ and $\overline{\alpha_{I\!P}} = 1.066^{+0.012}_{-0.009}$, respectively.

The value of $\overline{\alpha_{I\!P}} = 1.135 \pm 0.008(stat)^{+0.011}_{-0.030}(syst)$ obtained in this analysis is larger than those obtained from analyses of soft hadronic cross sections. It also exceeds the values obtained from the analyses of the photon diffractive dissociation cross section at $Q^2 = 0$, by ZEUS and H1 [16, 17].

[1] When parameterizing the t-distribution by $d\sigma/dt \propto exp[(B + 2\alpha'_{I\!P} \ln(1/x_{I\!P}))t]$ the difference $\alpha_{I\!P}(0) - \overline{\alpha_{I\!P}}$ is determined mainly by B and $\alpha'_{I\!P}$. H1 quotes $B = 4.6$ GeV^{-2} and $\alpha'_{I\!P} = 0.26$ GeV^{-2}.

[2] We assumed here values of B and $\alpha'_{I\!P}$ to be the same as quoted by H1.

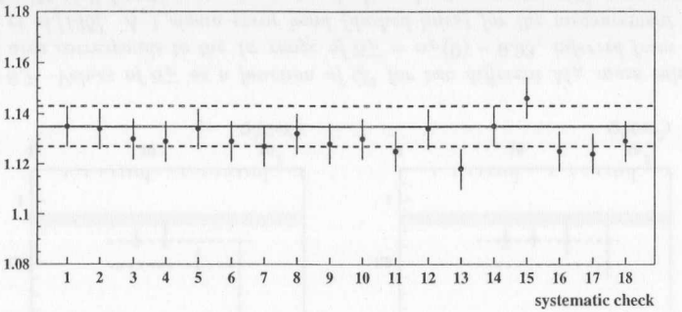

Figure 8.8: *Sensitivity of the value of $\overline{\alpha_{I\!P}}$ to the different sources of systematic uncertainties. The central line and the band show for the standard fit the value of $\overline{\alpha_{I\!P}}$ and ± 1 s.d. The dots give $\overline{\alpha_{I\!P}}$ value with its uncertainty obtained by repeating the analysis for each systematic check labeled 1 through 18 as described in the text.*

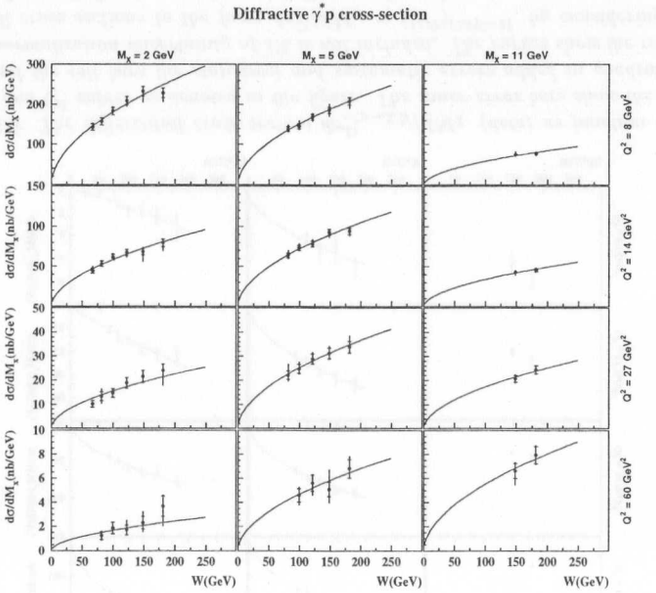

Figure 8.9: *The differential cross section $d\sigma^D_{\gamma^* p}/dM_X$ (dots) as function of W, for the M_X and Q^2 values as denoted in the figure. The inner error bars show the statistical errors and the full bars the statistical and systematic errors added in quadrature. The overall normalization uncertainty of 3% is not included. The curves show the results from fitting all cross sections to the form $d\sigma^D/dM_X \propto (W^2)^{(2\overline{\alpha_{I\!P}}-2)}$, by considering one $\overline{\alpha_{I\!P}}$ and different normalization constants for the various (M_X, Q^2) intervals as free parameters.*

8.4 Comparison with total $\gamma^* p$ cross section.

The ratio of the diffractive cross section to the total virtual photon proton cross section,

$$r^D = \frac{\int_{M_a}^{M_b} dM_X \, d\sigma^D_{\gamma^* p \to XN}/dM_X}{\sigma^{tot}_{\gamma^* p}}, \tag{8.5}$$

is presented in figure 8.10 as a function of W for the different M_X and Q^2 values. For each M_X bin, the diffractive cross section was integrated over the bin width $M_a < M_X < M_b$. The total cross section was taken from ZEUS F_2 measurements performed with the 1994 data [137] using $\sigma^{tot}_{\gamma^* p}(W, Q^2) = \frac{4\pi^2 \alpha}{Q^2(1-x)} F_2(x \approx \frac{Q^2}{W^2}, Q^2)$.

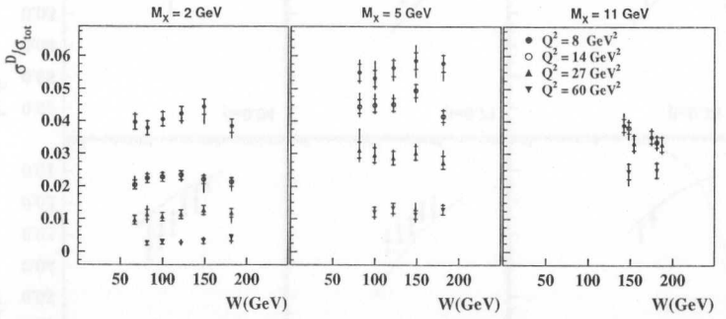

Figure 8.10: *The ratio of diffractive cross section, integrated over the M_X intervals, $\sigma^D = \int_{M_a}^{M_b} dM_X \, d\sigma^D_{\gamma^* p \to XN}/dM_X$, for $M_N < 5.5$ GeV, to the total cross section for virtual photon proton scattering, $r^D = \sigma^D/\sigma^{tot}_{\gamma^* p}$, as a function of W for the M_X and Q^2 values indicated. $\sigma^{tot}_{\gamma^* p}$ was taken from ZEUS F_2 measurement with the 1994 data [137].*

The data show that the ratio r^D, within errors, is consistent with W independence. The same conclusion is reached when comparing the value of the power $a^D = 0.52 \pm 0.03(stat)^{+0.04}_{-0.12}(syst)$ for energy dependence of diffractive cross section, W^{a^D}, with the power $a^{tot} = 0.55 \pm 0.02$ obtained for $\sigma^{tot}_{\gamma^* p}$ energy dependence in the same W and Q^2 interval. In the Regge phenomenology one would expect the ratio to increase with W as $W^{a^D/2}$. Hence, taking the W dependence found for diffractive cross section the power a^{tot} would have been expected to be $a^{tot} = a^D/2 = 0.26 \pm 0.02(stat)^{+0.02}_{-0.06}(syst)$ in clear disagreement with the data.

The observation of similar W dependence for diffractive and total cross sections suggests that the mechanism responsible for diffractive scattering in DIS is the same as in total $\gamma^* p$ scattering, that is dominated by the gluon exchange. The same W dependence for the diffractive and total cross sections has been predicted in [138].

The Q^2 dependence of r^D at low mass is much stronger than at larger masses where it almost disappears, indicating that the diffractive production of a fixed low mass is suppressed roughly by an extra power of Q^2 relative to the total cross section. This is not in contradiction to ZEUS earlier observation [18] of DIS diffraction as a leading twist effect, since the scaling variable is β and not M_X^2. For a fixed M_X the increase of Q^2 corresponds to an increase in β. The Q^2 dependence observed here is not unlike the one observed in exclusive vector meson production.

8.5 Diffractive Structure Function of the Proton

The concept of a diffractive structure function introduced in [8] is based on the assumption that diffraction is mediated by the exchange of a colorless object, called a Pomeron, which is composed of partons. The differential diffractive cross section $d\sigma^D_{\gamma^* p}/dM_X$ of the proton can be related to the diffractive structure function via Jacobian transformation as follows [139]:

$$F_2^{D(3)} = \frac{1}{4\pi\alpha_{em}} \frac{Q^2(W^2+Q^2)^2}{2M_X W^2} \frac{d\sigma^D_{\gamma^* p}}{dM_X}. \tag{8.6}$$

For $W^2 \gg Q^2$, which holds for this analysis, the above equation can be rewritten as:

$$x_{I\!P} \cdot F_2^{D(3)} \approx \frac{1}{4\pi\alpha_{em}} \frac{Q^2(Q^2+M_X^2)}{2M_X} \frac{d\sigma^D_{\gamma^* p}}{dM_X}. \tag{8.7}$$

$F_2^{D(3)}$ can be interpreted in terms of parton densities which for diffractive scattering specify the probability of finding a parton carrying a momentum fraction $x = \beta x_{I\!P}$ of the proton momentum.

The results of this measurement can be compared with a measurement of $F_2^{D(3)}$ with the LPS in the ZEUS experiment [122]. In order to do so the $\sigma^D_{\gamma^* p}$ has been transformed into $F_2^{D(3)}$ after correcting for contribution due to double dissociation. The comparison is shown in figure 8.11. All the points from the inclusive analysis have $x_{I\!P}$ less than 0.01, justifying their interpretation in terms of Pomeron exchange. The LPS measurements extend to higher values of $x_{I\!P}$ and indicate a slower $x_{I\!P}$ dependence. In the region of overlap the agreement is good. The slow $x_{I\!P}$ dependence of LPS results can be interpreted as due to contributions of sub-leading Regge trajectory.

To estimate the contribution of sub-leading Regge trajectories, we have used the calculation of Golec-Biernat and Kwiecinski [140] (GK). As expected the contribution is large in the IP region covered by the LPS and negligible for $x_{I\!P}$ less than 0.01, see figure 8.11.

Our measurement have been also compared to the parameterization of the Pomeron contribution to $F_2^{D(3)}$ as obtained by H1 Collaboration. This is at the same time a good representation of their measurements for $F_2^{D(3)}$ for $x_{I\!P}$ less than 0.01, in the bins covered by this analysis. In general the agreement is good in the overall normalization. However, the H1 measurements exhibit a steeper $x_{I\!P}$ dependence. This can also be seen in the dependence of $\overline{\alpha_{I\!P}}$ as a function of Q2 shown in figure 8.7, where our measurements of $\overline{\alpha_{I\!P}}$ are compared to that of H1.

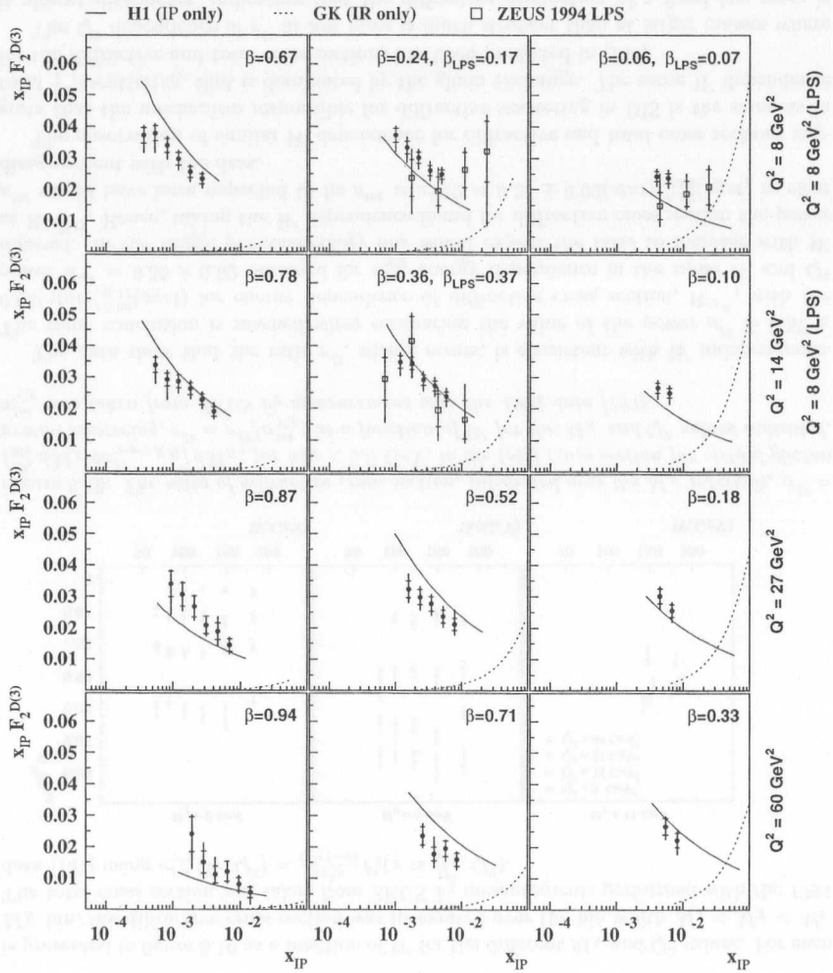

Figure 8.11: *The measured values of $x_{I\!P} \cdot F_2^{D(3)}$ from the M_X method (solid dots) and the LPS method (open squares). The value of $F_2^{D(3)}$ from the M_X method was scaled with 0.69, to account for double dissociation. The solid lines are the H1 parameterization of $F_2^{D(3)}$(IP only) to their data. The dotted lines are the calculations from GK for the Reggion contribution.*

8.5.1 The $x_{I\!P}$ dependence of $x_{I\!P} \cdot F_2^{D(3)}$

It has been suggested in [8] on the basis of expectations from Regge theory that the diffractive structure function, $F_2^{D(3)}(x_{I\!P}, \beta, Q^2)$, could be factorized into two terms as follows:

$$F_2^{D(3)}(x_{I\!P}, \beta, Q^2) = f_{I\!P/p}(x_{I\!P}) \cdot F_2^{I\!P}(\beta, Q^2), \tag{8.8}$$

where $f_{I\!P/p}(x_{I\!P})$ is the Pomeron flux factor and parameterizes the probability of emitting the $I\!P$ from the proton vertex carrying a fraction $x_{I\!P}$ of the proton momentum. The second term $F_2^{I\!P}(\beta, Q^2)$ is called the Pomeron structure function and can be described in terms of the Pomeron parton densities which depend on β and Q^2.

The data in figure 8.11 show that $x_{I\!P} F_2^{D(3)}$ decreases smoothly with increasing $x_{I\!P}$ and reflects the observed rapid rise of the diffractive cross section with increasing W. To test the hypothesis of factorization, the data were fitted with a universal dependence on $x_{I\!P}$ such that

$$x_{I\!P} \cdot F_2^{D(3)}(x_{I\!P}, \beta, Q^2) = (\frac{x_0}{x_{I\!P}})^n \cdot F_2^{I\!P}(\beta, Q^2), \tag{8.9}$$

where x_0 is the average value of the measured $x_{I\!P}$, $x_0 = 0.0042$. Using this form we can identify the Pomeron structure function to be given by $F_2^{I\!P}(\beta, Q^2) = x_0 F_2^{D(3)}(x_0, \beta, Q^2)$. Note that there is an arbitrary normalization factor for the flux and therefore also for $F_2^{I\!P}$. The parameter n can be related to the power of the energy dependence of the diffractive cross section, $n \simeq a^D/2 = 2(\overline{\alpha_{I\!P}} - 1)$.

The 12 values of $F_2^{I\!P}(\beta_i, Q_i^2)$ and a universal n were treated as fit parameters in the measured β and Q^2 bins. A good fit to the data was obtained yielding

$$n = 0.270 \pm 0.016(stat)^{+0.022}_{-0.060}(syst).$$

The fit was also performed assuming n to depend logarithmically on Q^2. This resulted in small differences that were included in the errors given for $F_2^{I\!P}$.

The fact that a good fit was found with a single value for n shows that the data are consistent with the assumption that $F_2^{D(3)}$ factorizes into a flux factor depending only on $x_{I\!P}$ and a structure function $F_2^{I\!P}$ which depends on β and Q^2.

8.5.2 The β dependence of $F_2^{I\!P}(\beta, Q^2)$

The $F_2^{I\!P}(\beta, Q^2)$ values obtained from the fit are presented in figure 8.12 as a function of β for all Q^2 values. It should be stressed that these $F_2^{I\!P}$ values do not depend on whether the $F_2^{D(3)}$ factorizes into a Pomeron flux factor or not, since *i)* $F_2^{I\!P}(\beta, Q^2) = x_0 F_2^{D(3)}(x_0, \beta, Q^2)$ and the fit was only used to inter/extrapolate to $x_{I\!P} = x_0$ and *ii)* a fit with a Q^2 dependent flux gave basically the same $F_2^{I\!P}$ values.

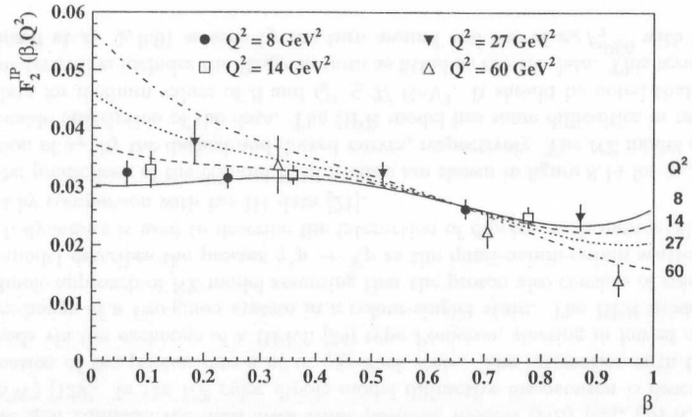

Figure 8.12: *The structure function $F_2^{I\!P}(\beta, Q^2)$ for the Q^2 values indicated, as a function of β as extracted from a fit to the measured $x_{I\!P} F_2^{D(3)}$ values, see text. The curves show the results obtained from the BEKW model, see section 8.5.4.*

The data show that the Pomeron structure function $F_2^{I\!P}$ has a simple behavior. For $\beta < 0.6$ and $Q^2 \leq 14$ GeV^2, $F_2^{I\!P}$ is approximately independent of β. For $\beta < 0.8$ also the data from different Q^2 values are rather similar suggesting a leading twist behavior characterized by a slow $\ln Q^2$ type rescaling. For $\beta > 0.9$ the data show a decrease with β or Q^2.

The approximate constancy of $F_2^{I\!P}$ for $\beta < 0.9$ combined with the rapid rise of $F_2^{D(3)}$ as $x_{I\!P}$ decreases can be interpreted as evidence for a substantial partonic component in DIS diffraction dissociation.

8.5.3 The Q^2 dependence of $x_{I\!P} F_2^{D(3)}$

The Q^2 behavior of $x_{I\!P} F_2^{D(3)}(x_{I\!P}, \beta, Q^2)$ is shown as solid points in figure 8.13. The data are presented for fixed M_X and W values, the variables in which the diffractive contribution was extracted. Given M_X, W and Q^2 the value of $x_{I\!P}$ can be calculated. From the figure it is seen, that for $M_X < 7.5$ GeV, $x_{I\!P} F_2^{D(3)}$ decreases with Q^2 while for $M_X = 11$ GeV it is approximately constant.

Strong Q^2 variations, which are found for the diffractive cross section are just a reflection of kinematics, see figure 8.4. The strong Q^2 variation of $d\sigma^D_{\gamma^* p}/dM_X$ is mainly given by the kinematical factor $M_X/(Q^2 + M_X^2)Q^2$ in Eq. 8.7.

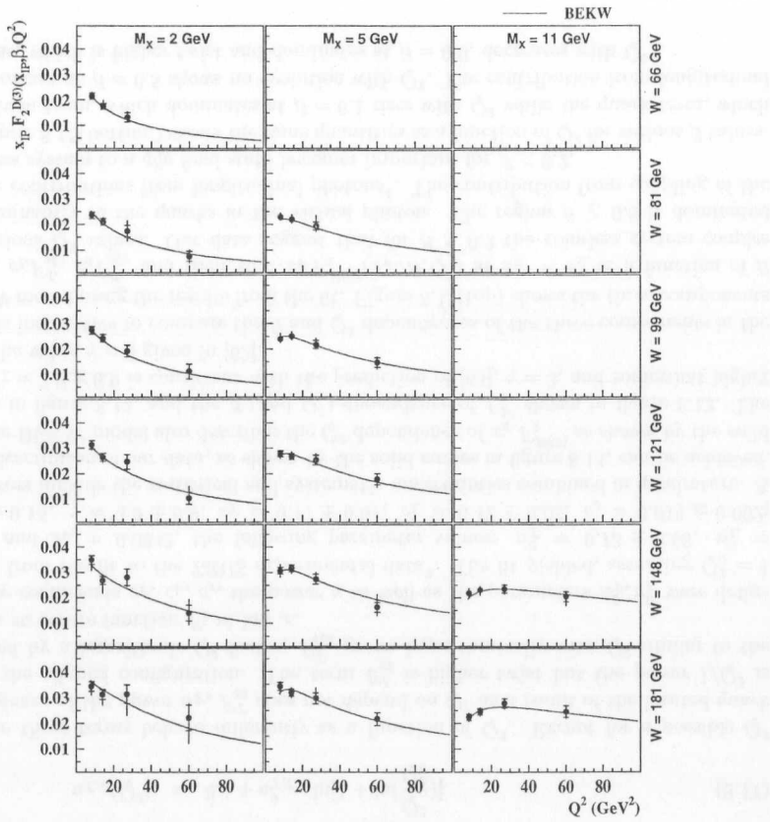

Figure 8.13: *The measured values of $x_{I\!P} \cdot F_2^{D(3)}$ (solid dots) as a function of Q^2. The values were scaled with 0.69, to account for double dissociation. The solid lines show the results obtained from the BEKW model, see section 8.5.4*

8.5.4 Comparison with Models

The diffractive process in DIS has attracted considerable attention because of the possibility that this process can be described by perturbative QCD. In [50] it was argued that the dominant contribution to diffraction in DIS comes from the aligned jet configuration. This contribution was expected to scale with Q^2. The β distribution for the aligned jet configuration from transverse photons was predicted [9] to be of the form

$$F_{q\bar{q}}^T \propto \beta(1-\beta). \tag{8.10}$$

The same β dependence was expected in pQCD when the aligned quarks interact with the proton via two-gluon exchange [62].

The production of a $q\bar{q}g$ system by transverse photons was also found to be leading twist and was assumed to have a β dependence of the type [62]

$$F_{q\bar{q}g}^T \propto (1-\beta)^\gamma \tag{8.11}$$

with $\gamma = 2$. A later calculation [63] found $\gamma = 3$. In the same approach the contribution to the production of a $q\bar{q}$ system by longitudinal photons was found to be of higher twist and to have a β dependence of the form

$$F_{q\bar{q}}^L \propto \beta^3(1-2\beta)^2. \tag{8.12}$$

In [68] the sum of the contributions from the three terms $F_{q\bar{q}}^T$, $F_{q\bar{q}}^L$, $F_{q\bar{q}g}^T$ was evaluated in the perturbative region.

We now compare the data with three partonic models (NZ) [62], (BPR) [65] and (BEKW) [129]. In the NZ color dipole model diffractive dissociation is described as a fluctuation of the photon into a $q\bar{q}$ or $q\bar{q}g$ Fock state. The interaction with the proton proceeds via the exchange of a BFKL [34] type Pomeron, starting in lowest order from the exchange of a two-gluon system in a colour-singlet state. The BPR model extends the dipole approach of NZ model assuming that the proton also consists of color dipoles. This model describes the process $\gamma^* p \to Xp$ as the quasi-onium-onium scattering. The BFKL dynamics is used to describe the interaction of dipoles, with numerical estimates tuned by comparison with the H1 data [21].

The predictions of the NZ and BPR models are shown in figure 8.14 for $x_{I\!P}\, F_2^{D(3)}$ as a function of $x_{I\!P}$ by the dashed and dotted curves, respectively. The NZ model provides a reasonable description of the data. The BPR model has some difficulties in reproducing the data for medium values of β and $Q^2 \leq 27$ GeV^2. It should be noted that the BPR parameterization includes the Reggeon term as fitted to the H1 data. This term becomes dominant at $x_{I\!P} \gtrsim 0.01$ as seen by the turn around and rise of $x_{I\!P}\, F_2^{D(3)}$ with increasing $x_{I\!P}$.

In the BEKW model [129] the individual contributions from the three terms in equations 8.10–8.12, were calculated in the perturbative region and extended into the soft region. The $x_{I\!P}\, F_2^{D(3)}$ dependence was assumed to be of the following form:

$$x_{I\!P}\, F_2^{D(3)}(\beta, x_{I\!P}, Q^2) = c_T \cdot F_{q\bar{q}}^T + c_L \cdot F_{q\bar{q}}^L + c_g \cdot F_{q\bar{q}g}^T \tag{8.13}$$

with

$$F_{q\bar{q}}^T = \left(\frac{x_0}{x_{I\!P}}\right)^{n_T(Q^2)} \cdot \beta(1-\beta) \tag{8.14}$$

$$F_{q\bar{q}}^L = \left(\frac{x_0}{x_{I\!P}}\right)^{n_L(Q^2)} \cdot \frac{Q_0^2}{Q^2} \cdot \left[\ln\left(\frac{7}{4} + \frac{Q^2}{4\beta Q_0^2}\right)\right]^2 \cdot \beta^3(1-2\beta)^2 \tag{8.15}$$

$$F_{q\bar{q}g}^T = \left(\frac{x_0}{x_{I\!P}}\right)^{n_T(Q^2)} \cdot \ln\left(1 + \frac{Q^2}{Q_0^2}\right) \cdot (1-\beta)^\gamma \tag{8.16}$$

$$n_{T,L}(Q^2) = 0.1 + n_{T,L}^0 \cdot \ln\left[1 + \ln\left(\frac{Q^2}{Q_0^2}\right)\right]. \tag{8.17}$$

The three terms behave differently as a function of Q^2. Except for a possible Q^2 dependence of the power n_T, $F_{q\bar{q}}^T$ does not depend on Q^2 as a result of the limited quark p_T in the aligned configuration. The term $F_{q\bar{q}}^L$ is higher twist but the power $1/Q^2$ is softened by a logarithmic Q^2 factor; $F_{q\bar{q}g}^T$ grows logarithmically with Q^2 similar to the proton structure function F_2 at low x.

The coefficients c_T, c_L, c_g, the power γ as well as the parameters n_T^0, n_L^0 were determined from the fit to the ZEUS experimental data[3]. The fit yielded, assuming $Q_0^2 = 1$ GeV^2 and $x_0 = 0.0042$, the following parameter values: $n_T^0 = 0.13 \pm 0.03$, $n_L^0 = 0.32 \pm 0.14$, $\gamma = 3.9 \pm 0.9$, $c_T = 0.11 \pm 0.01$, $c_L = 0.12 \pm 0.03$, $c_g = 0.014 \pm 0.002$; the errors include the statistical and systematic uncertainties combined in quadrature. A good description of our data, as shown by the solid curves in figure 8.14, can be achieved.

The BEKW model also describes the Q^2 dependence of $x_{I\!P}\, F_2^{D(3)}$ as shown by the solid curves in figure 8.13, and the β (and Q^2) dependence of $F_2^{I\!P}$ shown in figure 8.12. The value $\gamma = 3.9 \pm 0.9$ is consistent with the prediction of [63], $\gamma = 3$, and somewhat higher than the value $\gamma = 2$ given in [62].

It is instructive to compare the β and Q^2 dependences of the three components in the BEKW model using the results from the fit. Figure 8.15(top) shows the three components $c_T F_{q\bar{q}}^T$, $c_L F_{q\bar{q}}^L$, $c_g F_{q\bar{q}g}^T$ and their sum $x_{I\!P}\, F_2^{D(3)}(x_{I\!P}, \beta, Q^2)$ at $x_{I\!P} = x_0$ as a function of β for various Q^2 values. Our data suggest that for $\beta > 0.2$ the colorless system couples predominantly to the quarks in the virtual photon. The region $\beta \geq 0.8$ is dominated by the contributions from longitudinal photons[4]. The contribution from coupling of the colorless system to a $q\bar{q}g$ final state becomes important for $\beta < 0.2$.

Figure 8.15(bottom) shows the same quantities as a function of Q^2 for various β values. The gluon term, which dominates at $\beta = 0.1$ rises with Q^2 while the quark term, which is important at $\beta = 0.5$ shows no evolution with Q^2. The contribution from longitudinal photons, which is higher twist and dominates at $\beta = 0.9$, decreases with Q^2.

[3] The work done in this thesis has contributed to the nominal ZEUS analysis and the numerous contributions are indicated and acknowledged in [141]. In addition, the ZEUS nominal diffractive cross sections include as a systematic check the difference with the cross sections as obtained in this thesis. The differences were found to be typically less than 2% for most of the quoted diffractive cross sections.

[4] In determining the diffractive cross section and the diffractive structure function the R term in the Eq. 8.1 has been assumed to be zero. If this term is kept for $\beta > 0.8$ and the BEKW fit is repeated with the assumption $R = 1$ the changes in the fit parameters are small compared to their errors.

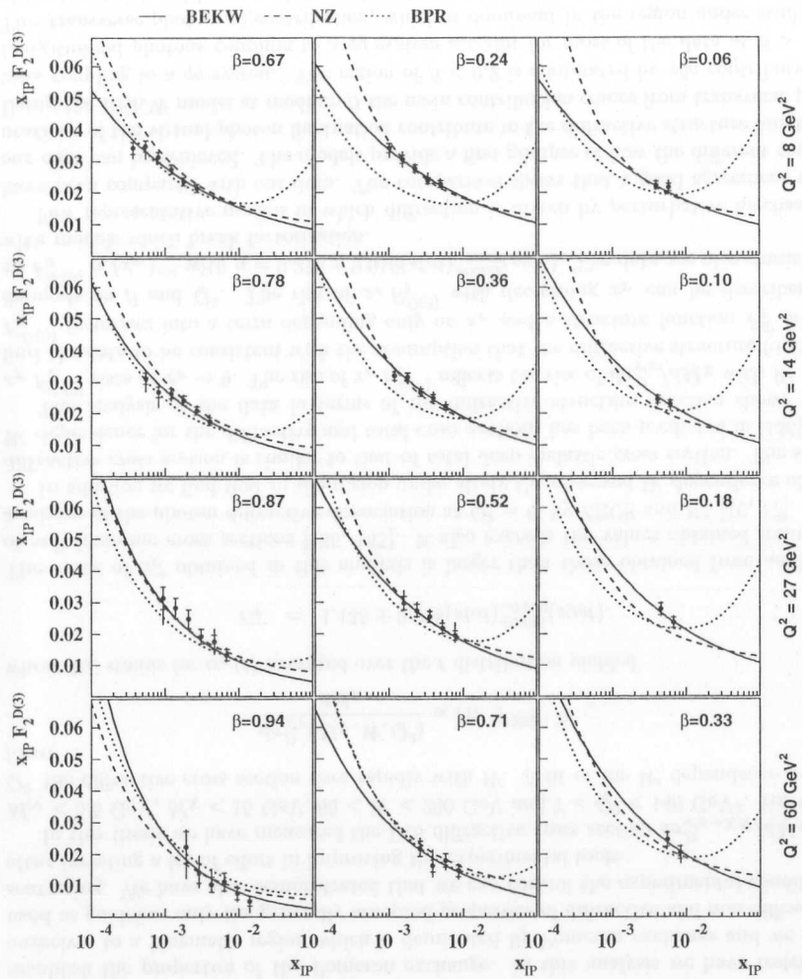

Figure 8.14: *The diffractive structure function of the proton multiplied by $x_{I\!P}$, $x_{I\!P} F_2^{D(3)}$, as a function of $x_{I\!P}$ from this analysis (solid points). The value of $F_2^{D(3)}$ from the M_X method was scaled with 0.69, to account for double dissociation. The inner error bars show the statistical errors and the full bars the statistical and systematic errors added in quadrature. The curves show the results from the models of Nikolaev and Zhakarov (NZ), Bialas, Peschanksi and Royon (BPR) and Bartels, Ellis, Kowalski and Wüsthoff (BEKW).*

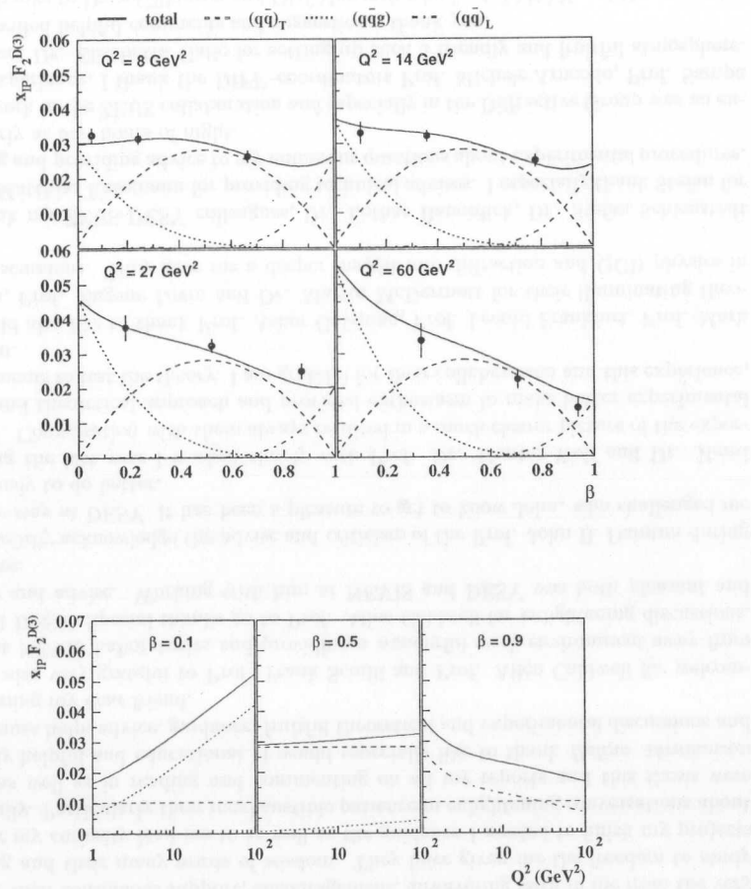

Figure 8.15: *Top) The three components $c_T F^T_{q\bar{q}}$, $c_L F^L_{q\bar{q}}$, $c_g F^T_{q\bar{q}g}$ and their sum $x_{I\!P} F_2^{D(3)}$ at $x_{I\!P} = x_0 = 0.0042$ as a function of β for Q^2 values indicated in the figure, as obtained from the BEKW model. Bottom) the same quantities as a function of Q^2 for β values as denoted in the figure.*

8.6 Summary and Conclusions

Since the discovery of Large Rapidity Gap events in DIS at HERA the experimentalists have been struggling to understand the properties and the origin of these events. The task is not simple as the environment of a collider experiments makes it very difficult to make measurements unbiased by MC simulation of the Deep Inelastic Physics. In addition, there is no strict definition of diffraction while the purpose of studying diffraction is to establish the properties of the Pomeron exchange. In this analysis we have restricted ourselves to a kinematic region which is dominated by Pomeron exchange and we have used as guideline only the generally accepted properties of diffractive and non-diffractive scattering. We have also demonstrated that we can control the experimental conditions after investing a lot of effort in improving the experimental tools.

In this thesis we have measured the DIS diffractive cross section $d\sigma^D_{\gamma^* p \to XN}/dM_X$ for $M_N < 5.5$ GeV, $M_X < 15$ GeV, $60 < W < 200$ GeV and $7 < Q^2 < 140$ GeV^2. For fixed Q^2 the diffractive cross section rises rapidly with W. A fit of the W dependence to the form

$$\frac{d\sigma^D_{\gamma^* p}(M_X, W, Q^2)}{dM_X} \propto (W^2)^{(2\overline{\alpha_{I\!P}}-2)} \quad ,$$

where $\overline{\alpha_{I\!P}}$ stands for $\alpha_{I\!P}(t)$ averaged over the t distribution yielded

$$\overline{\alpha_{I\!P}} \;=\; 1.135 \pm 0.008(stat)^{+0.011}_{-0.030}(syst).$$

The value of $\overline{\alpha_{I\!P}}$ obtained in this analysis is larger than those obtained from analyses of soft hadronic cross sections [136, 135]. It also exceeds the values obtained from the analyses of the photon diffractive dissociation at $Q^2 = 0$, by ZEUS and H1 [16, 17].

In addition we find that in the region under study the observed W dependence of the diffractive cross section is similar to that of total deep inelastic cross section. The same W dependence for the diffractive and total cross sections has been predicted in [138].

The analysis of the data in terms of the diffractive structure function shows that $x_{I\!P}\, F_2^{D(3)}$ rises as $x_{I\!P} \to 0$. The rise of $x_{I\!P}\, F_2^{D(3)}$ reflects the rise of $d\sigma^D_{\gamma^* p}/dM_X$ with W. We find the data to be consistent with the assumption that the diffractive structure function $F_2^{D(3)}$ factorizes into a term depending only on $x_{I\!P}$ and a structure function $F_2^{I\!P}$ which depends on β and Q^2. The rise of $x_{I\!P}\, F_2^{D(3)}$ with decreasing $x_{I\!P}$ can be described as $x_{I\!P}\, F_2^{D(3)} \propto (x_{I\!P})^{-n}$ with $n = 0.270 \pm 0.016(stat)^{+0.022}_{-0.060}(syst)$. The data are also consistent with models which break factorization.

Few representative models in which diffraction is driven by perturbative mechanism have been compared with our data. The comparison shows that a good agreement with our data can be achieved. The models provide a first glimpse of how the different configurations of the virtual-photon fluctuation contribute to the diffractive structure function. Using the BEKW model at medium β the main contribution comes from transverse photons coupling to a $q\bar{q}$ system. The region of $\beta < 0.2$ is dominated by $q\bar{q}g$ contributions. Longitudinal photons coupling to a $q\bar{q}$ system account for most of the data at $\beta > 0.8$. The transverse photon $q\bar{q}$ contribution, which is dominant in the region under study, is of leading twist and has no substantial evolution with Q^2.

The leading twist behavior and the strong rise of $x_{I\!P}\, F_2^{D(3)}$ as $x_{I\!P} \to 0$ suggest a partonic process as a major production mechanism for diffractive scattering in DIS.

Acknowledgments

Quite a number of people helped me and gave me guidance during my Ph.D. studies. I would like to take this opportunity to thank all of them.

First of all I am grateful to my supervisors Prof. Halina Abramowicz and Prof. Aharon Levy, for their continuous support, encouragement, unwavering faith in me from the very beginning and their many words of wisdom. They have given me the freedom to study whatever my curiosity lead me to as well as the guidance I needed to finish my projects successfully. Particularly their inexhaustible patience in enlightening conversations about physics as well as in reading and commenting on all my reports and this thesis were extremely helpful and educational. I would especially like to thank *Halina Abramowicz* for continues help, advice, guidance, fruitful theoretical and experimental discussions and for becoming my dear friend.

I am also very grateful to Prof. Frank Sciulli and Prof. Allen Caldwell for welcoming me at NEVIS Laboratories and providing a wonderful work environment away from TAU and DESY. Special thanks go to Prof. Allen Caldwell for enlightening discussions, guidance and advise. Working with him at NEVIS and DESY was both pleasant and instructive.

I gratefully acknowledge the advise and criticism of the Prof. John B. Dainton during my entire stay at DESY. It has been a pleasure to get to know John, who challenged me continuously to do better.

During the last year I worked closely with Prof. Dr. Gunter Wolf and Dr. Henri Kowalski. Conversation with them always resulted in a much clearer picture of the experimental and theoretical approach and provided enthusiasm to make better experimental measurements to test the theory. I am grateful for their collaboration and this experience, thank you.

I would also like to thank Prof. Asher Gotsman, Prof. Leonid Frankfurt, Prof. Mark Strikman, Prof. Eugene Levin and Dr. Martin McDermott for their illuminating theoretical discussions. They gave me a deeper insight into diffraction and QCD physics in general.

I thank my ZEUS-DESY colleagues, Dr. Lothar Bauerdick, Dr. Stefan Schlenstedt and Dr. Matthias Kasemann for providing technical advises. I especially thank Stefan for answering and providing advice to my numerous questions about experimental procedures, particularly at odd hours of night.

The work in the ZEUS collaboration and especially in the Diffractive Group was an enjoyable experience. I thank the DIFF–coordinators Prof. Michele Arneodo, Prof. Sampa Bhadra and Dr. Elisabetta Gallo for setting up such a friendly and fruitful atmosphere. They provided helpful comments and suggestions, thank you.

It is thanks to Dave Gilkinson and Olaf Manczak who kept ZARAH and the computer cluster up and running, that I could torture these machines with my CPU intensive jobs and carry out my analysis.

It is a pleasure to acknowledge the warm friendship and support of several graduate students and postdocs at Tel Aviv University and DESY; Alon Marcus, Carmit Sahar, Dr. Alexandros Prinias, Dr. Costas Foudas, Dr. Bruce Straub and Dr. John Ryan. I thank them for their companionship and for the countless dinners and cups of coffee we shared.

I want to specially thank Dr. Ralph Sinkus for welcoming me in Hamburg, for his companionship and for the countless discussions we shared about physics and life in general. During my stay at DESY we became very good friends.

That I did not get completely lost at DESY, Hamburg but also enjoyed life outside is thanks to the friendship of Josephine Zilberkweit.

This work was partly supported by the German-Israel Foundation (GIF) and the Israel Science Foundation (ISF). I would like to thank the MINERVA Foundation and the DESY Laboratory for funding my stay at DESY during the last two years of my Ph.D.

Finally, I would like to thank my parents and grandparents who have always been patient, loving, caring and understanding. They have always supported and encouraged me to make the most out of opportunities they never had. I also want to express my gratitude to *Lisa Bryna Briskin*, my wife and best friend, for her love and understanding throughout this arduous portion of our life. This thesis and work towards it would not have been possible without them and their support.

THANK YOU !!!

Appendix A

Resolutions and Migrations

The plots showing resolution and migration of kinematic variables, as well as the acceptance and purity of the bins, are presented in figures A.1 - A.7. The arrows indicate the average migration from generated to reconstructed values within a bin. The thick error bars show the detector resolution for bin j which are obtained from the Gaussian fit. The thin error bars represent the r.m.s. values. The purity (upper) and acceptance (lower) values in the bin are shown in %.

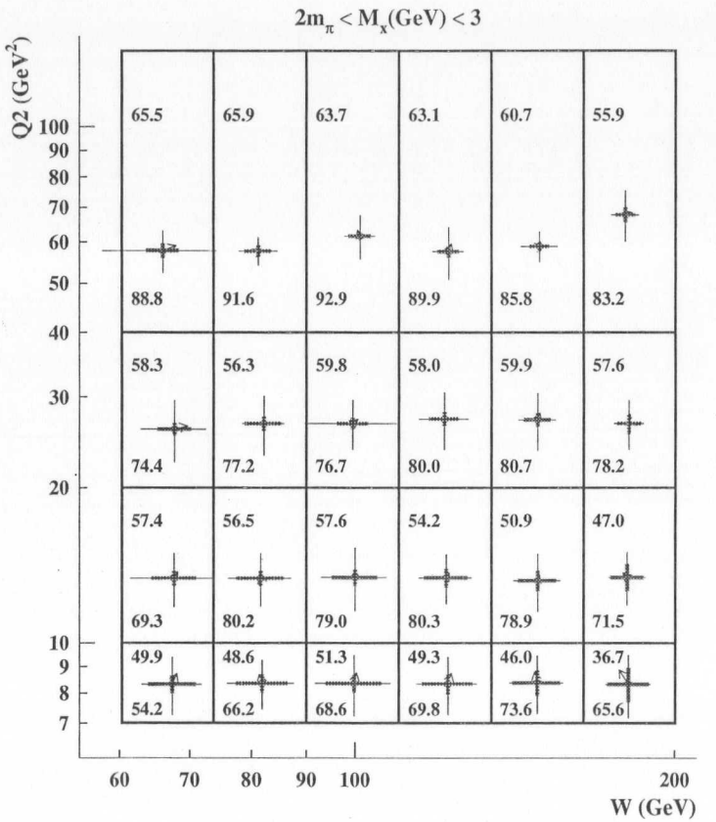

Figure A.1: *W and Q^2 resolutions and migrations for $2m_\pi < M_X < 3$ GeV. The arrows indicate the average migration from generated to reconstructed values within a bin. The thick error bars show the detector resolution for bin j which are obtained from the Gaussian fit. The thin error bars represent the r.m.s. values. The purity (upper) and acceptance (lower) values are in % for the selected bins.*

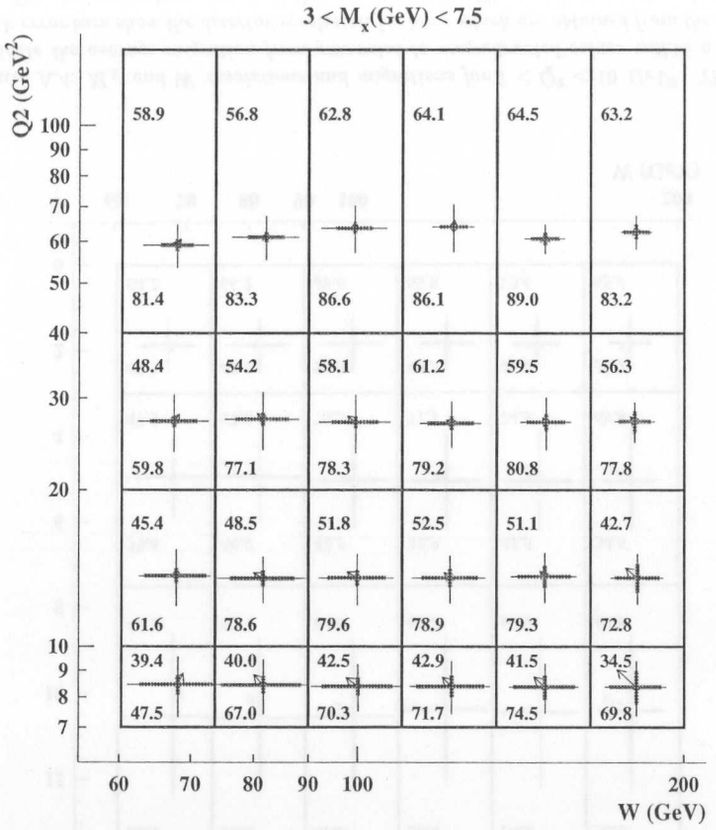

Figure A.2: *W and Q^2 resolutions and migrations for $3 < M_X < 7.5$ GeV. The arrows indicate the average migration from generated to reconstructed values within a bin. The thick error bars show the detector resolution for bin j which are obtained from the Gaussian fit. The thin error bars represent the r.m.s. values. The purity (upper) and acceptance (lower) values are in % for the selected bins.*

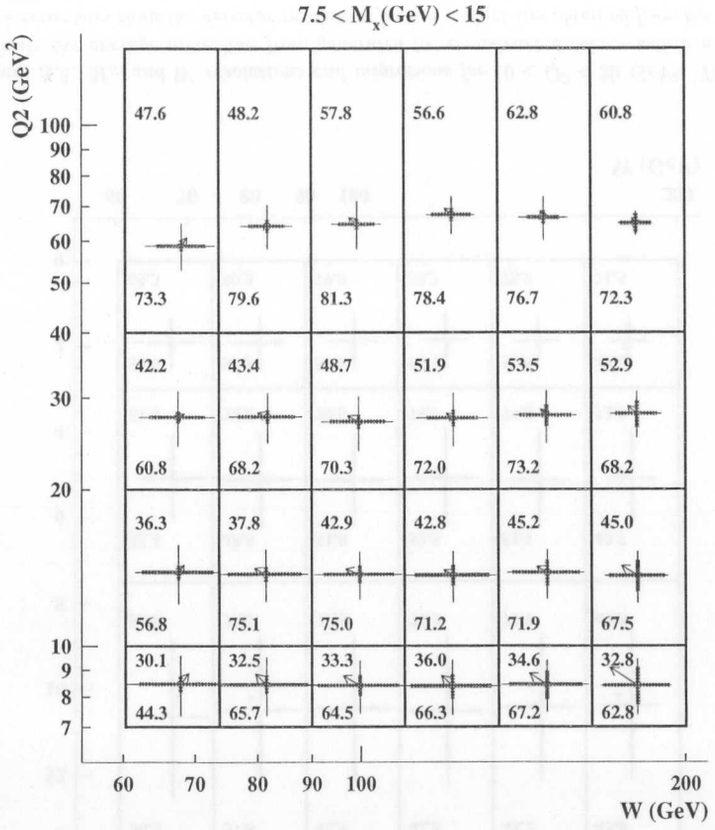

Figure A.3: *W and Q^2 resolutions and migrations for $7.5 < M_X < 15$ GeV. The arrows indicate the average migration from generated to reconstructed values within a bin. The thick error bars show the detector resolution for bin j which are obtained from the Gaussian fit. The thin error bars represent the r.m.s. values. The purity (upper) and acceptance (lower) values are in % for the selected bins.*

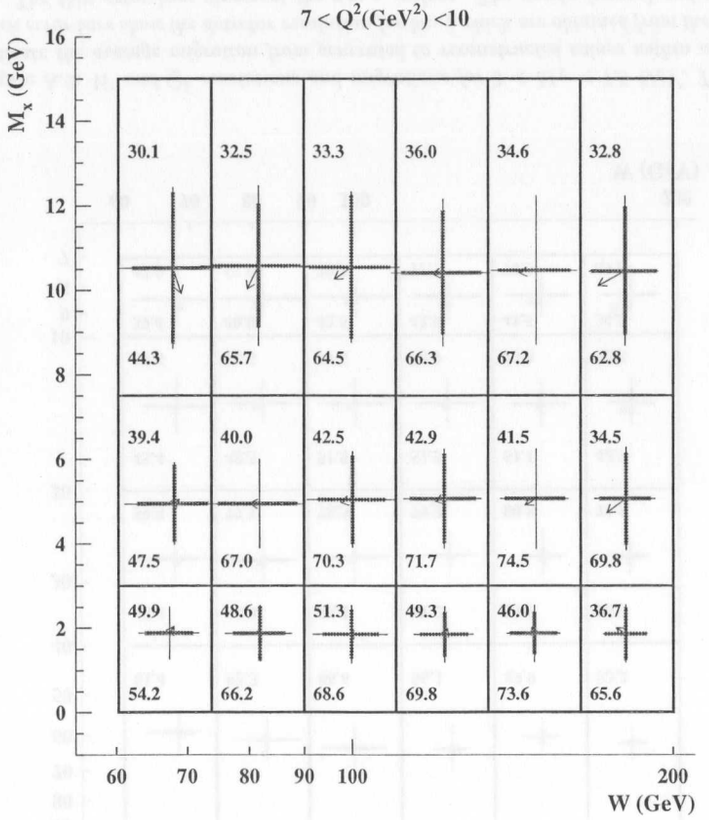

Figure A.4: *M_X and W resolutions and migrations for $7 < Q^2 < 10$ GeV^2. The arrows indicate the average migration from generated to reconstructed values within a bin. The thick error bars show the detector resolution for bin j which are obtained from the Gaussian fit. The thin error bars represent the r.m.s. values. The purity (upper) and acceptance (lower) values are in % for the selected bins.*

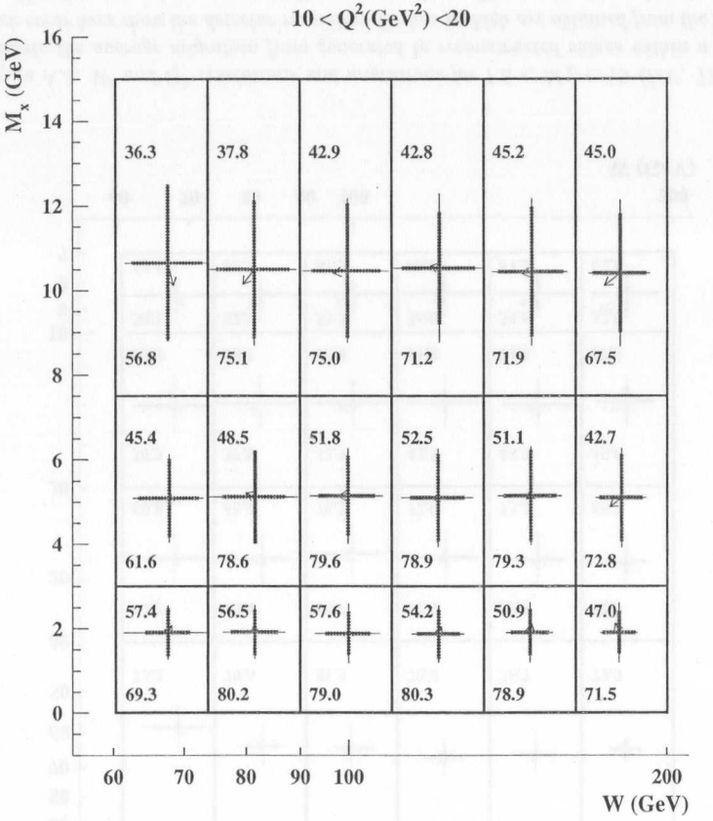

Figure A.5: *M_X and W resolutions and migrations for $10 < Q^2 < 20$ GeV^2. The arrows indicate the average migration from generated to reconstructed values within a bin. The thick error bars show the detector resolution for bin j which are obtained from the Gaussian fit. The thin error bars represent the r.m.s. values. The purity (upper) and acceptance (lower) values are in % for the selected bins.*

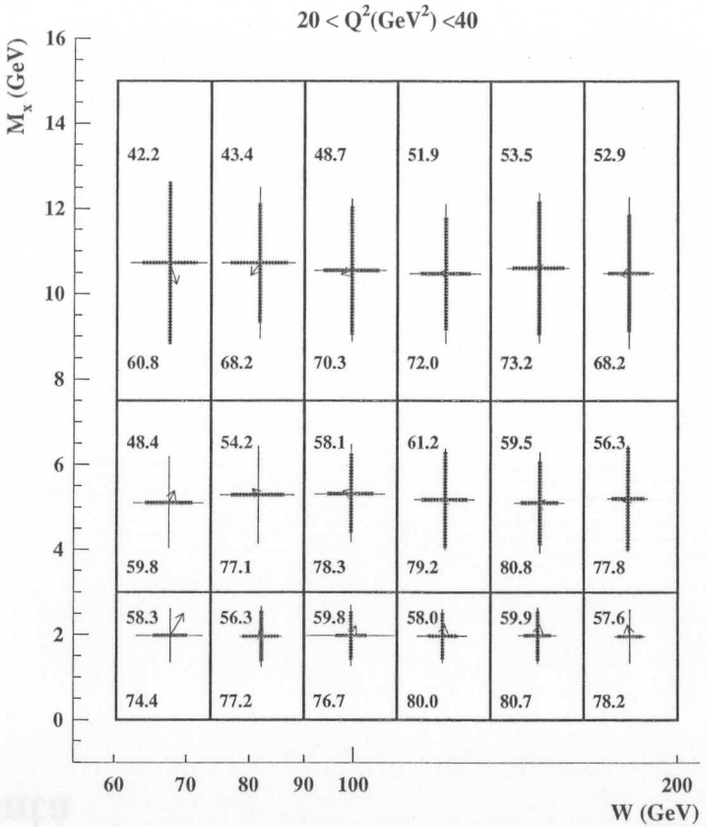

Figure A.6: *M_X and W resolutions and migrations for $20 < Q^2 < 40$ GeV^2. The arrows indicate the average migration from generated to reconstructed values within a bin. The thick error bars show the detector resolution for bin j which are obtained from the Gaussian fit. The thin error bars represent the r.m.s. values. The purity (upper) and acceptance (lower) values are in % for the selected bins.*

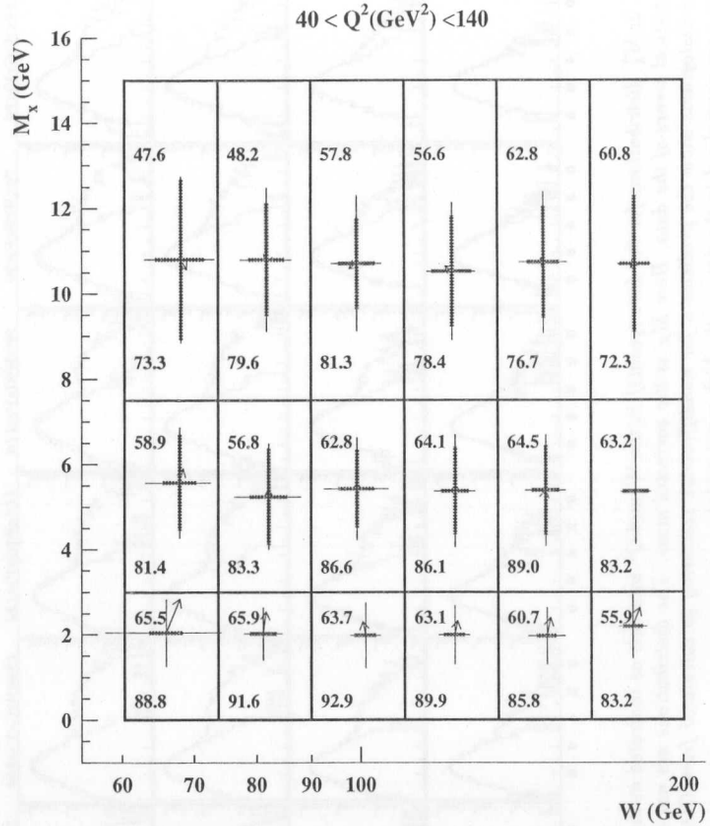

Figure A.7: *M_X and W resolutions and migrations for $40 < Q^2 < 140$ GeV^2. The arrows indicate the average migration from generated to reconstructed values within a bin. The thick error bars show the detector resolution for bin j which are obtained from the Gaussian fit. The thin error bars represent the r.m.s. values. The purity (upper) and acceptance (lower) values are in % for the selected bins.*

Appendix B

Comparison of MC simulation with data

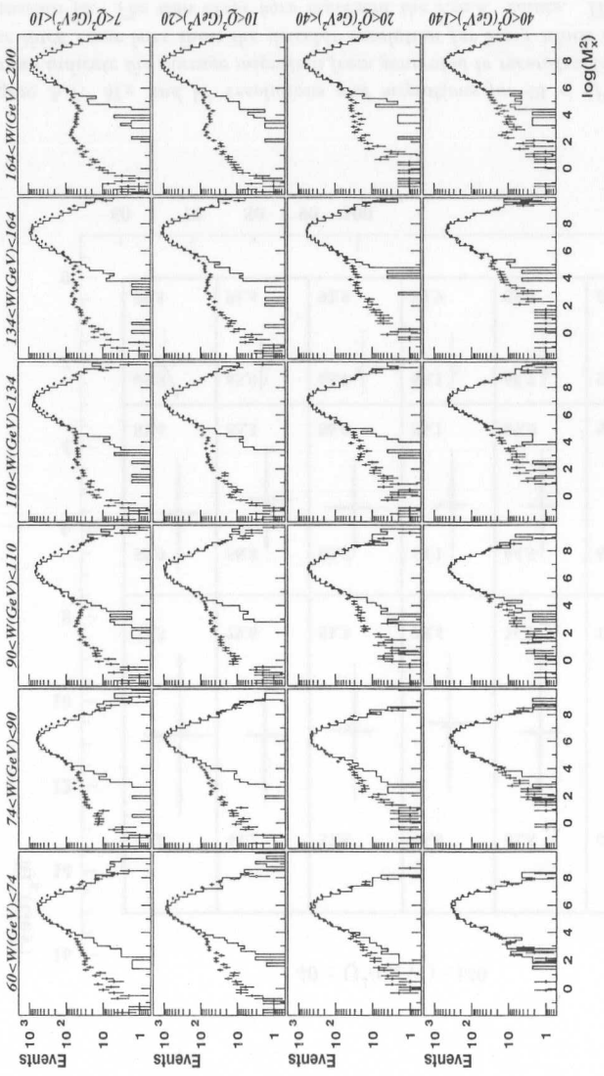

Figure B.1: $\ln M_X^2$ *distributions for the data (points) in the* W *and* Q^2 *intervals as indicated in the figure. The error bars give the statistical errors of the data. Here* M_X *is the corrected mass. The distributions are not corrected for acceptance effects. The histograms show the predictions for nondiffractive scattering as calculated from CDMBGF. The CDMBGF distributions were normalized to the data in the high mass region.*

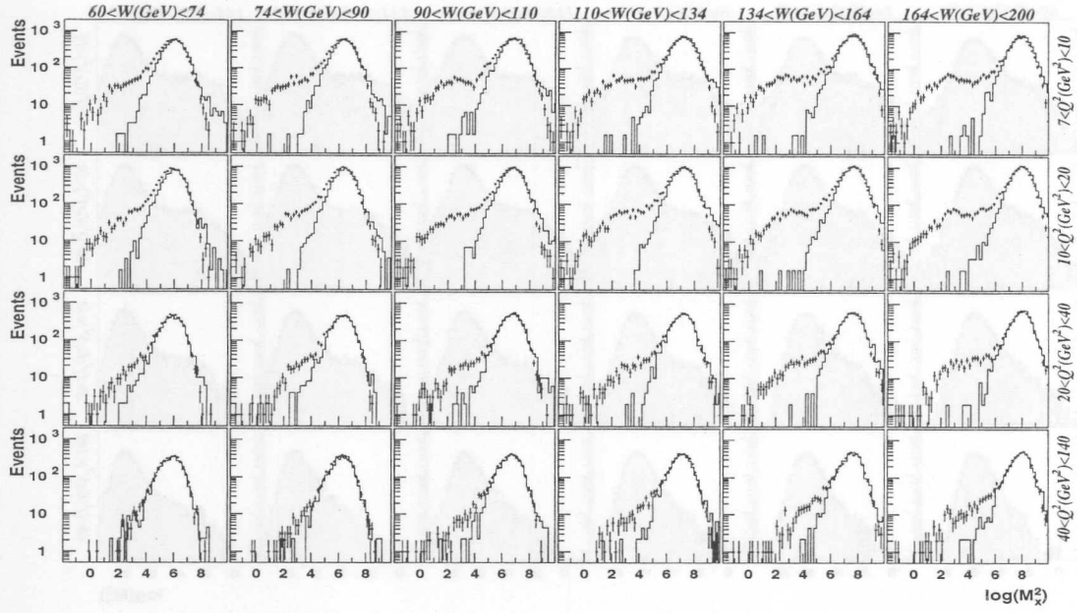

Figure B.2: $\ln M_X^2$ *distributions for the data (points) in the* W *and* Q^2 *intervals as indicated in the figure. The error bars give the statistical errors of the data. Here* M_X *is the corrected mass. The distributions are not corrected for acceptance effects. The histograms show the predictions for nondiffractive scattering as calculated from CDMBGF shifted upwards by 0.4 (0.35. 0.2, 0.1) units in* $\ln M_X^2$ *at* $Q^2 = 7(10, 27, 60)$ *GeV*^{2} *(see text). The CDMBGF distributions were normalized to the data in the high mass region.*

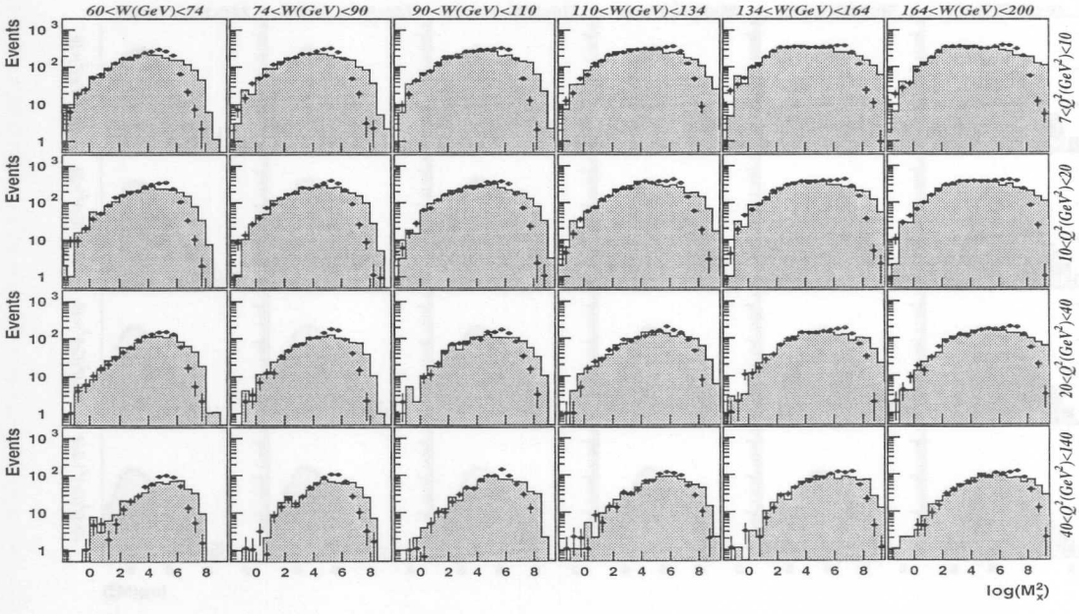

Figure B.3: *Distribution of* $\ln M_X^2$ *predicted for the diffractive contribution by RAPGAP (HJP1) at the generator (histograms) and detector (dots) levels for the* W *and* Q^2 *intervals as indicated in the figure.*

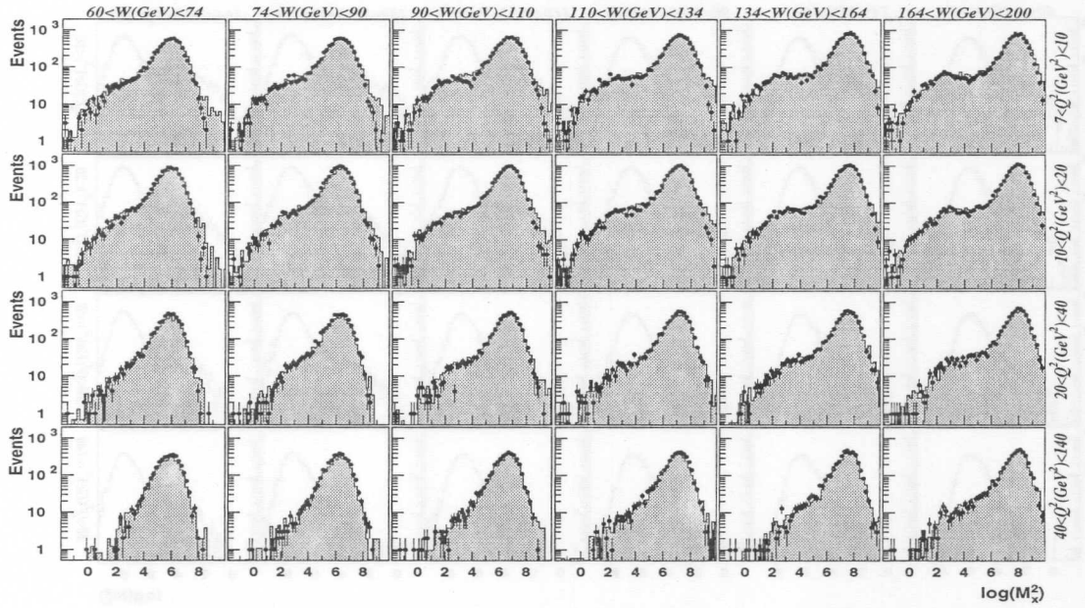

Figure B.4: *Distributions of* $\ln M_X^2$ *determined from the data (points) for the* W *and* Q^2 *intervals as indicated. The error bars give the statistical errors of the data. Here* M_X *is the corrected mass. The distributions are not corrected for acceptance effects. The histograms show the predictions for the sum of the contributions from nondiffractive scattering as calculated from CDMBGF (shifted upwards in* $\ln M_X^2$ *as explained in the text) and from diffractive scattering as calculated from RAPGAP (HJP1). The DIS and DIFF components were normalized to give the best description of data.*

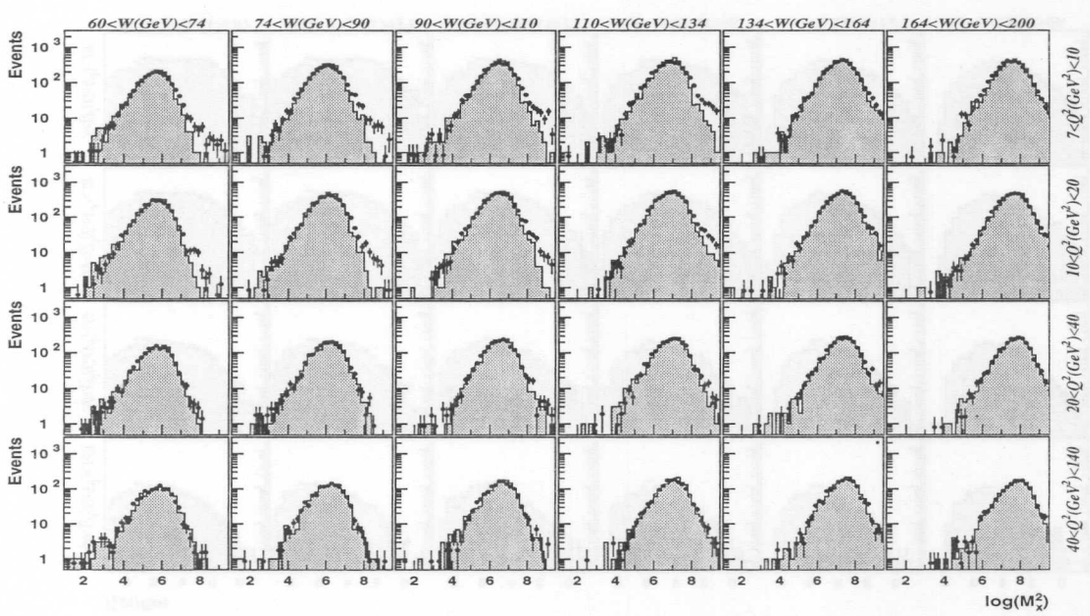

Figure B.5: *Distributions of* $\ln M_X^2$ *as predicted by CDMBGF MC model at the generator (histograms) and detector (dots) levels for the* W *intervals and* Q^2 *values indicated.*

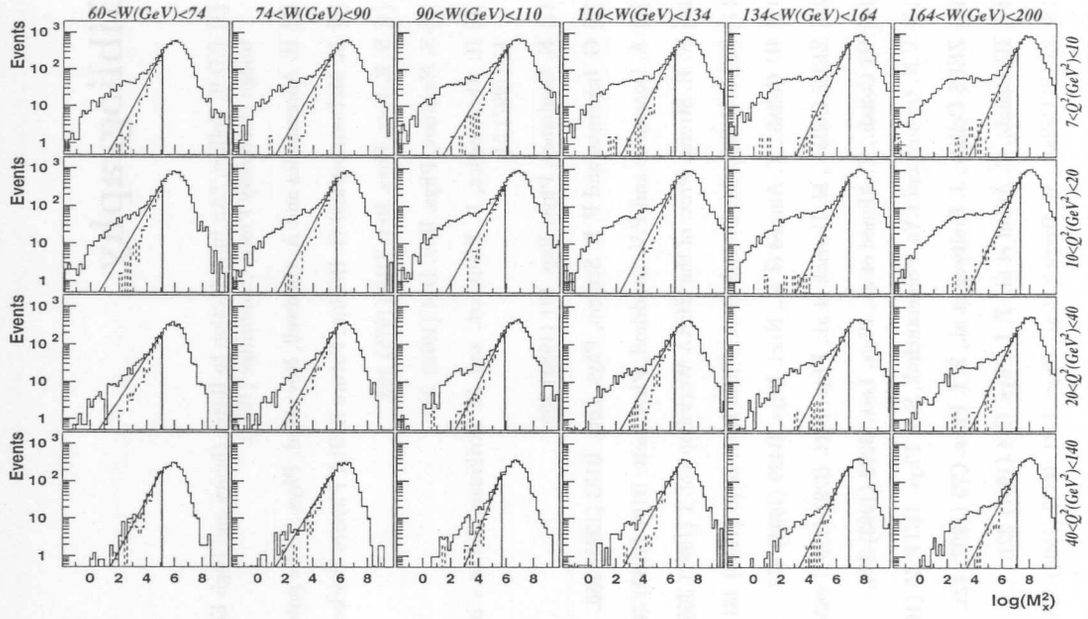

Figure B.6: *Example of standard fit to DIS+DIFF MC sample. The solid histograms show the predictions for the sum of the contributions from nondiffractive scattering as calculated from CDMBGF and from diffractive scattering as calculated from RAPGAP (HJP1). The DIS and DIFF components were normalized to give the best description of data. The dashed histograms show the predictions for the contributions from nondiffractive scattering as calculated from CDMBGF. The thick solid vertical lines indicate the maximum* $\ln M_X^2$ *values up to which the fits were performed. The thin solid lines show the results from the fits for the nondiffractive contribution.*

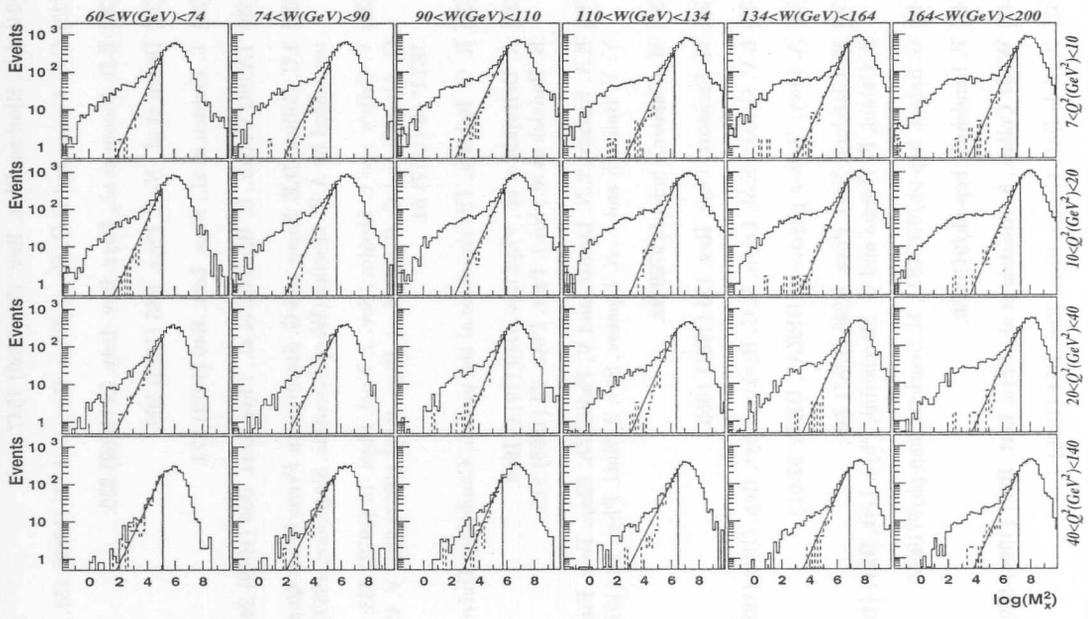

Figure B.7: *Example of extended fit to DIS+DIFF MC sample. The solid histograms show the predictions for the sum of the contributions from nondiffractive scattering as calculated from CDMBGF and from diffractive scattering as calculated from RAPGAP (HJP1). The DIS and DIFF components were normalized to give the best description of data. The dashed histograms show the predictions for the contributions from nondiffractive scattering as calculated from CDMBGF. The thick solid vertical lines indicate the maximum* $\ln M_X^2$ *values up to which the fits were performed. The thin solid lines show the results from the fits for the nondiffractive contribution.*

Bibliography

[1] P.D.B. Collins, "An Introduction to Regge theory and High Energy Physics", Cambridge University Press, Cambridge (1977).

[2] H. Abramowicz and A. Caldwell, Rev. Mod. Phys., to be published.

[3] M. McDermott and G. Briskin, Future HERA Physics Workshop, 1997.

[4] S. E. Low, Phys. Rev. D12 (1975) 163.

[5] S. Nussinov, Phys. Rev. D14 (1976) 246.

[6] H. Abramowicz, L. Frankfurt, and M. Strikman, Surveys in High Energy Phys. 11 (1997) 51.

[7] K. Goulianos, Phys. Rep. 101 (1983) 169.

[8] G. Ingelman and P. E. Schlein, Phys. Lett. B152 (1985) 256.

[9] A. Donnachie and P.V. Landshoff, Phys. Lett. B191 (1987) 309.

[10] K. H. Streng, Proc. of the HERA Workshop vol. 1 (1987) 365, ed. R.D. Peccei

[11] ZEUS Collab., M. Derrick et al., Phys. Lett. B315 (1993) 481.

[12] H1 Collab., T. Ahmed et al., Nucl. Phys. B429 (1994) 477.

[13] ZEUS Collab., M. Derrick et al., Phys. Lett. B293 (1992) 465.

[14] H1 Collab., T. Ahmed et al., Phys. Lett. B299 (1993) 374.

[15] V.N. Gribov and I.Ya. Pomeranchuk, Sov. Phys. JETP 15 (1962) 788.

[16] ZEUS Collab., J. Breitweg et al., Z. f. Phys. C75 (1997) 421.

[17] H1 Collab., C. Adloff et al., Z. f. Phys. C74 (1997) 221.

[18] ZEUS Collab., M. Derrick et al., Phys. Lett. B332 (1994) 228.

[19] ZEUS Collab., M. Derrick et al., Z. Phys. C70 (1996) 391.

[20] H1 Collab., T. Ahmed et al., Phys. Lett. B348 (1995) 681.

[21] H1 Collab., C. Adloff et al., Z. Phys. C76 (1997) 613.

[22] L.N. Hand, Phys. Rev. 129 (1963) 1834.

[23] R.P. Feynman, Phys. Rev. Lett. 23 (1969) 1415.

[24] J.D. Bjorken, Phys. Rev. 179 (1969) 1547.

[25] C.G. Callan and D.G. Gross, Phys. Rev. Lett. 22 (1969) 156.

[26] E.D. Bloom et al., Phys. Rev. Lett. 23 (1969) 930.

[27] Deden et al., Nucl. Phys. B85 (1975) 269.

[28] T. Eichten et al., Phys. Lett. B46 (1973) 274.

[29] TASSO Collab., R. Bradelik et al., Phys. Lett. B86 (1979) 243.

[30] J.C. Collins, D.E. Soper and G. Sterman, in *Perturbative Quantum Chromodynamics*, edited by A.H. Mueller (Word Scientific, Singapore, 1989).

[31] V. Gribov and L. Lipatov, Sov. J. Nucl. Phys. 15 (1972) 438;
G. Altarelli and G. Parisi, Nucl. Phys. B126 (1977) 298; Y. Dokshitzer, Sov. Phys. JETP 46 (1977) 64.

[32] R. G. Roberts, The structure of the proton, Cambridge University Press, 1990.

[33] A. DeRujula et al., Phys.Rev. D10 (1974) 1649;
B. Badelek et al., Nucl. Part. Phys. 22 (1996) 815.

[34] E.A. Kuraev, L.N. Lipatov and V. Fadin, Zh. Eksp. Teor. Fiz. 72 (1977) 373;
Y. Y. Balitskij and L. N. Lipatov, Sov. J. Nucl. Phys. 28 (1979) 882.

[35] M. Ciafaloni, hep-ph/9709390.

[36] M. Froissart, Phys. Rev. 123 (1961) 1053.

[37] L.V. Gribov, E.M. Levin, M.G. Ryskin, Phys. Rep. C100 (1983) 1.

[38] A. Levy, "Low-x physics at HERA", DESY 97-013.

[39] M. Ciafaloni, Nucl. Phys. B296 (1987) 249;
S. Catani, F. Fiorani and G. Marchesini, Phys. Lett. B234 (1990) 339.

[40] G. Salam, hep-ph/9707382 ; M. Scorletti, hep-ph/9710559.

[41] P. Landshoff, hep-ph/9410250.

[42] WA91 Collab., S. Albatzis et al., Phys. Lett. B321 (1994) 509.

[43] Particle Data Group, Phys. Rev. D54 (1996) 1.

[44] A. Donnachie and P. V. Landshoff, Phys. Lett. B296 (1992) 227.

[45] S. Levonian, hep-ph/9612206.

[46] A.H. Mueller, Phys. Rev. D2 (1970) 2963.

[47] T.H. Bauer et al., Rev. Mod. Phys. 50 (1978) 261.

[48] ZEUS Collab., J. Breitweg et al., hep-ex/9712019.

[49] T.J. Chapin et al., Phys. Rev. D31 (1985) 17.

[50] J.D. Bjorken and J.B. Kogut, Phys. Rev. D8 (1973) 1341.

[51] A.H. Mueller and B. Patel, Nucl. Phys. B425 (1994) 471.

[52] S.J. Brodsky et al., Phys. Rev. D50 (1994) 3134.

[53] J.C. Collins, hep-ph/9709499.

[54] E.L. Berger, J.C. Collins, D.E. Soper and G. Sterman, Nucl. Phys. B286 (1987) 704.

[55] K. Golec-Biernat and J. Kwiecinski, Phys. Lett. B353 (1995) 329.

[56] A. Capella et al., Z. Phys. C65 (1995) 657.

[57] B.A. Kniehl, H.G. Kohrs and G. Kramer, Z. Phys. C65 (1995) 657.

[58] H. Kohrs, hep-ph/9512372.

[59] T. Gehrmann and W. Stirling, Z. Phys. C70 (1996) 89.

[60] J. Vermaseren, F. Barreiro, L. Labarga and F.J. Yndurain, hep-ph/9611444.

[61] ZEUS Collab., M. Derrick et al., Z. Phys. C68 (1995) 569.

[62] N.N. Nikolaev and B.G. Zakharov. Z. Phys. C53 (1992) 331; M. Genovese, N.N. Nikolaev and B.G. Zakharov, JETP 81 (1995) 625.

[63] M. Wüsthoff, PhD thesis, University of Hamburg and hep-ph/9706407.

[64] N.N. Nikolaev and B.G. Zakharov, Phys. Lett. B327 (1994) 149.

[65] A. Białas, R. Peschanski and Ch. Royon, hep-ph/9712216 (1997).

[66] M.G. Ryskin, Sov. J. Nucl. Phys. 52 (1990) 529.

[67] J. Bartels and M. Wüsthoff, Nucl. Part. Phys. 22 (1996) 929.

[68] E. Gotsman, E. Levin and U. Maor, Nucl. Phys. B493 (1997) 354.

[69] W. Buchmüller and A. Hebecker, hep-ph/9512329.

[70] W. Buchmüller, M. F. McDermott, and A. Hebecker, hep-ph/9607290.

[71] W. Buchmüller and A. Hebecker, Phys. Lett. B355 (1995) 573.

[72] A. Blondel and F. Jacquet, DESY 79-48.

[73] S. Bentvelsen, J. Engelen and P. Kooijman, Proc. Workshop *Physics at HERA*, ed. W. Buchmüller and G. Ingelman, DESY 1992, Vol. 1,23.

[74] ZEUS Collab., The ZEUS Detector, Technical Proposal 1986.

[75] ZEUS Collab., The ZEUS Detector, Status Report 1993.

[76] B. Foster et al., Nucl. Instr. Meth. A338(1994)254.

[77] M. Derrick et al., Nucl. Instr. Meth. A309(1991)77

[78] A. Bamberger et al., ZEUS-Note 95-095.

[79] H. Bethe and W. Heitler, Proc. Roy. Soc. A146(1934)83.

[80] K. Piotrzkowski, Dissertation, DESY F35D-93-06.

[81] C. Youngman, 'The ZEUS Data Acquisition System', DESY 92-150A.

[82] W.H. Smith et al., ZEUS-Note 89-084.

[83] H. Uijterwaal, Ph.D. Thesis, University of Amsterdam 1992.

[84] U. Behrens et al., Nucl. Instr. Meth. A336 (1993) 23.

[85] H. Spiesberger et al., DJANGO6 Monte Carlo Event Generator.

[86] H. Spiesberger, see WWW page – http://www.desy.de/~hspiesb/heracles.html

[87] G. Ingelman et al., LEPTO6.5 Monte Carlo Event Generator.

[88] L. Lnnblad, Ariadne program and manual, Comput.Phys.Commun. 71 (1992) 15.

[89] T. Sjöstrand. Comput. Phys. Commun. 82 (1994).

[90] Y. Azimov, Y. Dokshitzer, V. Khoze, S. Troyan, Phys. Lett. B165 (1985) 147.

[91] B. Anderson et. al., Phys. Rev. 97 (1983) 31.

[92] ZEUS Collab., M. Derrick et al., Z. Phys. C59 (1993) 231.

[93] A.D. Martine, W.J. Stirling and R.G. Roberts, Phys. Rev. D51 (1994) 4756.

[94] RAPGAP 2.3, H. Jung, Manual in preparation.

[95] ZEUS Collab., M.Derrick et al., Z. Phys. C68 (1995) 569.

[96] POMPYT, G. Ingelman et. al., Monte Carlo Event Generator.

[97] PYTHIA/JETSET manual by T. Sjöstrand.

[98] GEANT 3.13: R. Brun et. al., CERN DD/EE/84-1 (1987).

[99] ZGANA, ZEUS trigger simulation library.

[100] F.S. Chlebana, Ph.D. Thesis, University of Toronto (1993).

[101] W.H. Smith et al., Nucl. Instr. Meth. A355(1995)278.

[102] LOCAL electron finder, ZEUS user library.

[103] Elec5 electron finder, ZEUS user library.

[104] G.F. Hartner et al., ZEUS-Note 96-013.

[105] J. Krüger, DESY F35-92-02.

[106] G.A. Akopjanov et al., Nucl. Instr. and Meth. 140(1977)441.

[107] T.C. Awes et al., Nucl. Instr. and Meth. A311(1977)130.

[108] H.Beier, Ph.D. Thesis, University of Hamburg (1997).

[109] R. Sinkus, Nucl. Instr. and Meth. A361(1995)290.

[110] R. Sinkus and T.Voss, Nucl. Instr. and Meth. A391(1997)360.

[111] L.L. Wai, Ph.D. Thesis, Columbia University (1995).

[112] T. Doeker, A. Frey and M. Nakao, ZEUS-Note 94-123.

[113] J. Ng and W. Verkerke, ZEUS-Note 95-037.

[114] ZEUS Collab., M.Derrick et al., Z. Phys. C69 (1996) 607.

[115] A. Quadt, Ph.D. Thesis, University of Oxford, 1996.

[116] R. Sinkus, Ph.D. Thesis, University of Hamburg, 1996.

[117] G. Briskin and A. Caldwell, ZEUS-Note 95-035.

[118] Bin Lu, presentation at the ZEUS DIS meeting.

[119] C. Amelung, Diploma Thesis, Bonn, 1996.

[120] H. Abramowicz and A. Caldwell, Private communication.

[121] A. Prinias, Ph.D. Thesis, University of London, 1995.

[122] ZEUS Collab., J. Breitweg et al., Eur. Phys. J. C1 (1998) 81.

[123] ZEUS Collab., M.Derrick et al., Z. Phys. C68 (1995) 569.

[124] H1 Collab., S. Aid et al., Phys. Lett. B358 (1995) 412.

[125] B.W. Rust and W.R. Burrus, 'Mathematical Programming and the Numerical Solutions of Linear Equations', Mod. Anal. and Comp. Meth. in Science and Math. 38, ed. R. Bellman.

[126] G. D'Agostini, DESY-94-099.

[127] A. Hocker and V. Kartvelishvili, hep-ph/9509307.

[128] Hannes Jung, Private communication.

[129] J. Bartels, J. Ellis, H. Kowalski and M. Wüsthoff, hep-ph/9803497.

[130] ZEUS Collab., M. Derrick et al., Phys. Lett. B356 (1995) 601.

[131] ZEUS Collab., M. Derrick et al., Phys. Lett. B380 (1996) 220.

[132] H1 Collab., S. Aid et al., Nucl. Phys. B468 (1996) 3.

[133] H1 Collab., C. Adloff et al., Z. Phys. C75 (1997) 607.

[134] R.D. Field and G. Fox, Nucl. Phys. B80 (1974) 367.

[135] J. Cudell, K. Kang and S.K. Kim, hep-ph/9701312.

[136] A. Donnachie and P.V. Landshoff, Nucl. Phys. B267 (1986) 690.

[137] ZEUS Collaboration; M.Derrick et al., Z. Phys. C72 (1996) 399.

[138] W. Buchmüller, Phys. Lett. B353 (1995) 335.

[139] G. Ingelman and K. Prytz, Z. Phys. C58 (1993) 285.

[140] K. Golec-Biernat and J. Kwiecinski, hep-ph/9607399.

[141] ZEUS Collab., *Measurement of the Diffractive Cross Section in Deep Inelastic Scattering using ZEUS 1994 Data.*, to be published.